



Pilkington Library

Author/Filing Title GYNZ - REKOWSKI

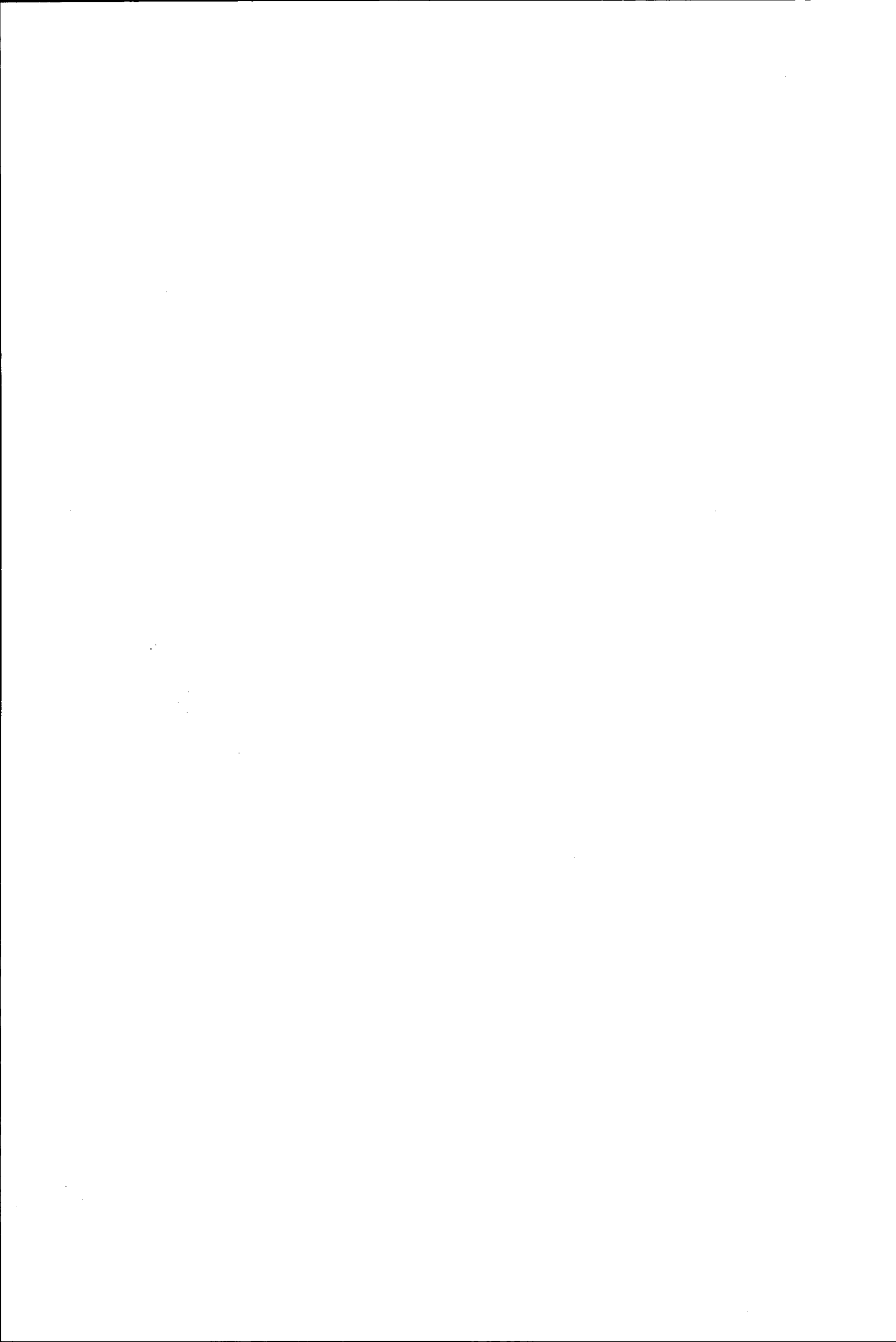
.....
Vol. No. Class Mark T

**Please note that fines are charged on ALL
overdue items.**

FOR REFERENCE ONLY

0402589653





Specific Heat Measurement
and its application to
 $\text{Pd}_2[\text{Rare Earth}]_{\text{In}}$ Alloys


by
Felix v.Gynz-Rekowski

A Master's Thesis
Submitted in partial fulfilment of the requirements
for the award of the degree

Master of Philosophy

of
Loughborough University
United Kingdom

© by Felix v.Gynz-Rekowski (2001)

 University of Toronto P. 101
Date <i>Aug 02</i>
Class
Acc. No. <i>040258965</i>

ABSTRACT

Some experimental details of the construction and programming of the equipment is presented and discussed. The calorimeter is used to determine the specific heat of solid, approximately 1 g samples within the temperature range 4 to 210 K. Initially, the performance of the calorimeter is demonstrated by measuring the specific heat of a spectroscopically pure copper sample. The working of the apparatus is demonstrated with the experimental investigation of the specific heat of some Pd₂[Rare Earth]In Alloys. The 4*f*-electron contribution to the specific heat of Pd₂YbIn and Pd₂HoIn is determined, by subtraction of isostructural Pd₂LuIn from the measured specific heat of Pd₂YbIn and Pd₂HoIn.

TABLE OF CONTENT

ABSTRACT	I
TABLE OF CONTENT	II
1 INTRODUCTION	1
2 ELEMENTARY PROPERTIES OF RARE EARTH METALS AND Pd₂[RE]In ALLOYS	3
2.1 Introduction.....	3
2.2 Structural Behaviour	3
2.3 Magnetic Properties	5
2.4 The RKKY Interaction	6
2.5 References	7
3 OUTLINE OF CRYSTAL FIELD THEORY	8
3.1 The Free Ion	8
3.1.1 The Ground State of the Free Ion	8
3.1.2 The Hamiltonian of the Free Ion	11
3.2 Interaction of the Ion with the Crystalline Environment	12
3.2.1 Classification of the Crystal Field	12
3.2.2 Crystal Field Potential	13
3.2.3 Stevens Operator Equivalent Method.....	14
3.2.4 The LLW Parameterisation Scheme	15
3.3 References	17
4 SPECIFIC HEAT	18
4.1 Heat Capacity	18
4.1.1 Heat Capacity of ideal Gases	18
4.1.2 Heat Capacity of Solids.....	19
4.2 Lattice Heat Capacity	21
4.2.1 Classical Interpretation.....	21
4.2.2 Quantum Mechanical Theories	22
4.3 Free Electron Heat Capacity	26
4.4 Magnetic Heat Capacity	28
4.5 Determination of the Thermal Properties of Crystal Field Splitting	29
4.6 Isolating Different Contributions	31
4.6.1 Non Magnetic Materials	31
4.6.2 Estimating the Conduction Electron and Phonon Contribution of Magnetic Materials	31
4.7 Summary	34
4.8 References	35

5	CALORIMETER DESIGN AND AUTOMATION	36
5.1	Introduction.....	36
5.2	Adiabatic Calorimetry.....	36
5.3	Design Overview	37
5.3.1	The Calorimeter.....	37
5.3.2	Temperature Measurement	39
5.3.3	Sensor Calibration	39
5.3.4	Interfacing.....	41
5.4	Shield Temperature Control	42
5.4.1	Feedback Control.....	43
5.4.1.1	Proportional (P).....	44
5.4.1.2	Integral (I)	45
5.4.1.3	Derivative (D)	46
5.4.2	Heater Power Range	47
5.4.3	Tuning PID Parameter	47
5.5	Software	53
5.5.1	System Set-up Phase	53
5.5.2	Preparation Phase.....	53
5.5.3	Measurement Phase.....	54
5.5.4	Analysis Phase	56
5.6	Heat Capacity of the Calorimeter	57
5.6.1	Addenda.....	57
5.6.2	Apiezon N High Vacuum Grease.....	59
5.7	Copper Standard	60
5.8	Summary	63
5.9	References	64
6	SAMPLE PREPARATION AND CHARACTERISATION.....	65
6.1	Sample Preparation	65
6.2	X-Ray Diffraction	66
6.2.1	Experimental Set-up for X-ray Diffraction	66
6.2.2	Structure of Pd ₂ [Heavy Rare Earth]In Alloys	68
6.2.3	Structure of Pd ₂ [Light Rare Earth]In Alloys	74
6.3	Conclusion.....	79
6.4	References	79
7	MEASUREMENT OF SPECIFIC HEATS OF SOME Pd₂[RE]In ALLOYS	80
7.1	Specific Heat of Pd ₂ LuIn	80
7.2	Crystal Field Excitations in Pd ₂ YbIn	82
7.2.1	CEF Level Scheme	83
7.2.2	C _{CEF} of Pd ₂ YbIn	84
7.3	Crystal Field Excitations in Pd ₂ HoIn.....	85
7.3.1	CEF Level Scheme	86
7.3.2	C _{CEF} of Pd ₂ HoIn.....	86
7.4	Discussion	87
7.5	References	89
8	SUMMARY AND OUTLOOK	90

1 INTRODUCTION

Specific Heat measurements constitute a very useful tool for investigating the magnetic properties of Rare Earth intermetallic compounds. In these systems with total angular momentum J , the $2J+1$ associated quantum levels are split by the surrounding crystalline electric field (CEF). That leads to a rapid change in the internal energy as the temperature increases from 0K and the excited CEF levels become populated. This provides a large contribution to the specific heat at temperatures around the Schottky peak. Furthermore, other contributions to the specific heat may arise from the magnetic excitations present in ordered materials, from critical phenomena in the vicinity of the ordering temperature, or from spin fluctuations above it [4.4]. At sufficiently low temperatures the specific heat of the investigated materials can be considered to have the form

$$C = \gamma T + \beta T^3 + C_m. \quad (1.1)$$

The linear term is due to conduction electrons and is related to the density of states at the Fermi level. The term that is cubic in temperature is the low-temperature approximation to the lattice heat capacity of a solid. The coefficient β is related to the Debye temperature. C_m stands for the contribution of the specific heat due to the magnetic degrees of freedom of the material.

The work presented in this thesis details the design and automation of a calorimeter for the measurement of specific heat of solid samples in the temperature range from 4.2 K to 210 K. The functioning of this instrument is then demonstrated by measuring and analysing the specific heat of members of the $\text{Pd}_2[\text{RE}]\text{In}$ alloys series (RE = Rare Earth metal).

Structure of this Thesis

Chapter two: Gives a short introduction to the properties of Rare Earth metals, such as electron configuration, crystal structure, the magnetic properties of pure Rare Earth metals and the mechanism of magnetic interaction of the Rare Earth 4f electrons in Pd₂[RE]In intermetallic alloys.

Chapter three: An outline of the crystal field theory is given which leads to the discussion of the effect of the crystal field on the degenerated Rare Earth 4f electron levels. In order to calculate the Hamiltonian of the 4f electrons the Stevens operator equivalent method is introduced as well as the crystal field parameterisation scheme by Lea, Leask and Wolf (LLW).

Chapter four: The theory of the specific heat of solids is presented. The different contributions due to conduction electrons, the lattice heat capacity and magnetic degrees of freedom as well as thermal properties of the crystal field splitting are discussed.

Chapter five: The Design and automation of the calorimeter is presented. The working procedure of the software is shown, as well as the tuning of the shield temperature control. The accuracy of this system is tested by measuring the specific heat of Copper.

Chapter six: Samples are prepared by melting of the appropriate quantities of starting elements in an argon arc furnace. A structure determination is performed using X-ray powder diffraction. The heavy Pd₂[RE]In alloys (RE = Ho, Er, Yb and Lu) are being examined as well as some light Pd₂[RE]In compounds (RE = La, Ce and Nd).

Chapter seven: The subject of this chapter is the specific heat of Pd₂[RE]In Heusler alloys (RE = Ho, Yb and Lu). The heat capacity of each compound is measured and an analysis is made. The CEF level scheme of the Rare Earth 4f electrons obtained by previous investigations are verified.

Chapter eight: Gives a general conclusion. Recommendations for further work and improvements on the instrument are discussed.

2 ELEMENTARY PROPERTIES OF RARE EARTH METALS AND Pd₂[RE]In ALLOYS

2.1 Introduction

Rare Earth metals, elements alternatively known as Lanthanide's, have an atomic number between Lanthanum (Z=57) and Lutetium (Z=71). Strictly speaking, Lanthanum is not a Rare Earth element and is often omitted in discussions of their properties [2.1]. Praseodymium (Pm) is a radioactive element with a half-life time of six hours (Pm¹⁴⁵) and therefore people refrained from investigating its properties.

Rare Earth elements form a subgroup in the periodic table and are usually arranged outside the periodic table, since they all exhibit similar chemical characteristics. This is due to the fact, that the electronic structure is given by $(4f)^n(5s)^2(5p)^6(5d)^1(6s)^2$, where n increases from 0 to 14 as the atomic number increases from 57 to 71 [2.2]. The 5p and 6s electrons form part of the conduction band in the metals, while the 4f -electrons are well embedded within the atom and shielded by the 5s and 5p states from surroundings [2.3].

2.2 Structural Behaviour

The structure of Rare Earth metals at room temperature was first investigated by Klemm and Bommer in 1937 [2.4]. Since then a complete classification of the room temperature crystal structures has been carried out and is given by Taylor and Darby [2.1] for example. The results for those Rare Earth elements under consideration in this work are given in Table 2.1. The structures are shown in Figure 2.1.

Table 2.1: The room temperature structural properties of the pure Rare Earth metals

	Atomic number		Molar mass	Metallic radius [Å]	Ionic radius [Å]	Structure	Space Group
Lanthanum	La	57	138.91	1.877	1.061	d-hex	P6 ₆ /mmc
Cerium	Ce	58	140.12	1.825	1.034	d-hex	P6 ₃ /mmc
Neodymium	Nd	60	144.24	1.821	0.995	d-hex	P6 ₃ /mmc
Holmium	Ho	67	164.93	1.766	0.894	hcp	P6 ₃ /mmc
Erbium	Er	68	167.26	1.757	0.881	hcp	P6 ₃ /mmc
Ytterbium	Yb	70	173.04	1.940	0.858	fcc	Fm3m
Lutetium	Lu	71	174.97	1.734	0.848	hcp	P6 ₃ /mmc

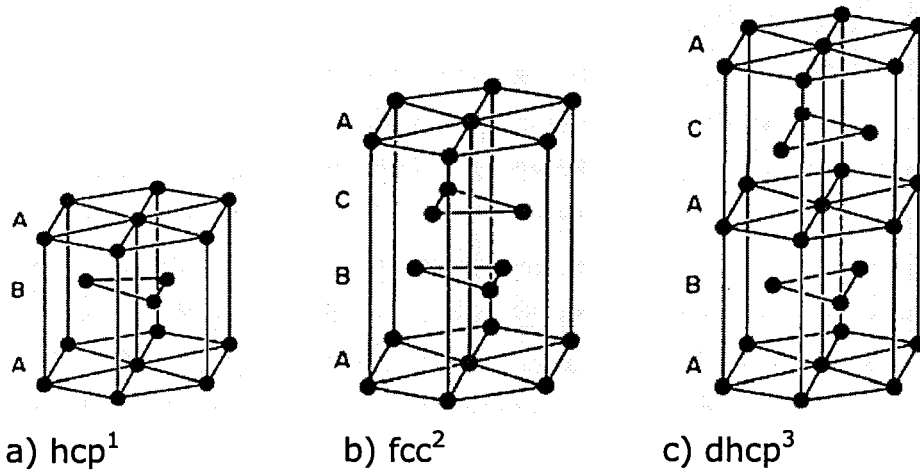


Figure 2.1: Closed-packed structures [2.1]

The atomic radius decreases from Lanthanum to Lutetium, while the atomic number increases (with two exceptions for Europium and Ytterbium). This effect is known as the Lanthanide Contraction and is shown in Figure 2.2.

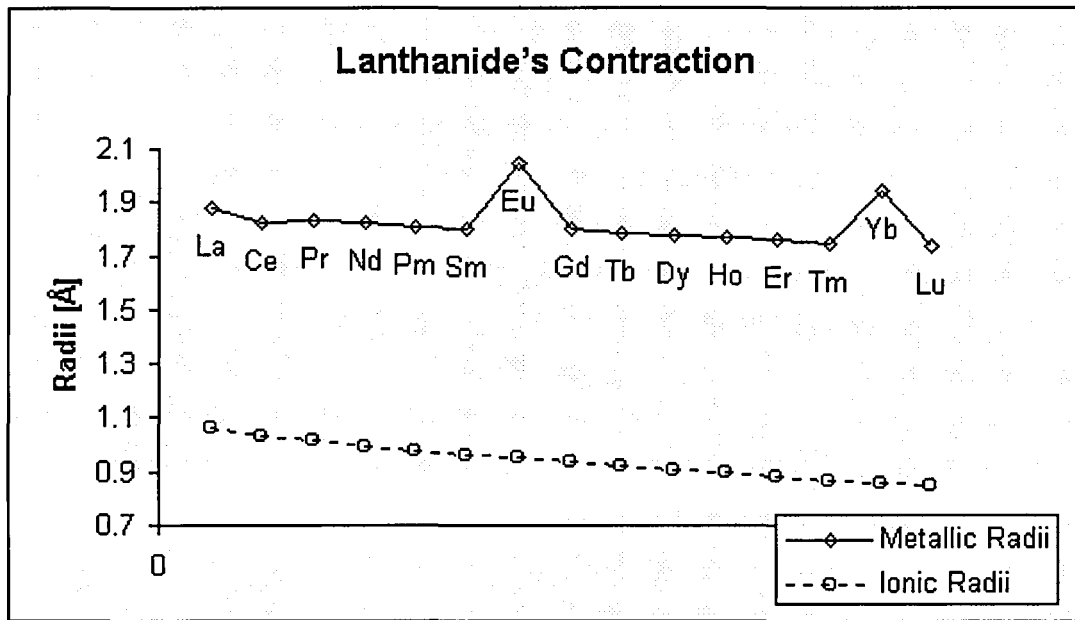


Figure 2.2: Lanthanide's Contraction, the variation of the metallic radius of the Rare Earth elements with atomic number

The great uniformity of the crystalline structure and of the atomic radius can be described in a first approximation as resulting from the $(5d)^1(6s)^2$ electron shells which are nearly the same for all Rare Earth metals, while the interaction between the nucleus and the electrons is increasing with atomic number.

¹ hexagonal closed packed

² face centred cubic

³ double hexagonal closed packed

2.3 Magnetic Properties

As already mentioned previously, the electron configuration of the Rare Earth elements is given by:

$$(4f)^n(5s)^2(5p)^6(5d)^1(6s)^2. \quad (2.1)$$

They all appear to be group IIIa elements of the periodic table. This arises from the fact, that the number of outer valence electrons remains unchanged, while the $(4f)^n$ shell is been filled with increasing atomic number. The $4f$ electrons are closely bound inside the outer shells and thus they play only a small role in chemical bounding. In metallic alloys, the $5d$ and $6s$ levels are partially filled and form part of the conduction electron band [2.5]. The intra-atomic electron-electron interactions among $4f$ electrons generate a localised magnetic moment. The overlap of $4f$ orbitals of different atoms is too small to create magnetic ordering. Therefore, the magnetism cannot be explained by a direct exchange mechanism. However, it can be described by an indirect exchange mechanism (see next page, RKKY interaction).

For systems with localised magnetic moments, the magnitude of the magnetic moment depends on the filling of the electron shells. For the Rare Earth metals, spin S and the orbital momentum L are coupled to give the total angular momentum J . The total magnetic moment μ is equal to

$$\mu = -g_L \mu_B \sqrt{J(J+1)} \quad (2.2)$$

where μ_B is Bohr magneton, g_L the Landé factor.

S , L and therefore J are given according to the Hund's rules [2.6]. In order to calculate the magnetic moment of atoms, the Landé factor has to be calculated using the Landé formula:

$$g_L = 1 + \frac{J(J+1) + S(S+1) + L(L+1)}{2J(J+1)} \quad (2.3)$$

With this, the atomic magnetic moment can be calculated, which is shown for Rare Earth metals in Figure 2.3. Pure Rare Earth metals are paramagnetic at sufficiently high temperature and present different magnetic orderings at low temperatures [2.7].

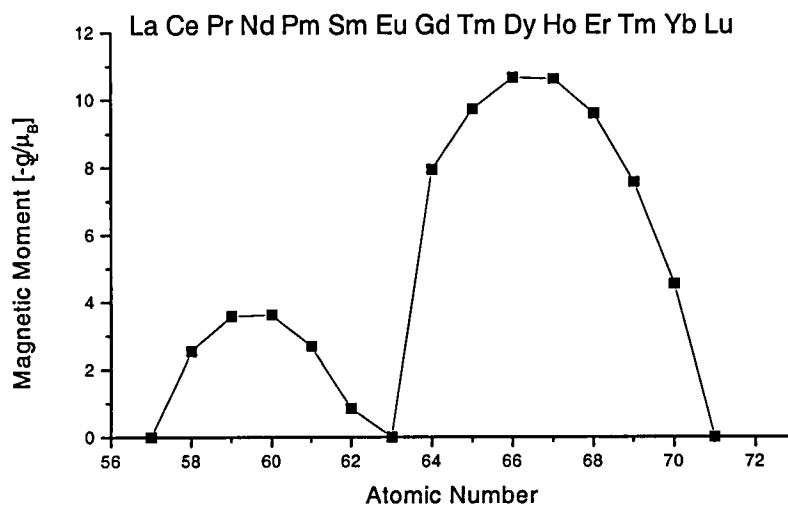


Figure 2.3: Calculated Magnetic Moment of Rare Earth metals

2.4 The RKKY Interaction

The RKKY (Ruderman, Kittel, Kasuya & Yosida) interaction describes magnetic ordering of localised magnetic moments in Rare Earth metals. In this theory, the magnetic ordering of the localised moments is caused by an indirect exchange interaction mediated by the conduction electrons. The conduction electrons move in the field of the localised moments on the atoms. Each localised moment interacts with the conduction electrons. As a result, a certain direction of the localised moment and the polarisation of the conduction electrons is favoured. Because of their itinerant character, the conduction electrons interact with many neighbouring localised moments. Therefore, it is favourable for the localised moments to align in a certain way to enable the most favourable interaction of each of the localised moments with the conduction electrons. Whether a ferro- or antiferromagnetic alignment of the localised moments is preferred, depends on the sign of the exchange interaction. This exchange interaction is oscillatory. Since the conduction electrons spin may interact with impurities and magnetic disorder, the interaction is damp. The RKKY has been applied to many different materials, such as for example Cu-Mn alloys (Yosida [2.8]), $\text{Pd}_2[\text{RE}]\text{Sn}$ (Babateen [2.9]). Furthermore, various extensions have been made to the theory. Reviews are given, for example, by Kittel [2.6], and Kasuya [2.10]. Calculations, especially for Heusler alloys, were done by Blandin & Campbell [2.11], Malmstroem, Geldart & Blomberg [2.12], Price [2.13] and Kuebler, Williams & Sommers [2.14].

2.5 References

- [2.1] Taylor K.N.R., Darby M.I., "Physics of Rare Earth Solids", Chapman and Hall Ltd, (1972)
- [2.2] Chikazumi S. and Charap S., "Physics of magnetism" Robert E. Krieger Publishing Company Huntington N.Y., (1978)
- [2.3] Jensen J., Macintosh A.R., "Rare Earth magnetism, structures and excitations", from "The International Series of Monographs on Physics", Clarendon Press, Oxford, (1991)
- [2.4] Klemm W. and Bommer H., Z. anorg. u. allgem. Chem., 231, 138 (1973)
- [2.5] Wohlfarth E.P., "Ferromagnetic Materials", North-Holland Publishing Company, (1980)
- [2.6] Kittel Ch., "Einführung in die Festkörperphysik", 12. Auflage, R.Oldenburg Verlag München Wien (1999)
- [2.7] Coqblin B., "The Electronic Structure of Rare-Earth Metals and Alloys: the magnetic heavy Rare-Earths", Academic Press Inc. (London) Ltd. (1977)
- [2.8] Yosida T., "Magnetic Properties of CU-Mn Alloys", Phys. Rev., 106 (5) 893, (1957)
- [2.9] Babateen M.O., "An Investigation of Magnetic Properties of some Rare Earth Heusler Alloys", PhD Thesis, Loughborough University, (1994)
- [2.10] Kasuya T., "Magnetism" ed. Rado and Suhl, Academic Press, London, 28 215 (1966)
- [2.11] Blandin A., Campbell I.A., " RKKY Spin Polarization in a Strongly Perturbed Medium and Applications to Hyperfine Fields", Phys. Rev. Lett. 31 51 (1973)
- [2.12] Malmstroem G., Geldart D.J.W., Blomberg C., "Interaction between local magnetic moments in metals :I", J. Phys. F, 6 233 (1976)
- [2.13] Price D.C., "Indirect magnetic coupling between local moments in metals", J. Phys. F, 8 933 (1978)
- [2.14] Kübler J., Williams A.R., Sommers C.B., "Formation and coupling of magnetic moments in Heusler alloys", Phys. Rev. B 28 1745 (1983)

3 OUTLINE OF CRYSTAL FIELD THEORY

3.1 The Free Ion

3.1.1 The Ground State of the Free Ion

The unpaired electrons in any particular ion exist in shells and have energies appropriate to it. The electron energy in each shell, when neglecting all interactions (besides the coulomb interaction between the nucleus and the electrons), is given by [3.1]

$$E_n = -\frac{e^2 Z}{2r} = -\frac{m_e e^4 Z}{2 \hbar^2 n^2} \quad (3.1)$$

where n is the principle quantum number of the electron shell, Z the atomic number, m_e and e the electron mass and electron charge, \hbar Planck's constant divided by 2π .

Within each shell n of an atom there are n sub-shells characterised by ℓ , the angular quantum number that ranges from 0, 1 to $n-1$. These sub-shells ℓ contain $2\ell + 1$ states labelled by m , the magnetic quantum number which can take values $-\ell, (1 - \ell), \dots, (\ell - 1)$ and ℓ . In addition, each state can be occupied by two electrons with opposite spin. s characterises the spin quantum number and is limited to the values $\pm 1/2$. For each n there are

$$\sum_{\ell=0}^{n-1} 2(2\ell + 1) = 2n^2 \quad (3.2)$$

possible combinations of quantum numbers ℓ , m and s . Such states are called degenerate. According to Pauli's exclusion principle, the maximal number of electrons in a sub-shell ℓ , is equal to the number of possible states. For the 4f-shell, which is of particular interest in the investigation of the magnetic behaviour of Rare Earth ions in a crystal lattice, ℓ is equal to three and thus the maximum number of electron states in this shell is 14.

For more complex atoms with more than one electron, the rather simple model of a central coulomb potential must be extended by the impact of the coulomb interaction between the electrons with each other, as well as spin-orbit interaction [3.1]. Pauli's exclusion principle prevents electrons with the same spin to be at the

same state. Moreover, because of the coulomb interaction the energy of electrons with the same spin is lower [3.2] than of those with opposite spin in the same shell. For Rare Earth metals, the coulomb repulsion between electrons is large compared to the spin-orbit interaction. Therefore, Russell-Saunders coupling scheme⁴ can be applied. The individual ℓ_i and s_i couple as

$$\sum_i \ell_i = L \quad \text{and} \quad \sum_i s_i = S \quad (3.3)$$

to give the total orbital angular momentum number L and the total spin number S . Due to the spin-orbit interaction, the total orbital angular momentum and the total spin then couple to give the total angular momentum. In order to appraise the groundstate electron configuration of the free ion, S and L have to be determined according to Hund's⁵ rules to yield the total angular momentum quantum number J . The value of J is given by

$$J = |L - S| \quad (3.4)$$

if less than half of all states in the shell are occupied by an electron and

$$J = L + S \quad (3.5)$$

if more than half of the states within the shell are occupied. If exact half of all states are occupied, then, according to the first Hund's rule, L is equal to zero and therefore

$$J = S \quad (3.6)$$

The degeneracy of an energy level E_n with respect to ℓ is reduced by the electron-electron interaction. The degeneracy with respect to m is not lifted as long as the spherical symmetry of the potential is unchanged. The spherical symmetry is broken, for example, by an external magnetic field [3.3].

To illustrate this by an example, S , L and J are given for Ytterbium-, Erbium- and Holmiumion [3.4]

⁴ known as LS-coupling, after Kubo & Nagamiya [3.5], it can be applied to Rare Earth metals
⁵ see for example Kittel [3.2]

1. Ytterbium (Yb^{3+}), 13 electron in the 4f-shell
 $\ell = 3$

$$|\vec{S}| = \sum_{i=1}^{13} s_i = \frac{1}{2}$$

$$|\vec{L}| = \sum_{i=1}^{13} l_i = 3 \quad (3.7)$$

$$|\vec{J}| = |L + S| = \frac{7}{2}$$

The groundstate degeneracy is $2J + 1 = 8$

The groundstate configuration of Yb^{3+} is $^2\mathbf{F}_{7/2}$

2. Erbium (Er^{3+}), 11 electron in the 4f-shell

$$|\vec{S}| = \sum_{i=1}^{11} s_i = \frac{3}{2}$$

$$|\vec{L}| = \sum_{i=1}^{11} l_i = 6 \quad (3.8)$$

$$|\vec{J}| = |L + S| = \frac{15}{2}$$

The groundstate degeneracy is $2J + 1 = 16$

The groundstate configuration of Er^{3+} is $^2\mathbf{I}_{15/2}$

3. Holmium (Ho^{3+}), 10 electron in the 4f-shell

$$|\vec{S}| = \sum_{i=1}^{10} s_i = 2$$

$$|\vec{L}| = \sum_{i=1}^{10} l_i = 6 \quad (3.9)$$

$$|\vec{J}| = |L + S| = 8$$

The groundstate degeneracy is $2J + 1 = 17$

The groundstate configuration of Ho^{3+} is $^5\mathbf{I}_8$

3.1.2 The Hamiltonian of the Free Ion

Considering a single particle with an electric charge e in a central Coulomb potential $V(r)$, in example the hydrogen atom, the Hamilton operator is given by [3.3]:

$$H = -\frac{\hbar^2}{2m_e} \Delta + V(r) \quad \text{with} \quad V(r) = -\frac{Z e^2}{4\pi \epsilon_0 r} \quad (3.10)$$

where r is the distance between the electron and the nucleus.

There are different interactions within the free ion, which contribute to form the Hamiltonian of a many electron atom. The most important of these are [3.1], [3.6]:

1. Nucleus Screening

For electrons in outer shells in atoms with more than one electron, the coulomb potential of the nucleus is screened by the inner shell electrons. This effect is recognised by introducing the effective nucleus number.

$$Z_{eff} = Z - s \quad (3.11)$$

s is correction term [3.1].

2. The Coulomb Repulsion

Since electrons are particles of the same charge, they are repelled by each other, this is known as Coulomb repulsion. The magnitude of this potential is inversely proportional to the distance between the electrons.

$$V_{ee} = \sum_{i=1}^N \sum_{j=1}^{i-1} \frac{e^2}{r_{ij}} \quad (3.12)$$

3. Spin-Orbit Coupling

A magnetic field is produced by the orbital motion of the electron around the nucleus. An interaction arises between the orbital momentum and the electron spin, which can be described by

$$V_{sl} = -\frac{1}{2m_e^2 c^2} \sum_{i=1}^N \frac{1}{r_i} \frac{dV(r)}{dr_i} (\vec{s}_i \cdot \vec{\ell}_i). \quad (3.13)$$

Considering these effects, the Hamiltonian of the free atom H_f is given by

$$H_f = -\sum_{i=1}^N \left[\frac{\hbar^2}{2m_e} \Delta_i + \frac{Z_{eff} e^2}{4\pi \epsilon_0 r_i} \right] + V_{ee} + V_{st} \quad (3.14)$$

3.2 Interaction of the Ion with the Crystalline Environment

If a magnetic ion is placed into a crystal lattice, a perturbation of the free ion electron states will occur because of the electrostatic field caused by the neighbouring atoms. This field is of certain symmetry. As a result, the degenerated electron levels will separate analogue to the Stark effect⁶. The number of components, into which a term of the free ion will separate, depends on the symmetry of the field, as determined then by the symmetry of the crystal. This interaction between the magnetic ion and its surroundings is often treated using Crystalline Electric Field (CEF) theory.

3.2.1 Classification of the Crystal Field

In order to determine the effect of the electric crystalline potential H_{cef} provided by the symmetrical distribution of the negative point charges about the central positive ion, one has to classify its magnitude relative to the Coulomb repulsion H_{ee} and the Spin-Orbit coupling H_{is} . Three different cases are distinguished [3.7]:

1. Strong Crystal Field: $H_{cef} \gg H_{ee} \gg H_{is}$

The energy of the field is stronger than the spin-orbit coupling and the Coulomb repulsion. The LS coupling is included using perturbation theory. The electrostatic interaction of the electrons can be included by using a self-consistent field, in example the Hartree-Fock approximation.

2. Intermediate Crystal Field: $H_{ee} \gg H_{cef} \gg H_{is}$

The crystal field is smaller than the electron-electron interaction but stronger than the spin-orbit coupling. The Hamiltonian of the free atom has to be considered with Coulomb repulsion and with the crystal field potential but without spin-orbit coupling.

⁶ Stark (1913) describes the splitting of energy levels of atoms in homogeneous electric field see for example [3.1].

3. Weak Crystal Field: $H_{ee} \gg H_{ls} \gg H_{cef}$

The crystal field is small. The "free ion", also considering electron repulsion and spin-orbit coupling, is influenced by the crystal field. The total angular momentum aligns relatively to the axes of the crystal field since the total orbital angular momentum and the total spin remain coupled.

This is the case for the Lanthanide.

3.2.2 Crystal Field Potential

Placed in the $\text{Pd}_2[\text{RE}]\text{In}$ crystal lattice, the Lanthanide ion is exposed to a cubic electrostatic field of the surrounding Palladium ions.

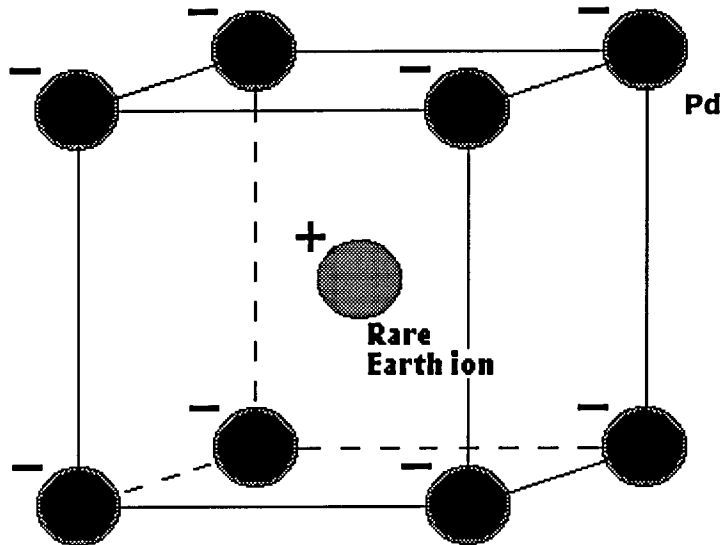


Figure 3.1: Rare Earth ion in the $\text{Pd}_2[\text{RE}]\text{In}$ crystal lattice, surrounded by Pd ions

In order to calculate the potential due to the ionic crystal, a simple point charge model can be used, although it is known to possess several weaknesses. It neglects the finite extent of charges on the ions, the overlap of the magnetic ion's wave functions with those of neighbouring ions, and the effects of "screening" of the magnetic electrons by the outer electron shells of the magnetic ion. However, it can be used to calculate ratios of terms of the same degree in the Hamiltonian of magnetic ions on lattice sites of high symmetry [3.8].

The electrostatic potential $V(r, \theta, \phi)$ due to the surrounding point charges, at a point (r, θ, ϕ) near the origin at the magnetic ion is given by [3.8]

$$V(r, \theta, \phi) = \sum_j \frac{q_j}{|R_j - r|} \quad (3.15)$$

where q_j is the charge of the j^{th} ion, a distance R_j from the origin.

If the magnetic ion is of the charge q_i at (r_i, θ_i, ϕ_i) , then the crystalline potential energy will be given by

$$H_{cef} = \sum_i q_i V_i = \sum_i \sum_j \frac{q_i q_j}{|R_j - r|}. \quad (3.16)$$

As the crystal field affects closed shells only in a higher order of the perturbation expansion, the summations in (3.16) will only concern electrons in the unfilled shell. The crystalline potential in (3.15) may be calculated in Cartesian coordinates, or directly in terms of spherical harmonics. Both methods are demonstrated for example Hutchings [3.8].

3.2.3 Stevens Operator Equivalent Method

As already revealed, the Rare Earth ions show Russell-Saunders coupling, so the single electron angular momentum and spins are first combined after (3.3) to yield J according to Hund's rules. For these states, the total angular momentum operator \hat{J} is a constant, according to Stevens [3.9].

Stevens Operator Equivalent Method depend largely on the result, that within a manifold of states for which \hat{J} is a constant there are simple relations between the matrix elements of potential operators and appropriate angular momentum operators [3.9]. In the following, this method is briefly discussed.

In [3.9] the crystal field potential considered is a sum of potential functions,

$$\sum_{n,m} V_n^m = V_2^0 + V_4^0 + V_6^0 + V_6^6 \quad (3.17)$$

where

$$\begin{aligned} V_2^0 &= \sum (3z^2 - r^2) \\ V_4^0 &= \sum (35z^4 - 30z^2 r^2 + 3r^4) \\ V_6^0 &= \sum (231z^6 - 315z^2 r^4 + 5r^6) \\ V_6^6 &= \sum (x^6 - 15x^4 y^2 + 15x^2 y^4 + y^6). \end{aligned} \quad (3.18)$$

The summations are taken over all coordinates of all electrons.

Each potential V can be written in the form $f(r)P_n^m(\theta, \phi)$ and thus transforms under rotation according to an irreducible representation of the rotation group. Therefore, the matrix elements of V_6^6 can be obtained from those of V_6^0 by pure symmetry arguments [3.9]. In order to determine the potential functions in (3.17) respectively (3.18), using Stevens operator equivalent method x , y and z have to be

replaced by J_x , J_y , and J_z . Since each potential transforms under rotation according to an irreducible presentation of the rotation group, for an operator equivalent to hold, the equivalent must transform in exactly the same way. There is no difficulty in doing this provided allowance is made for the non-commutation of J_x , J_y , and J_z . For example the product of xy is given by $1/2 (J_x J_y + J_y J_x)$.

For a manifold of angular momentum J composed of f -electron wave functions the most general operator equivalent potential with cubic point symmetry may be written, according to Baker et al. [3.10], as

$$H_{cef} = B_4(O_4^0 + 5O_4^4) + B_6(O_6^0 - 21O_6^4) \quad (3.19)$$

Where the potential functions are given by the Stevens operator equivalents

$$\begin{aligned} O_4^0 &= 35J_z^4 - [30J(J+1) - 25]J_z^2 - 6J(J+1) + 3J^2(J+1)^2 \\ O_4^4 &= \frac{1}{2}(J_+^4 + J_-^4) \\ O_6^0 &= 231J_z^6 - 105[3J(J+1) - 7]J_z^4 \\ &\quad + [105J^2(J+1)^2 - 525J(J+1) + 294]J_z^2 \\ &\quad - 5J^3(J+1)^3 + 40J^2(J+1)^2 - 60J(J+1) \\ O_6^4 &= \frac{1}{4}[11J_z^2 - J(J+1) - 38](J_+^4 + J_-^4) \\ &\quad + \frac{1}{4}(J_+^4 + J_-^4)[11J_z^2 - J(J+1) - 38]. \end{aligned} \quad (3.20)$$

The coefficients B_4 and B_6 are factors which determine the scale of the crystal field splitting's. They are linear functions of $\langle r^4 \rangle$ and $\langle r^6 \rangle$, the mean fourth and sixth power of the radii of the magnetic electrons (and thus depend on the detailed value of the magnetic ion wave function).

3.2.4 The LLW Parameterisation Scheme

Lea, Leask and Wolf (LLW) [3.11] have investigated the effect of a cubic crystal field Hamiltonian, as given in (3.19), as a function of the ratios of the fourth and the sixth degree terms. LLW rewrote (3.19) in the form

$$H_{cef} = W \left[\frac{x}{F(4)} (O_4^0 + 5O_4^4) + \frac{1-x}{F(6)} (O_6^0 - 21O_6^4) \right] \quad (3.21)$$

where W is the overall energy scale of the crystal field splitting and x determines the ration between the fourth and the sixth order contribution.

$$\frac{B_4}{B_6} = \frac{x}{1-|x|} \cdot \frac{F(6)}{F(4)} \quad (3.22)$$

$|x| < 1$ so that

$$\frac{B_4}{B_6} = 0 \quad \text{for } x = 0 \quad \text{while} \quad \frac{B_4}{B_6} = \pm \infty \quad \text{for } |x|=1 \quad (3.23)$$

$F(4)$ and $F(6)$ are numerical constants, their values are tabulated in [3.11]. These calculations have been done for all J manifolds between 2 and 8 in half-integral steps. Table 3.1 shows the LLW crystal field parameters for the alloys considered in this work. The values are taken from [3.11] and [3.12]

Table 3.1: LLW parameters for members of the alloys series Pd2[RE]In, vales taken from [3.11] and [3.12]

	$F(4)$	$F(6)$	W (meV)	x	OES ⁷ (meV)
Holmium	60	16860	0.0267	0.3543	19.9
Erbium	60	13860	-0.0462	0.3644	19.9
Ytterbium	60	1260	-0.7058	0.7758	18.8

It is this information which is been used to calculated the expected thermal response of the CEF in form of the specific heat (see also section 4.5 Determination of the Thermal Properties of Crystal Field Splitting).

⁷ OES – Overall Energy Splitting

3.3 References

- [3.1] Mayer-Kuckuk, Theo "Atomphysik" Teubner Studienbücher: Physik, Teubner, Stuttgart, (1977)
- [3.2] Kittel Charles, "Introduction to Solid State Physics" 7th Edition, John Wiley & Sons, Inc., New York, Chichester, Brisbane, Toronto, Singapore, (1996)
- [3.3] Nolting Wolfgang, "Grundkurs Theoretische Physik 5 Quantenmechanik, Teil 2: Methoden und Anwendungen", Friedr. Vieweg & Sohn Verlagsgesellschaft mbH, Braunschweig / Wiesbaden, (1997)
- [3.4] Taylor K.N.R., Darby M.I., "Physics of Rare Earth Solids", Capman and Hall Ltd, London (1972)
- [3.5] Kubo R, Nagamiya N., "Solid State Physics", McGraw-Hill Book Co. Inc., (1968)
- [3.6] Dieke G.H., "Spectra and energy levels of Rare Earth ions in solid state physics", Interscience Publishers, 1968
- [3.7] Behte H., "Termaufspaltung in Kristallen", Annalen der Physik, **3**, 133, (1929)
- [3.8] Hutchings M.T., "Point-Charge Calculations of Energy Levels of Magnetic Ions in Crystalline Electric Fields", Solid State Physics, V16, Academic Press, New York, (1964)
- [3.9] Stevens K.W.H., "Matrix Elements and Operator Equivalents Connected with the Magnetic Properties of Rare Earth Ions", Proc. Phys. Soc., 1952, A65, p.209
- [3.10] Baker J.M., Leaney B., Hayes W., Proc. Roy. Soc., A247, p141, (1958)
- [3.11] Lea K.R., Leask M.J.M. Wolf W.P., " The Raising of angular momentum degeneracy of f-electron terms by cubic crystal fields", J. Phys. Chem. Solids, Pergamon Press, V23, pp1381-1405, (1962)
- [3.12] Babateen M.O., "An Investigation of Magnetic Properties of Some Rare Earth Heusler Alloys", PhD Thesis, Loughborough University, (1994)

4 SPECIFIC HEAT

4.1 Heat Capacity

The heat capacity of a system is defined as the ratio of energy input to the system by heating dQ and the resulting temperature rise dT .

$$C = \frac{dQ}{dT} \quad (4.1)$$

From the first law of thermodynamics, which gives a relationship between dQ , the change in the internal energy dU and the work dA done by the system due to a change in volume dV at a given pressure p and the second law of thermodynamics, from which it can be obtained that for reversible isothermal processes dQ can be written as temperature times change in entropy, it follows

$$dQ = TdS = dU - dA. \quad (4.2)$$

Differentiating (4.2) with respect to T at constant volume V or, experimentally more relevant, at constant pressure p , the heat capacity can be written as a function of the internal energy U .

$$C_V = \left(\frac{\partial U}{\partial T} \right)_V \quad (4.3)$$

$$C_P = \left(\frac{\partial U}{\partial T} \right)_P + p \left(\frac{\partial V}{\partial T} \right)_P \quad (4.4)$$

4.1.1 Heat Capacity of ideal Gases

For an ideal gas, the internal energy can be written as a function of temperature and the number of atoms/molecules (with k_B being the Boltzmann constant).

$$U = U(T, N) = \frac{3}{2} k_B TN \quad (4.5)$$

Each degree of freedom has an average energy of $\frac{1}{2} k_B TN$. Using (4.3) it follows that

$$C_V^{Gas} = \frac{3}{2} k_B N. \quad (4.6)$$

By deriving the ideal gas law for classic, ideal gases

$$p \cdot V = N \cdot k_B \cdot T \quad (4.7)$$

with respect to temperature and under constant pressure

$$p \left(\frac{\partial V}{\partial T} \right)_p = N k_B \quad (4.8)$$

and substitute (4.8) in (4.4), one obtains C_p for an ideal gas

$$C_p = \frac{3}{2} k_B N + N k_B = C_v + N k_B \quad (4.9)$$

The heat capacity at constant pressure C_p is larger than C_v because some energy is required for the work as the gas expands.

4.1.2 Heat Capacity of Solids

To maintain the heat capacity for solids equations (4.3) and (4.4) have to be rewritten as functions of entropy (cp. (4.2)).

$$C_v = T \left(\frac{\partial S}{\partial T} \right)_v \quad (4.10)$$

$$C_p = T \left(\frac{\partial S}{\partial T} \right)_p \quad (4.11)$$

Considering entropy as a function of T and V and taking the number of atoms N to be constant, the total differential of S is given as

$$S = S(T, V) \rightarrow dS = \left(\frac{\partial S}{\partial T} \right)_v dT + \left(\frac{\partial S}{\partial V} \right)_T dV \quad (4.12)$$

Differentiating (4.12) with respect to T under constant pressure p gives

$$\left(\frac{\partial S}{\partial T} \right)_p = \left(\frac{\partial S}{\partial T} \right)_v + \left(\frac{\partial S}{\partial V} \right)_T \left(\frac{\partial V}{\partial T} \right)_p \quad (4.13)$$

Multiplying (4.13) by T reveals

$$C_p = C_v + T \left(\frac{\partial S}{\partial V} \right)_T \left(\frac{\partial V}{\partial T} \right)_p \quad (4.14)$$

By using the following Maxwell relations and the reciprocal relation for p , V and T , S can be eliminated

$$\left(\frac{\partial S}{\partial V}\right)_T = \left(\frac{\partial p}{\partial T}\right)_V \quad (4.15)$$

$$\left(\frac{\partial p}{\partial T}\right)_V \left(\frac{\partial T}{\partial V}\right)_P \left(\frac{\partial V}{\partial p}\right)_T = -1 \quad (4.16)$$

and (4.14) can be modify to

$$C_P = C_V - T \left(\frac{\partial V}{\partial T}\right)_P^2 \left(\frac{\partial p}{\partial V}\right)_T \quad (4.17)$$

Introducing the volume expansion coefficient α

$$\alpha = \frac{1}{V} \left(\frac{\partial V}{\partial T}\right)_P \quad (4.18)$$

and the isothermal compressibility

$$\kappa_T = -\frac{1}{V} \left(\frac{\partial V}{\partial p}\right)_T \quad (4.19)$$

equation (4.17) can finally be expressed as

$$C_P = C_V + \frac{\alpha^2}{\kappa_T} VT \quad (4.20)$$

$C_{p/V}$ gives the heat capacity of the entire system. $C_{p/V}$ divided by the system's mass or number of particles N provides the heat capacity per mass unit or particle. This is called *Specific Heat*. It is a function of T and the material.

Similar to the results for an ideal gas, C_p is larger than C_v . The difference between C_p and C_v decreases linear with decreasing T and $C_p \rightarrow C_v$ if T tends towards $0K$. At room temperature and for the most metallic alloys C_p is 3-5% larger than C_v . This is shown for Copper in Figure 4.1.

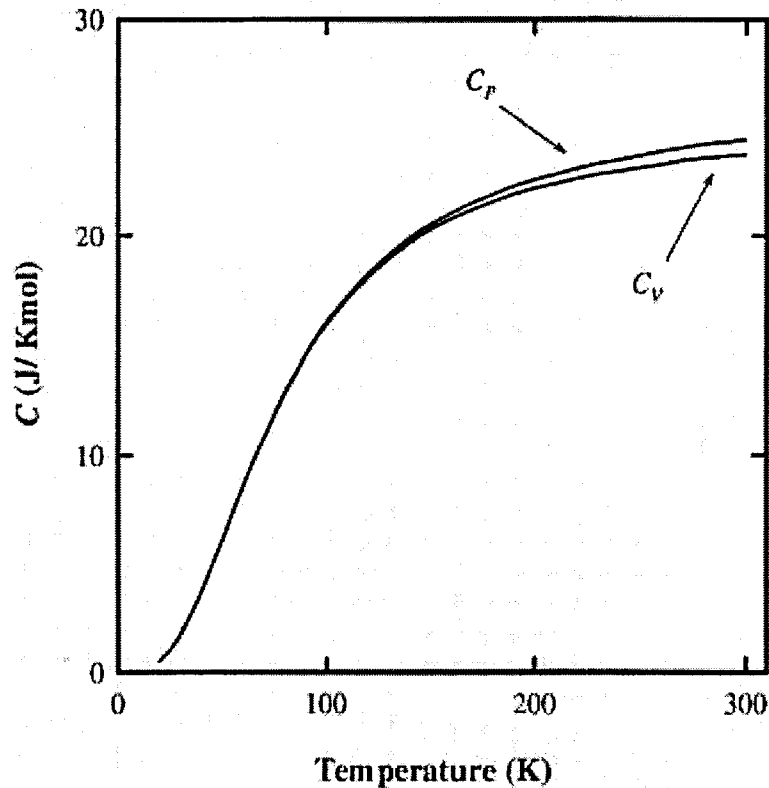


Figure 4.1: The specific heat of Copper at constant volume and pressure [4.1]

4.2 Lattice Heat Capacity

For most solids, the energy of the lattice vibrations provides the dominant specific heat contribution. For non-magnetic insulators it is the only contribution. At lower temperatures, the importance of the lattice heat capacity decreases and contributions from magnetic ordering or conduction electrons may dominate. At temperature below 1 K, and in particular for magnetically ordered samples, the heat capacity due to the orientation of nuclear spins may become important.

4.2.1 Classical Interpretation

There is more than one model to describe the motion of atoms in a crystal. From the classical statistics point of view and with the application of the theorem of equipartition of energy it follows that in a system of classical particles the average energy per degree of freedom in thermal equilibrium is $\varepsilon = \frac{1}{2}k_B T$. Thus for a crystal lattice, each atom has 6 degrees of freedom and therefore the energy is given as

$$U = \sum_i \varepsilon_i = 3k_B TN. \quad (4.21)$$

Hence the heat capacity C_V is obtained by calculating the derivative of U with respect to T , the phonon heat capacity C_V^{lat} becomes

$$C_V^{lat} = \left(\frac{\partial U}{\partial T} \right)_V^{lat} = 3Nk_B \quad \text{and} \quad C_V^{lat} (\text{per mol}) = 3R \quad (4.22)$$

with the molar gas constant $R = N_A k_B$, the Avogadro constant N_A and the Boltzmann constant k_B . This was discovered in 1819 by Dulong and Petit. In this model C_V is a constant. At low temperatures, this is not in agreement with observations. It is found, that as the temperature of a system decreases, the heat capacity is reduced well below the Dulong-Petit value, tending towards zero at zero temperature.

4.2.2 Quantum Mechanical Theories

At lower temperature, the energy of the harmonic oscillator decreases sufficiently so that the discrete nature of particles becomes important and quantum mechanics has to be used to explain the behaviour of the heat capacity. A lattice vibration mode n of frequency ω is restricted to the energy levels given by

$$\varepsilon_n = \hbar\omega(n+1/2). \quad (4.23)$$

Einstein developed a model considering the vibrating atoms in a solid as independent oscillators, i.e. non-coupled, all vibrating at the same frequency ω . So the average energy of a vibration mode is $\bar{\varepsilon}$ with p_n being the probability of finding the oscillator in the n^{th} energy state ε_n .

$$\bar{\varepsilon} = \sum_n p_n \varepsilon_n. \quad (4.24)$$

The probability of occupation of an energy level is given by the Boltzmann factor

$$\exp\left\{ \frac{-\varepsilon_n}{k_B T} \right\} \quad (4.25)$$

thus (4.24) becomes

$$\bar{\varepsilon} = \frac{\sum_{n=0}^{\infty} \hbar\omega(n+1/2) \exp\left\{ \frac{-\hbar\omega(n+1/2)}{k_B T} \right\}}{\sum_{n=0}^{\infty} \exp\left\{ \frac{-\hbar\omega(n+1/2)}{k_B T} \right\}}. \quad (4.26)$$

To evaluate the average energy of a vibration mode (4.26) has to be rewritten to

$$\bar{\varepsilon} = k_B T^2 \frac{1}{Z} \frac{\partial Z}{\partial T} = k_B T^2 \frac{\partial \ln(Z)}{\partial T}. \quad (4.27)$$

where the partition function Z is given by

$$\begin{aligned} Z &= \sum_{n=0}^{\infty} \exp\left\{-\frac{\hbar\omega(n+1/2)}{k_B T}\right\} \\ &= \exp\left\{\frac{-\hbar\omega}{2k_B T}\right\} \cdot \left(1 + \exp\left\{\frac{-\hbar\omega}{k_B T}\right\} + \exp\left\{\frac{-2\hbar\omega}{k_B T}\right\} + \dots\right) \\ &= \exp\left\{\frac{-\hbar\omega}{2k_B T}\right\} \cdot \left(1 - \exp\left\{\frac{-\hbar\omega}{k_B T}\right\}\right)^{-1}. \end{aligned} \quad (4.28)$$

By substituting (4.28) in (4.27) the average energy of a harmonic oscillator can be obtained as

$$\bar{\varepsilon} = 1/2 \hbar\omega + \frac{\hbar\omega}{e^{\hbar\omega/k_B T} - 1} \quad (4.29)$$

For very low temperatures $\bar{\varepsilon}$ tends towards the zero point energy

$$k_B T \ll \hbar\omega \quad \rightarrow \quad \bar{\varepsilon} \approx 1/2 \hbar\omega \quad (4.30)$$

and for high temperatures the exponential term in (4.29) can be expanded to

$$\begin{aligned} \bar{\varepsilon} &= 1/2 \hbar\omega + \hbar\omega \left(\frac{\hbar\omega}{k_B T} + \frac{1}{2} \left(\frac{\hbar\omega}{k_B T} \right)^2 + \dots \right)^{-1} \\ &= 1/2 \hbar\omega + k_B T \left(1 - \frac{1}{2} \frac{\hbar\omega}{k_B T} + \dots \right)^{-1} \end{aligned} \quad (4.31)$$

and thus yields the Dulong/Petit law for the heat capacity.

$$\begin{aligned} k_B T \gg \hbar\omega \quad \rightarrow \quad \bar{\varepsilon} &= 1/2 \hbar\omega + \hbar\omega \left(\frac{\hbar\omega}{k_B T} + \frac{1}{2} \left(\frac{\hbar\omega}{k_B T} \right)^2 + \dots \right)^{-1} \\ &= k_B T \left(1 + \mathcal{O} \left(\frac{k_B T}{\hbar\omega} \right)^2 \right) \cong k_B T \end{aligned} \quad (4.32)$$

At any arbitrary temperature, the molar specific heat of the lattice is obtained by taking the derivative of the internal energy $U = 3N\bar{\epsilon}$ with respect to temperature. It can be expressed by using the Einstein temperature $\Theta_E = \hbar\omega/k_B$ as

$$C_V^{lat} = \left(\frac{\partial U}{\partial T} \right)_V^{lat} = 3Nk_B \left(\frac{\Theta_E}{T} \right)^2 \frac{e^{\Theta_E/T}}{(e^{\Theta_E/T} - 1)^2}. \quad (4.33)$$

The Einstein model was found to describe the experiment reasonably well. However, at low temperatures $C_{V(Einstein)}$ decreases faster than observed experimentally.

A more advanced model which takes into account that the harmonic oscillator do not vibrate independently was introduced by Debye who considered the system as a continuous elastic body. Based on the phenomenological theory of elasticity a continuum model is employed for all possible vibrational modes of a crystal in which the phonon frequency is not restricted to one value but ranges from $\omega = 0$ to some maximum value ω_D .

It is an assumption of the Debye model, that the distribution of the modes is spherically symmetric, i.e. the frequency of a mode only depends on the magnitude of the wave vector. This approximation is found to work reasonably well for crystals with high symmetry (for example Heusler alloys with a cubic structure). In the Debye approximation, the dispersion of acoustic waves is neglected.

ω_D , the cut-off frequency, is taken to be the frequency which yields the correct total number of lattice modes. For a crystal of volume V and containing N atoms there are $3N$ lattice vibration modes.

$$\int_0^{\omega_D} g(\omega) d\omega = 3N \quad (4.34)$$

with the density of states per unit frequency range $g(\omega)$ being chosen as

$$g(\omega) = \frac{V\omega^2}{2\pi^2} \left(\frac{1}{v_L^3} + \frac{2}{v_T^3} \right). \quad (4.35)$$

v_L and v_T represent the velocity of sound for longitudinal and transversal modes. Substituting (4.35) into (4.34) and integrating over all the distributions of vibration frequencies, the energy of the lattice vibrations is obtained as

$$U = \frac{9}{8} N \hbar \omega_D + \frac{9N}{\omega_D^3} \int_0^{\omega_D} \frac{\hbar \omega^3}{e^{\hbar \omega / k_B T} - 1} d\omega. \quad (4.36)$$

The derivative of U (4.36) with respect to temperature provides the heat capacity

$$C_V^{lat} = \left(\frac{\partial U}{\partial T} \right)_V^{lat} = 9Nk_B \left(\frac{T}{\Theta_D} \right)^3 \int_0^{\Theta_D/T} \frac{x^4 e^x}{(e^x - 1)^2} dx \quad (4.37)$$

with the variable $x = \hbar \omega / k_B T$ and the Debye temperature $\Theta_D = \hbar \omega_D / k_B$.

For high temperatures the integrand reduce to x^2 and thus the heat capacity yields the Dulong/Petit value.

$$T \gg \Theta_D \quad \rightarrow \quad C_V^{lat} = 3Nk_B \quad (4.38)$$

At low temperatures solving the integral results in $4\pi^4/15$ and from this the specific heat at low temperatures is given by the Debye T^3 law.

$$T < \Theta_D/10 \quad \rightarrow \quad C_V^{lat} = \frac{12}{5} Nk_B \pi^4 \left(\frac{T}{\Theta_D} \right)^3 = \beta T^3 \quad (4.39)$$

The Debye model describes the heat capacity of most solids with some success, even though the actual phonon density of states can be different to that assumed in the model.

The applicability of the Debye model to fit the specific heat of a system can be readily investigated by plotting Θ_D versus T . If the Debye model fits perfectly this would give a constant value for Θ_D , however the Debye temperature does vary with temperature and the degree of variability depends on the system under consideration. A particular variation in $\Theta_D(T)$ is often found where at low temperatures a minimum is found indicating that the specific heat rises more rapidly with temperature than would be expected from the Debye model. Despite having some weaknesses, the Debye model represents the specific heat of most solids well and it has been widely used to interpret experimental data [4.2].

4.3 Free Electron Heat Capacity

The contribution to the specific heat due to the free electrons applies only for metals and is given by

$$C_V^{el} = \left(\frac{\partial U}{\partial T} \right)_V^{el} \quad (4.40)$$

The theory, which describes the heat capacity of free electrons, was initiated with the discovery of the Pauli principle and the subsequent development of the Fermi-Dirac distribution function. When a system is heated from absolute zero, not all the free electrons gain an energy proportional to $k_B T$ as expected classically, but only those electrons within a range of $k_B T$ around the Fermi level are thermally excited (Figure 4.2).

The probability of occupation of an electron energy state ε is given by the Fermi distribution function

$$f(\varepsilon, T) = \frac{1}{e^{(\varepsilon - \mu)/k_B T} + 1} \quad (4.41)$$

where μ is the chemical potential, equal to the Fermi energy ε_F at $T = 0K$.

In the independent electron approximation the internal energy is given by the sum over all energy levels multiplied by the probability of occupation. The change in the internal energy by heating

$$\Delta U \equiv U(T) - U(0) \quad (4.42)$$

is therefore given as

$$\Delta U = \int_0^\infty d\varepsilon \varepsilon D(\varepsilon) f(\varepsilon, T) - \int_0^{\varepsilon_F} d\varepsilon \varepsilon D(\varepsilon) \quad (4.43)$$

with $D(\varepsilon)$ the density of states.

Multiplying the identity

$$N = \int_0^\infty d\varepsilon D(\varepsilon) f(\varepsilon, T) = \int_0^{\varepsilon_F} d\varepsilon D(\varepsilon) \quad (4.44)$$

by ε_F to obtain

$$\left(\int_0^{\varepsilon_F} + \int_{\varepsilon_F}^\infty \right) d\varepsilon \varepsilon_F D(\varepsilon) f(\varepsilon, T) = \int_0^{\varepsilon_F} d\varepsilon \varepsilon_F D(\varepsilon). \quad (4.45)$$

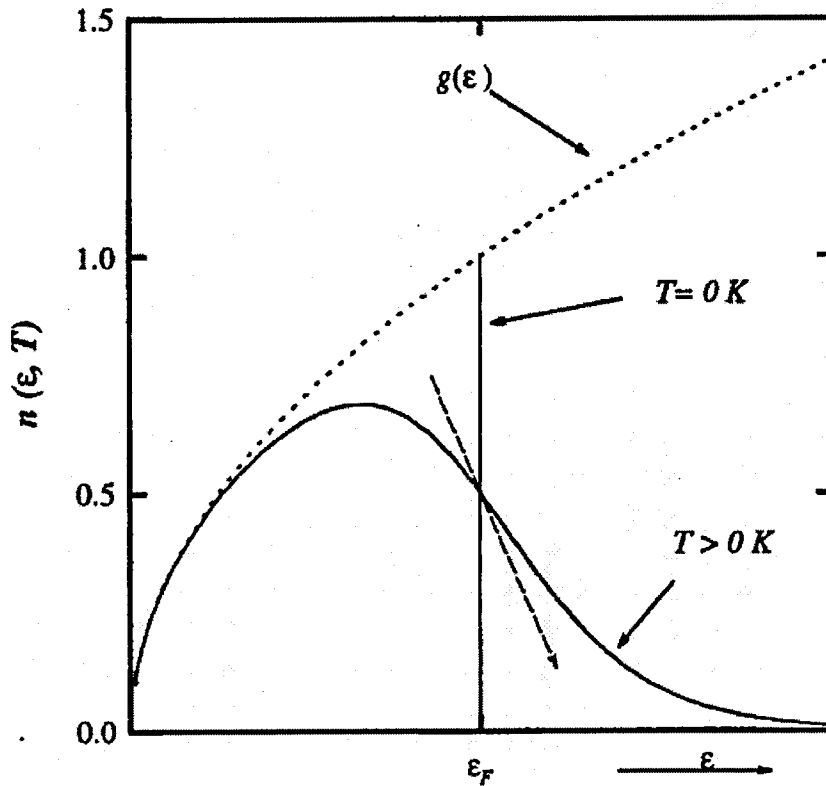


Figure 4.2: The Number of electrons per unit energy range according to the free electron model. The arrow shows the migration of electrons for $T > 0$ K. For clarity the situation is shown for which $k_B T$ is a significant proportion of ϵ_F , in general however, for all temperatures considered in this thesis $k_B T \ll \epsilon_F$, [4.2]

With (4.45), (4.43) can be rewritten as

$$\Delta U = \int_{\epsilon_F}^{\infty} d\epsilon (\epsilon - \epsilon_F) D(\epsilon) f(\epsilon, T) - \int_0^{\epsilon_F} d\epsilon (\epsilon_F - \epsilon) [1 - f(\epsilon, T)] D(\epsilon) \quad (4.46)$$

The heat capacity of the free electrons can be found by differentiating (4.46) with respect to temperature. Since $f(\epsilon, T)$ is the only temperature dependent term in (4.46), hence the terms can be grouped to obtain

$$C_V^{el} = \left(\frac{\partial U}{\partial T} \right)_V^{el} = \int_0^{\epsilon_F} d\epsilon (\epsilon - \epsilon_F) \frac{df}{dT} D(\epsilon). \quad (4.47)$$

At the temperatures of interest in metals, $(\epsilon - \epsilon_F) df/dT$ has a large positive peak at energies near ϵ_F , see for example Ashcroft [4.1]. According to Ashcroft, it is a good approximation to evaluate the density of states $D(\epsilon)$ at the Fermi level and taking it outside the integral.

$$D(\varepsilon_F) = \frac{3N}{2\varepsilon_F} = \frac{3N}{2k_B T_F} \quad (4.48)$$

Solving the integral for $k_B T \ll \varepsilon_F$, and with $D(\varepsilon)$, the heat capacity of free electrons becomes

$$C_{el} = \frac{1}{3} \pi^2 D(\varepsilon_F) k_B^2 T = \frac{1}{2} \pi^2 N k_B \frac{T}{T_F} = \gamma T. \quad (4.49)$$

Although T_F is called the Fermi temperature, it is not an actual temperature but a convenient reference notation.

4.4 Magnetic Heat Capacity

The energy required to align magnetic moments to form an ordered magnetic state, such as a ferromagnet, provides a contribution to the specific heat. The magnetic specific heat is associated with the magnetic entropy of a system

$$C_{mag} = T \left(\frac{dS_{mag}}{dT} \right)_B \quad (4.50)$$

A change in entropy of the magnetic state is given by

$$\Delta S_{mag}(T) = \int_0^T \frac{C_{mag}(\tilde{T})}{\tilde{T}} d\tilde{T} \quad (4.51)$$

and can be obtained from experimental measurements. Furthermore, this entropy is directly related to the quantum number of the magnetic atom J

$$\Delta S^S = ck_B N \ln[2J + 1] \quad (4.52)$$

where c is the number of atoms per unit cell present carrying the magnetic moment.

The total integral of the magnetic contribution to the specific heat is proportional to $\ln[2J+1]$. This assumes that the entropy of the ground state is equal to zero and that the temperature integration is carried out such that all CEF contributions are incorporated.

4.5 Determination of the Thermal Properties of Crystal Field Splitting

The free energy is a thermodynamic potential and thus it describes the thermodynamics of the system. F can be calculated as followed

$$F = U - TS. \quad (4.53)$$

Deriving (4.53) with respect to temperature yields, that the entropy S of a system is proportional to the derivative with respect to temperature of the Helmholtz free energy F ,

$$S = -\frac{\partial F}{\partial T} \quad (4.54)$$

while the partition function Z , of a system of N particles, is related to the Helmholtz free energy F via

$$F = -Nk_B T \ln\{Z\}. \quad (4.55)$$

In order to obtain the partition function it is necessary to sum over all energy levels

$$Z = \sum_i d_i \exp\left\{\frac{-e_i}{k_B T}\right\} \quad (4.56)$$

where e_i is the energy of the i^{th} level and d_i is its degeneracy.

Thus, by substituting the partition function Z of a system (4.56) in (4.55) and taking from that result the derivative with respect to temperature, the entropy (4.54) of a system can be obtained. Multiplying T to derivative of the entropy of the system with respect to temperature (4.50) yields the specific heat contribution due to the population of the excited electrons levels.

Therefore, by evaluating the partition function of a system, the thermodynamic properties with respect to the magnetic properties of that system are readily obtained and it follows that

$$C_{CEF} = T \left(\frac{dS}{dT} \right)_B = Nk_B T \frac{d^2}{dT^2} \left[T \text{Log} \left(\sum_i d_i \exp\left\{\frac{-e_i}{k_B T}\right\} \right) \right]_B. \quad (4.57)$$

At absolute zero, only the ground state electron levels are populated and as T is increased, energy must be provided to raise electrons to higher energy levels. There is only a limited range of magnetic energy levels. At very high temperatures, all levels are nearly equally populated so any increase in temperature will not lead to a significant gain in entropy of the system. Hence, the magnetic heat capacity at high temperatures is small. C_m is therefore expected to show a maximum at a temperature such that the thermal energy is of the order of the separation of the levels. This phenomenon is known as the *Schottky anomaly* [4.3].

As illustrated in Table 3.1, the overall CEF splitting energy (OES) of the investigated $\text{Pd}_2[\text{RE}]\text{In}$ alloys is approximately 20 meV, which is equal to a temperature of 230 K. However, the magnetic heat capacities of those systems under considerations is being calculated using the CEF level schemes⁸ obtained from neutron scattering experiments by Babateen [4.5].

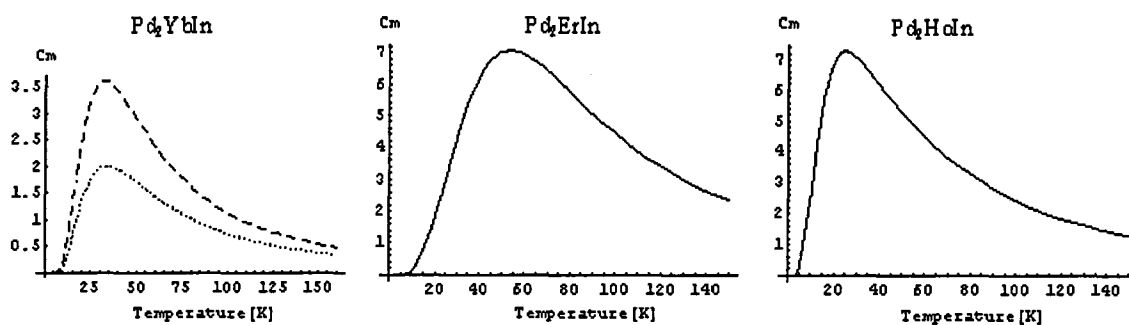


Figure 4.3: Calculated Magnetic Specific Heat ($[\text{J}/(\text{mol}\cdot\text{K})]$) of Pd_2YbIn , Pd_2ErIn & Pd_2HoIn

As shown in Figure 4.3, the Schottky peaks occurs for all alloys at temperatures $T < 70\text{K}$. Furthermore, for temperatures above $\sim 70\text{K}$ the magnetic heat capacity will be less than 1% of the measured heat capacity and thus the experimental uncertainty makes 70 K a suitable upper limit for the investigation.

⁸ For further details see to paragraphs 7.2.2 and 7.3.2.

4.6 Isolating Different Contributions

At low temperatures, where $C_p \approx C_v$ the heat capacity of a system is given by

$$C_p = C_{el} + C_{lat} + C_m \quad \text{for small } T \quad (4.58)$$

As already shown, the electronic and phonon heat capacities are given by

$$C_{el} = \gamma T \quad (4.59)$$

and

$$C_{lat} = \beta T^3. \quad (4.60)$$

In order to analyse the measured specific heat of a material and to obtain the magnetic contribution to the specific heat, electronic and phonon specific heats have to be isolated.

4.6.1 Non Magnetic Materials

For systems, for which the electronic and phonon heat capacities are the only contributions to the specific heat, the two contributions can be separated by plotting the experimental data in the form of C_p / T versus T^2 as

$$\frac{C_p}{T} = \gamma + \beta T^2 \quad (4.61)$$

This yields a straight line with intercept γ and with a slope of β

From this plot, the heat capacities due to the conduction electrons and the crystal lattice vibration can be obtained according to (4.59) and (4.60) respectively.

The analysis of the specific heat measurement of a system becomes more difficult if an additional contribution exists, such as that from magnetic moments.

4.6.2 Estimating the Conduction Electron and Phonon Contribution of Magnetic Materials

As before, the heat capacities due to the conduction electrons can often be obtained by plotting the low temperature data (where no magnetic contribution exists) in the form C_p / T versus T^2 [4.2]. Varying the Rare Earth atoms in the series $\text{Pd}_2[\text{RE}]$ is not expected to give rise to a significant change in the conduction electron density of states as a result of the localised nature of the $4f$ -electrons.

The main difficulty is to evaluate the lattice contribution of magnetic compounds, since it cannot be obtained directly. One way is to measure the specific heat at

temperature much higher than the magnetic ordering temperature, where the magnetic contribution vanishes, then to extrapolate the values to low temperatures according to the Debye model [4.4]. Since the accuracy of the considered instrument decreases with higher temperatures, another method is used to estimate the phonon contributions.

The lattice contribution is obtained by the measurement of the specific heat of an isomorphous non-magnetic compound. Here Pd₂LuIn is used. The results are renormalised by taking the different molar masses into account. For that purpose, Bouvier, Lethuillier and Schmit [4.4] have developed a many Debye function model of which a short outline is presented below.

The phonon part of the heat capacity may be written (cp. (4.37)) as

$$C_{lat} = 9Nk_B \left(\frac{T}{\Theta_D} \right)^3 \int_0^{\Theta_D/T} \frac{x^4 e^x}{(e^x - 1)^2} dx \quad (4.62)$$

with the variable $x = \hbar\omega/k_B T$ and the Debye temperature $\Theta_D = \hbar\omega/k_B$. For convenience, (4.62) may be written as

$$C_{lat} = N f_D(\Theta_D/T) \quad (4.63)$$

where $f_D(\Theta_D/T)$ is the single Debye function.

Applying the model to ternary compounds $X_m RE_n Z_p$, the lattice heat capacity can be expressed by the relationship

$$C_{lat}(X_m RE_n Z_p) = m f_D(\Theta_X/T) + n f_D(\Theta_{RE}/T) + p f_D(\Theta_Z/T) \quad (4.64)$$

This can be rewritten by considering low temperatures and using a single effective Debye temperature $\Theta_D(X_m RE_n Z_p)$ according to

$$C_{LowT}(X_m RE_n Z_p) = (m+n+p) f_D\left(\frac{\Theta_D(X_m RE_n Z_p)}{T}\right) \quad (4.65)$$

where $\Theta_D(X_m RE_n Z_p)$ is an effective Debye temperature which refers to the partial Debye temperatures Θ_X , Θ_{RE} and Θ_Z associated with X, RE and Z atoms in a given compound. m , n and p are the number of atoms per mole.

For further simplifications it is assumed, that all atoms in the crystal have the same mean-square displacement. It follows that

$$M_X(\Theta_X)^2 = M_Y(\Theta_Y)^2 = M_Z(\Theta_Z)^2 \quad (4.66)$$

where M_X , M_{RE} and M_Z are the molar masses of X, RE and Z atoms. Identifying the coefficients of the T^3 terms in equation (4.64) and (4.65) leads to the following relationship between all Debye temperatures

$$\frac{m+n+p}{[\Theta_D(X_m RE_n Z_p)]^3} = \frac{m}{[\Theta_X]^3} + \frac{n}{[\Theta_{RE}]^3} + \frac{p}{[\Theta_Z]^3} \quad (4.67)$$

It is assumed, that by replacing RE with another RE' element the partial Debye temperatures of the X and Z atoms are not modified. The corresponding effective Debye temperatures of both compounds are related by

$$\rho_{scale} = \frac{\Theta_D(X_m RE_n Z_p)}{\Theta_D(X_m RE'_n Z_p)} = \left[\frac{m(M_X)^{2/3} + n(M'_{RE})^{2/3} + m(M_Z)^{2/3}}{m(M_X)^{2/3} + n(M_{RE})^{2/3} + m(M_Z)^{2/3}} \right]^{1/3} \quad (4.68)$$

This renormalisation ratio ρ_{scale} provides the correction factor for the C_p versus T curve by which the nonmagnetic compound must be multiplied in order to obtain the lattice contribution of the magnetic compound under investigation. This factor has been calculated for the magnetic compounds considered here in [4.2] and is tabulated in Table 4.1

Table 4.1: Renormalisation parameters of the lattice specific heat of Pd₂LuIn to obtain the phonon blank for some of magnetic Rare Earth compounds [4.2]

	Holmium	Erbium	Ytterbium
ρ_{scale}	1.012	1.009	1.002

4.7 Summary

The heat capacity C of a system can be written as

$$C_p = C_v + \frac{\alpha^2}{\kappa_T} VT = \frac{\alpha^2}{\kappa_T} VT + C_{el} + C_{lat} + C_m \quad (4.69)$$

$$C_p = \gamma T + \beta T^3 + C_m \quad \text{for small } T$$

considering contributions due to the free electrons, the crystal lattice, magnetic momentum and the crystal field.

Except for low temperatures where $T \ll \Theta_D$, the phonon contribution to the specific heat dominates that of the electron gas. For non-magnetic compounds and temperatures less than approximately $\Theta_D/10$, the phonon contribution falls off rapidly as T^3 and the electronic contribution becomes a significant contribution to the measured specific heat. By plotting experimental data in the form C_p/T versus T^2 the two contributions can be isolated. Considering a model of free conducting electrons, the values of γ (the extrapolated intercept of the graph at $T=0$) and β (the slope) can be obtained from which the Fermi and Debye temperatures can be calculated. Substituting T_F into equations (4.48) and (4.49) the density of states at the Fermi level can be derived.

For magnetic materials, the electronic contribution can be obtained like for non-magnetic materials. However, the phonon blank can be estimated by the measurement of specific heat of an isomorphous nonmagnetic compound and by normalising the data using the ratio of the effective Debye temperatures of the compounds considered.

Knowing the heat capacity of the material obtained by measuring and deriving the electronic and phonon heat capacities as described above, the magnetic contribution to the specific heat can be calculated using equation (4.69).

The change in the internal order of a magnetic material as it passes through the transition temperature may be clearly displayed by plotting experimental data in the form C_p versus T . A sharp peak at the transition temperature is typical of a second order phase transition and is associated with the disappearance of long-range magnetic order. The small contribution of the magnetic specific heat just above the transition temperature arises from the presence of residual short-range magnetic order [4.6].

4.8 References

- [4.1] Ashcroft N.W., Mermin N.D., "Solid State Physics", Saunders College Publishing, (1976)
- [4.2] Parsons M.J., "An Investigation of the thermal properties of some Strongly Correlated Electron Systems", PhD Theses, Loughborough University, (1998)
- [4.3] Taylor K.N.R., Darby M.I., "Physics of Rare Earth Solids", Capman and Hall Ltd, (1972)
- [4.4] Bouvier M., Lethuillier P., Schmitt D., "Specific heat in some gadolinium compounds", Phys. Rev. B 43, 13137-13144 (1991)
- [4.5] Babateen M.O., "An Investigation of Magnetic Properties of Some Rare Earth Heusler Alloys", PhD Thesis, Loughborough University, (1994)
- [4.6] Dressler S., "Experimental Characterisation of the Low temperature Properties of $RE_{14}Ag_{51}$ Compounds", MPhil. Thesis, Loughborough University, (1999)

In preparation of this chapter on the theory of specific heat, among others the following textbooks have been consulted.

Baierlein R., "Thermal Physics", Cambridge University Press, (1999)

Black W.Z., Hartly J.G., "Thermodynamics, SI Version", 2nd ed., HarperCollinsPublishers, (1991)

Kittel Charles, "Introduction to Solid State Physics" 7th Edition, John Wiley & Sons, Inc., New York, Chichester, Brisbane, Toronto, Singapore, (1996)

Nolting Wolfgang, "Grundkurs Theoretische Physik 4 Spezielle Relativitaetstheorie / Thermodynamik", Friedr. Vieweg & Sohn Verlagsgesellschaft mbH, Braunschweig / Wiesbaden, 1997

Nolting Wolfgang, "Grundkurs Theoretische Physik 6 Statistische Physik", Friedr. Vieweg & Sohn Verlagsgesellschaft mbH, Braunschweig / Wiesbaden, 1997

5 CALORIMETER DESIGN AND AUTOMATION

5.1 Introduction

Heat capacities have been measured using a variety of experimental methods. In this work the "heat pulse method" is being used since bigger samples ($\cong 1\text{g}$) can be investigated. In this work a calorimeter based on the Nernst heat pulse method is used.

The specific heat measurement apparatus was originally designed by W. A. Hussen [5.1] within the scope of his PhD thesis and further improvements are implemented by M. J. Parsons within his PhD thesis with the help of J. W. Taylor and B. Dennis [5.2]. In order to increase the system's accuracy and temperature stability the sample temperature sensor was recalibrated and a new heater was added. This change in the calorimeter set-up is accompanied by a rewriting of the control software, using new temperature control parameters as well as new calibration data for the temperature sensors and the heat capacity of the empty calorimeter.

5.2 Adiabatic Calorimetry

For the determination of the specific heat the method of adiabatic calorimetry was used. Adiabatic calorimetry involves injecting a known quantity of energy into the sample and measuring its response in terms of a temperature variation. In the heat pulse method, the heat energy is supplied with constant power for the heat pulse time. The sample temperature is measured before and after the heat pulse is applied. The heat capacity is derived from the ratio of the heat input to the temperature rise.

$$C = \frac{\Delta Q}{\Delta T} \quad (5.1)$$

From observing the sample temperature before and after the heating period, respectively pre-drift and post-drift (Figure 5.1), the rate of heat flow from the sample to the surrounding system can be estimated and incorporated into the calculation of ΔT . Due to the design of the calorimeter⁹, the temperature measured during the heat pulse is slightly different from the actual temperature across the sample.

⁹ The sample temperature sensor is placed close to the edge of the sapphire plate, so while heating, the temperature at the heater is higher than at the sensor position. After the heat pulse is applied, the remaining energy dissipates towards the temperature sensor. This results in the overshoot observed. See also section 5.3.1 The Calorimeter.

To equalise this temperature gradient the system is given a short delay time before the post-drift measurement starts.

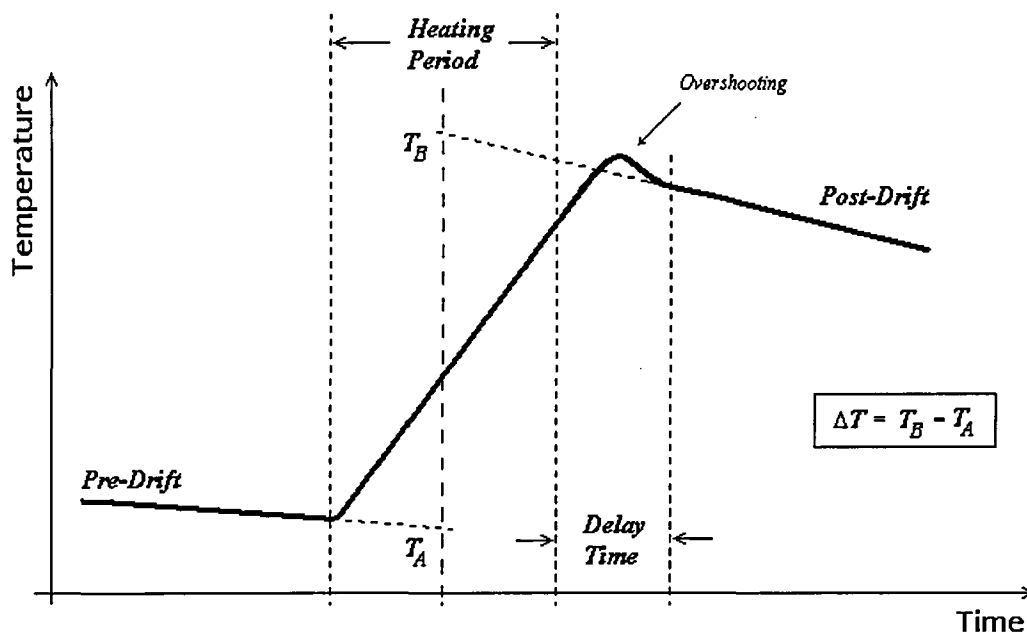


Figure 5.1: Variation of sample temperature during one measuring cycle, schematic

5.3 Design Overview

The cryogenic environment is provided by means of a ^4He storage Dewar (Oxford Instruments Ltd.). This Dewar consists of an outer liquid N_2 jacket acting as an intermediate cooling stage to the ^4He reservoir which provides a sample environment down to 4.2 K. A vacuum jacket separates the N_2 from the outer Dewar wall and from the ^4He .

5.3.1 The Calorimeter

The calorimeter consists of a sapphire disc of 25.4 mm in diameter and with a thickness of 0.5 mm, with a thin chromium heater on the side below. The sample is positioned on the disc above the heater by using a small amount (approximately 6 to 10 mg) of Apiezon N grease. The electrical connection to the sample heater is provided by 10 μm Gold wire (Goodfellows) and electrical conductive paint (RS Products Ltd.). The temperature of the sapphire plate and the sample is measured by a CERNOXTM temperature sensor (LakeshoreTM; model: CX-1050-SD; serial number: SN X05304). The sensor is attached at the bottom of the plate using GE 7031 low temperature varnish. The set-up is shown schematically in Figure 5.2.

The ensemble is situated within two copper radiation shields aimed at minimising thermal response time. The outer shield is a copper can, on which copper wire has been wound. The wire acts as a shield heater. A second heater placed on top of the

copper can. Temperature control of the outer shield is provided by means of another CERNOX™ sensor (Lakeshore™; CX-1050-SD; SN X06942) situated on the upper flange. The calorimeter is suspended from the outer ^4He bath by a stainless steel can which can be evacuated down to pressures of approximately 10^{-6} mbar, to minimise the heat transport by convection.

A cross-section of the calorimeter is shown in Figure 5.3.

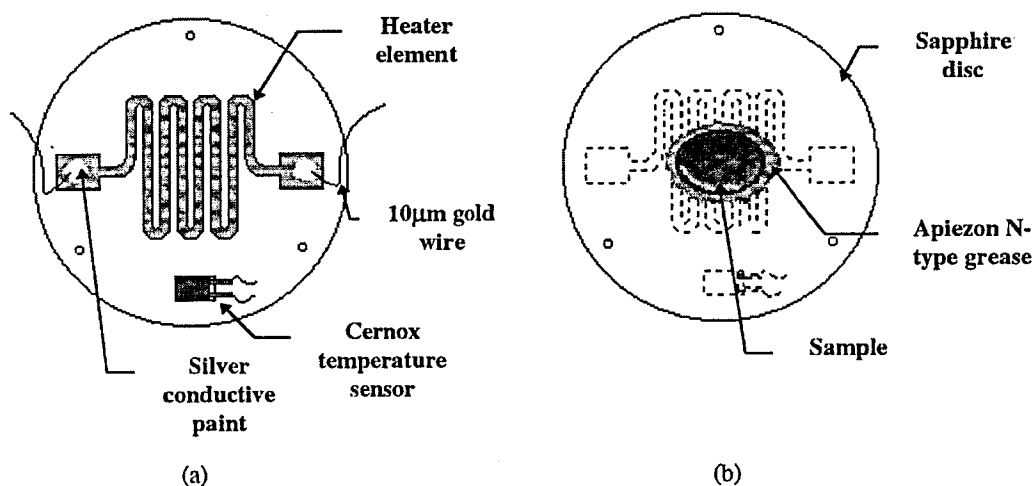


Figure 5.2: Schematic of the sample system, a) underside view, b) top view [5.2]

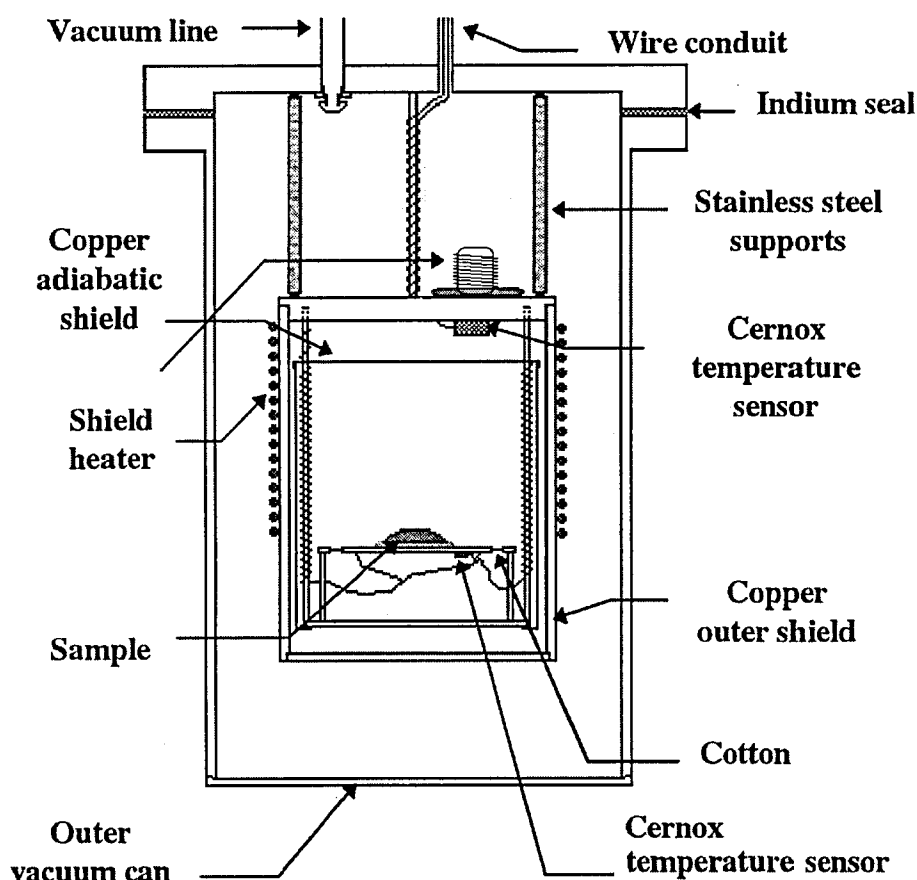


Figure 5.3: Cross-section of the calorimeter

5.3.2 Temperature Measurement

The temperature is determined by measuring the resistance of the CERNOX™ temperature sensors and calculating the temperature using calibration data. Setting, measurement and control of the temperature of the shield inside the calorimeter and measuring of the temperature of the sample is carried out by using a LakeShore Cryotronics, Inc. TEMPERATURE CONTROLLER MODEL DRC-93C. The temperature controller also contains a 9318C RESISTANCE INPUT CARD and an additional 8229 SCANNER CONVERSION OPTION. The DRC-93C is connected to a PC via a MODEL 8223 RS-232C INTERFACE.

The TEMPERATURE CONTROLLER MODEL DRC-93C is operated in RESISTANCE MODE, the 9318C RESISTANCE INPUT CARD in the CONTROL INPUT mode. The shield sensor X06942 is connected to channel A while the sample sensor X05304 is connected to channel B. A schematic picture of the data flow is shown in Figure 5.8.

The DRC-93C is an analogue controller. Its current variability has four ranges. Within each range there are 54 independent values. The supply voltage across the sensors is maintained at 10.5 millivolts. To do so, the 9318C RESISTANCE INPUT CARD has to alter the supply current.

To eliminate the resistance of the wiring of the sensor connection cable, the resistance is obtained in a four-lead measurement scheme.

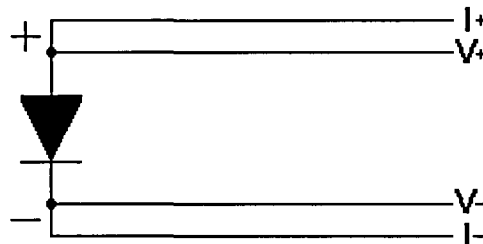


Figure 5.4: Four-Lead Sensor Connection

5.3.3 Sensor Calibration

CERNOX™ temperature sensor model CX-1050-SD have a negative temperature coefficient over a wide temperature range. These thin film sensors offer a small package size and low weight, which leads to a small sensor heat capacity to minimise addenda heat capacity. Furthermore, these sensors are easy to mount in packages designed for excellent heat transfer [5.3]. LakeShore™ offers a series of CERNOX™ temperature sensors with different characteristics. The sensor model CX-1050-SD was found to have the highest sensitivity over the whole temperature range covered by the calorimeter.

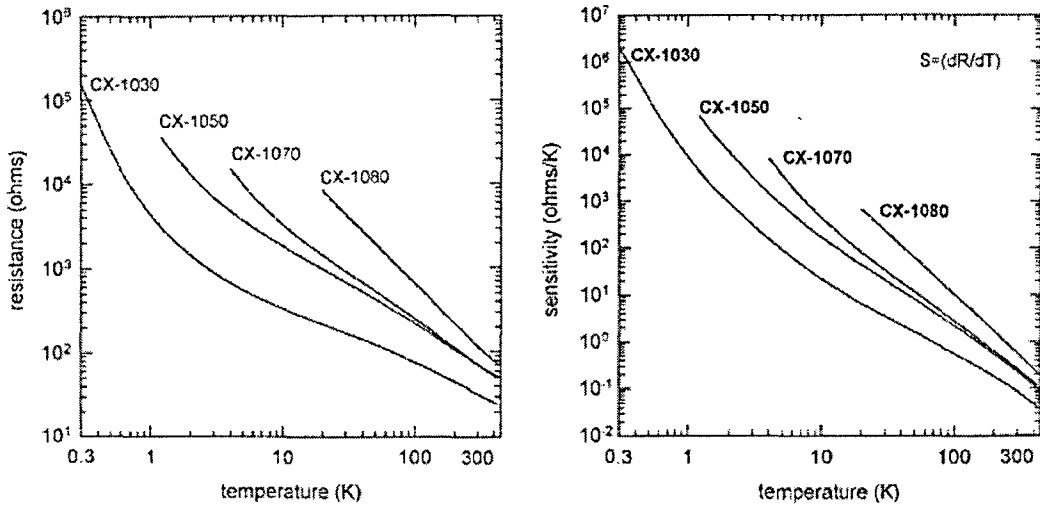


Figure 5.5: Typical Resistance and Sensitivity values for CERNOX™ Sensors [5.3]

The sensor X06942 has a known temperature response. To calibrate the sensor X05304 both sensors are placed next to each other (near the heater on the shield). A set temperature (\cong set resistance) as well as the temperature control settings (PID¹⁰ and heater current setting) is sent to the controller. When the system is stable, the values for the resistance of both sensors are obtained.

The system is considered stable, if the temperature drift is smaller than 25mK/min for at least 100 seconds for temperatures below 80K and temperature drift smaller than 50mK/min for at least 200 seconds for temperatures above 80K.

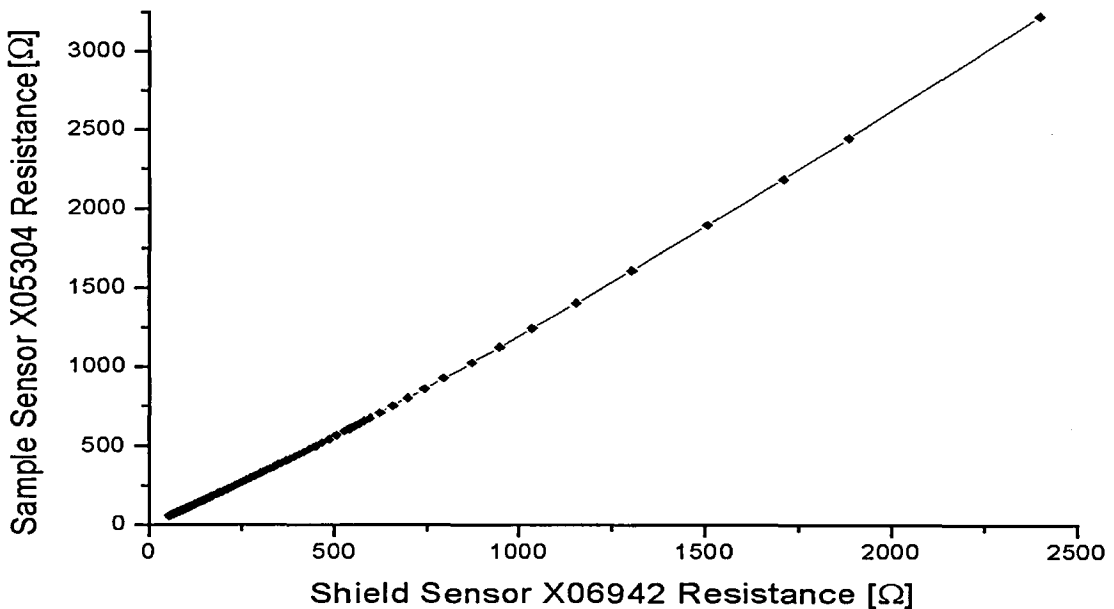


Figure 5.6: Sensor Resistance Calibration

¹⁰ See section 5.4 Shield Temperature Control

The data of the shield sensor temperature response is interpolated using a cubic spline interpolation method [5.4]. Using the shield - sample sensor resistance calibration in addition to the known temperature response of the shield sensor, the resistance versus temperature curve of both sensors can be obtained.

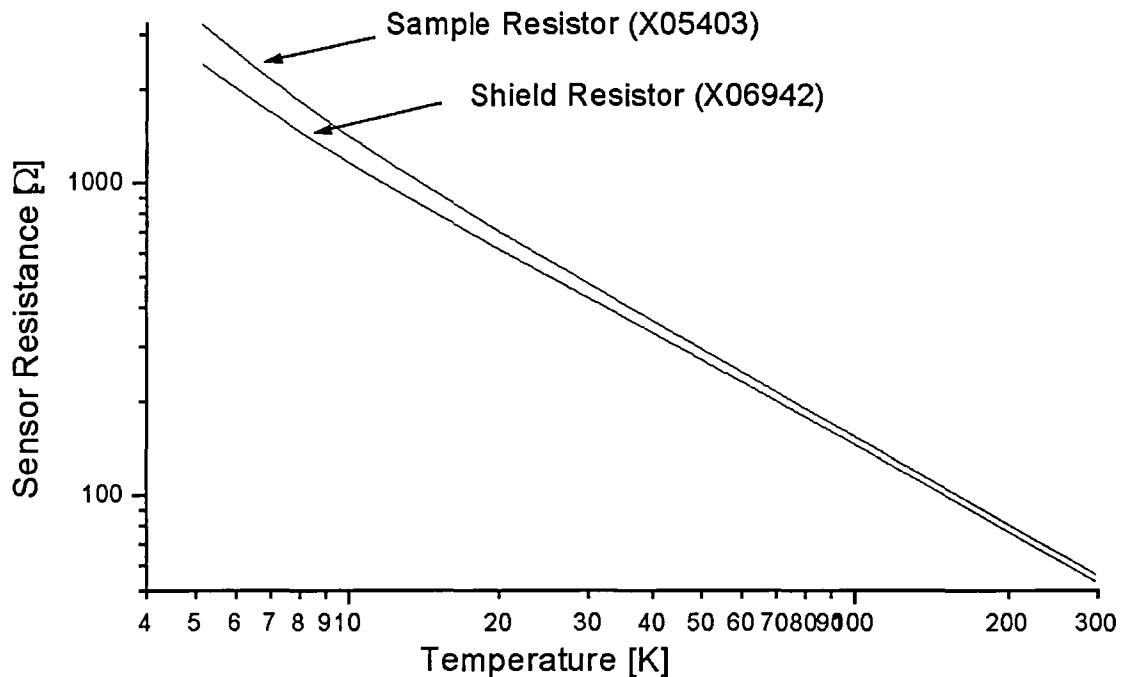


Figure 5.7: Resistance response with respect to temperature of shield and sample sensor

5.3.4 Interfacing

The automation is based around a PC with a Pentium processor running at 90 MHz. Communication with the temperature controller (Lakeshore MODEL DRC-93C) and digital voltmeter (DVM, Selfcal Digital Volt Meter 1271, Datron Wavetek) is made using an IEEE-488 interface. The IEEE-488 is an instrument bus with hardware and programming standards designed to simplify instrument interfacing [5.5]. The current source is built in-house. Any instrument on the interface bus has at least one of the three operating states: talker, listener or controller. Both, the temperature controller and the DVM can operate in either a talker or a listener mode, as data are being sent to or being read from these devices. The PC acts as a controller in that it designates to the devices on the bus, which function are to be performed. All instruments are connected in parallel to allow transfer of data between all the devices on the bus. Further details are given by Parsons [5.2]

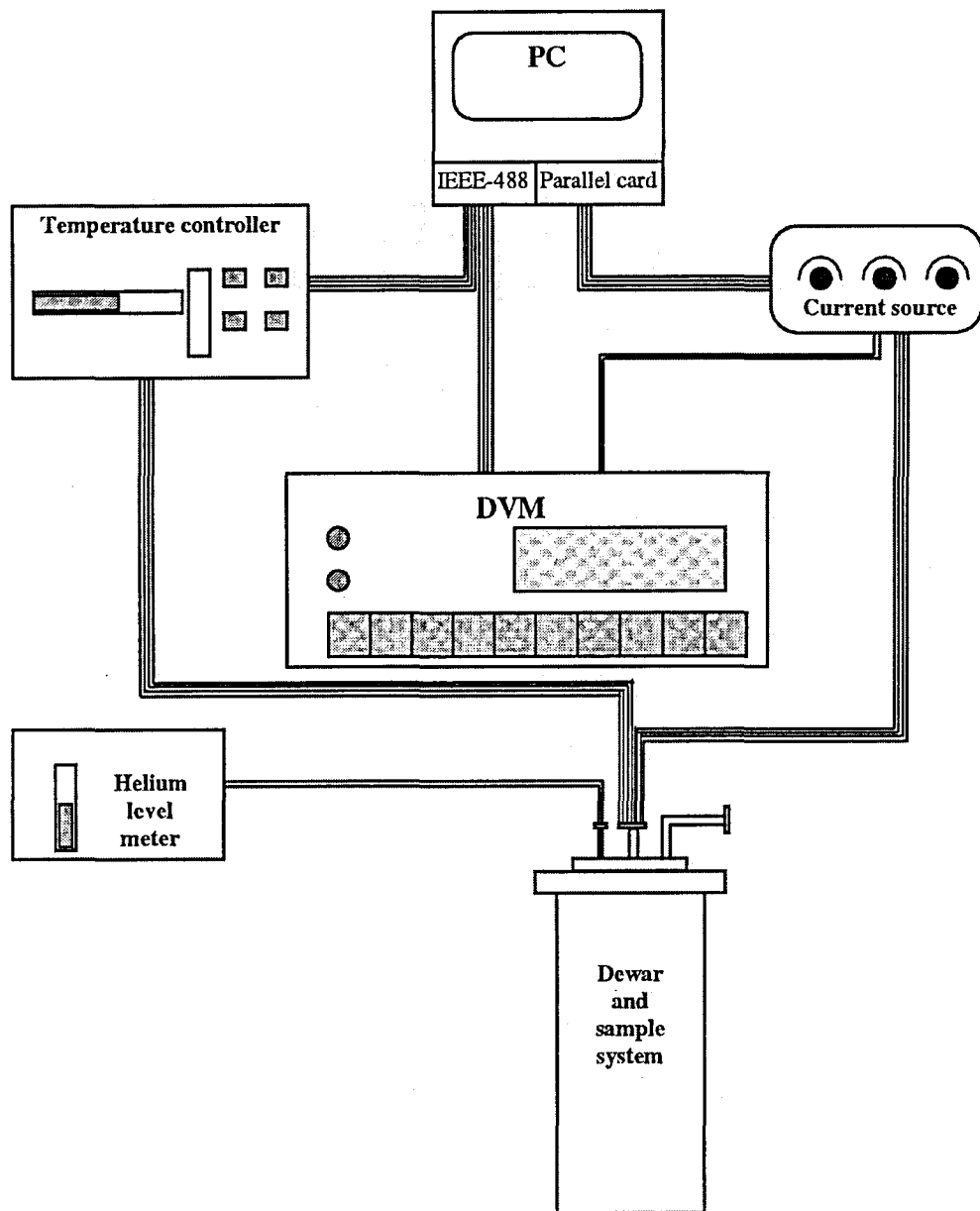


Figure 5.8: Layout of equipment and data acquisition pathways [5.2]

5.4 Shield Temperature Control

The shield temperature control has a significant impact on the measurement of the specific heat. The shield temperature is to be chosen in such a way, as to minimise influence on the sample.

It was found that if the shield temperature is stable at a given value, the sample temperature settles with time at a value slightly below the shield temperature. Therefore, in preparation for one specific heat measurement cycle, the shield temperature is set slightly above the starting temperature. This will almost eliminate the pre-heat drift. While performing a specific heat measurement run, the shield temperature has to be raised from the previous set point to a new value. The

aim is to reach the target temperature as fast as possible. At the same time, it is to ensure that a possible overshoot in shield temperature (which can cause instabilities in the sample temperature) is minimised. This is achieved by using the feedback control system of the TEMPERATURE CONTROLLER MODEL DRC-93C.

5.4.1 Feedback Control

Feedback is the process of measuring the controlled variable (here temperature) and using that information to influence the value of the variable, to be controlled, in this case the shield heating power [5.6].

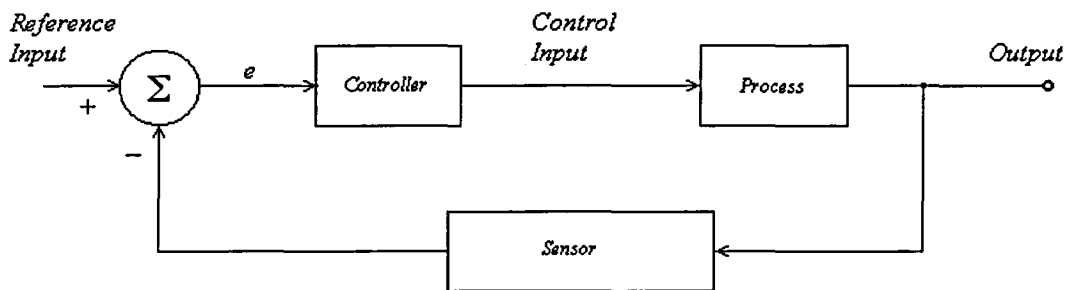


Figure 5.9: Block diagram of a process with a feedback controller

In the Model DRC-93C this is realised by the PID-technique.

The Proportional–Integral–Derivative (PID) control was first described by Callendar et al. [5.7]. It is developed in order to control processes which are not only highly complex but also non-linear and subject to relatively long time delays between actuator and sensor. Today, PID controller is the most common by used control algorithm. Most feedback loops are controlled by this algorithm or minor variation of it [5.8].

The control equation for the PID algorithm has three variable terms, a proportional (*P*), and integral (*I*) and a derivative (*D*) term. The equation that is used in the Model DRC-93C to alter the heater output is given by:

$$\text{Heater Output} = P \left[e + \frac{1}{I} \int e dt + D \frac{de}{dt} \right] \quad (5.2)$$

where *e* is the error, which is defined as the difference between the setpoint and feedback temperature.

$$\text{Error } (e) = \text{Setpoint} - \text{Feedback Reading} \quad (5.3)$$

Every system requires its specific PID settings. Changing these variables for best control is called tuning (see also section 5.4.3 Tuning PID Parameter). The different impacts of these three parameters will be discussed in the following sections.

5.4.1.1 Proportional (P)

The proportional term, also called gain, scales the heater output in proportion to the error on the setpoint and must have a greater value than zero for the control loop to operate.

$$\text{Heater Output (P)} = P e \quad (5.4)$$

If one only uses proportional feedback control, P can be either chosen

- a) too high, which will lead to an oscillation of the temperature around the setpoint

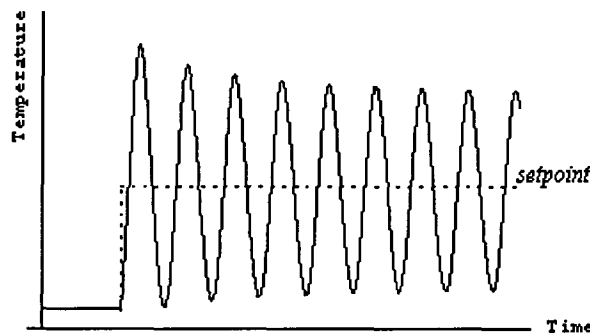


Figure 5.10: P only (too high)

- b) too low, which results in a smooth curve for T

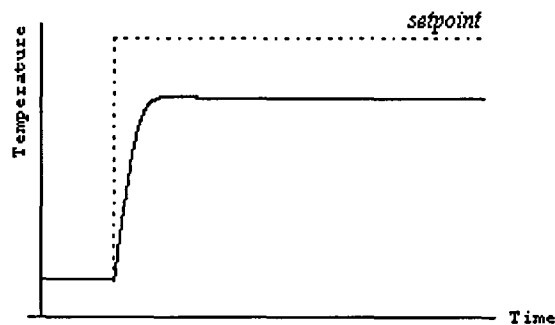


Figure 5.11: P only (too low)

c) at the optimum. In that case, the system stabilises after a few damped oscillations.

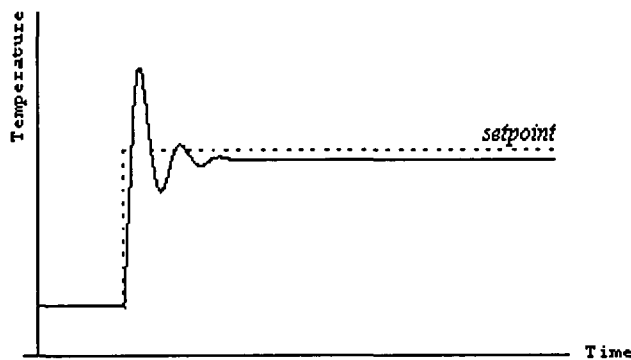


Figure 5.12: P only

However, even with P set to its optimum, with only proportional feedback control, it is not possible to stabilise the system at the setpoint. The reason for it is that, if the system temperature is equal to or higher than the setpoint, the error is zero and therefore the heater output is zero as well. Therefore, the system is cooling down. If P is too high the control will respond too rapidly and the heater output is significantly larger than the cooling rate and T overshoots. This will result in an oscillation of the system temperature around the setpoint. The temperature of any stable state, where the heater output is equal to the cooling power of the surrounding, is lower than the setpoint.

5.4.1.2 Integral (I)

The integral term, known as reset, integrates the system temperature error over a pre-set time period.

$$\text{Heater Output (I)} = P \frac{1}{I} \int e dt \quad (5.5)$$

The main function of the integral action is to make sure that the process output agrees with the setpoint in the steady state. If the error is zero, the integral component will have a constant output. The integral setting is proportional to the period of oscillations or time constant of the cryogenic system. If this time constant is determined, I can be estimated.

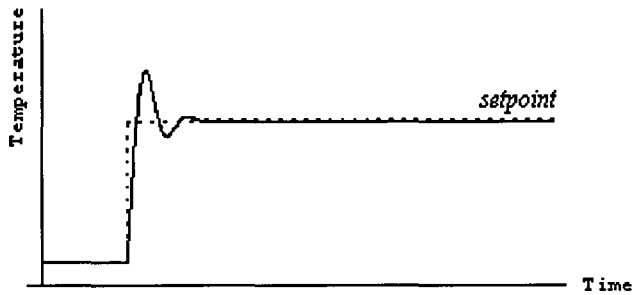


Figure 5.13: P & I

5.4.1.3 Derivative (D)

The rate, as what the derivative is also entitled, acts on the change in error with time to get its contribution to the output.

$$\text{Heater Output} = P D \frac{de}{dt} \quad (5.6)$$

By reacting to a fast changing error signal, the derivative can work to boost the output when the setpoint changes quickly, reducing the time it takes for temperature to reach the setpoint. It can also see the error decreasing rapidly when the temperature nears the setpoint and reduces the output for less overshoot. The derivative term can be useful in a fast changing system. In steady state control, it is often turned off because it reacts too strongly to small disturbers. Like the integral term, it is related to the time constant of the system.

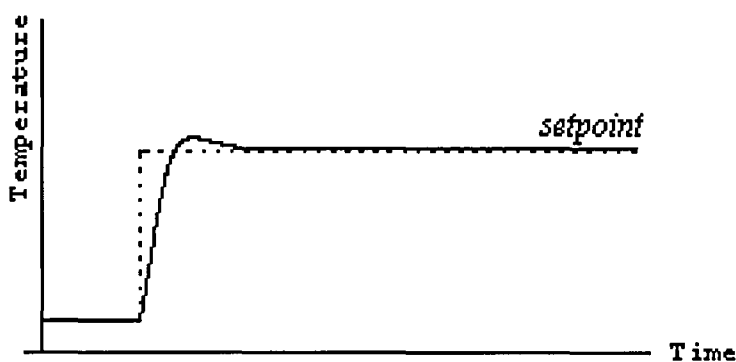


Figure 5.14: PID

5.4.2 Heater Power Range

In addition to the PID control parameters, the heater current can be altered. The Model DRC-93C provides five different current settings labelled R1 (min) to R5 (max), which correspond to a heater output multiplier of, 10^{-4} , 10^{-3} , 10^{-2} , 10^{-1} and 1 respectively. Selecting the appropriate heater current will be disamed in 5.4.3 Tuning PID Parameter.

5.4.3 Tuning PID Parameter

Since in general there is only little information provided concerning system's properties with respect to temperature, finding the optimal PID settings is done by trail and error. For estimate the best control settings one aims to find the balance between reaching the set temperature as fast as possible (to minimise total run time) while minimising the overshoot. In addition to the PID control parameters, heater rang is the main control parameter. It multiplies the heater power which is to calculate using equation (5.2). It was found that if the multiplier was chosen too high, for example range R3 at 85K the overshoot was enormous. On the other hand, when chosen too low, for example R2 at 150.2 K the shield temperature did not reach the setpoint. In fact, the shield temperature dropped. The appropriate heater current multiplier was found to be

- R1 for $T < 14$ K,
- R2 for $14 \text{ K} < T < 88$ K and
- R3 for $88 \text{ K} > T$.

Following the "textbook procedure" for manually tuning PID parameters (see [5.5], [5.6], [5.7] or [5.8] for example), an appropriate value for P has to be found first, for which the system temperature settles after a few oscillations just below the given setpoint. Then, an integral setting is to be chosen, which corresponds to the period of the observed oscillations. Finally, the derivative parameter can be found which is also connected to the time constant of the oscillation.

However, the particular system under consideration does not behave as it is predicted from textbooks. The effect of P only is investigated for $T = 150.2$ K and shown in Figure 5.15. Even for maximum value of P (P99) the system does not oscillate, instead it settles after an overshoot. This behaviour is due to the pre selected heater output range. Therefore, the proportional and integral parameter combination had to be estimated (see Figure 5.16). As a first guess P45 (as a value a little below half the scale) and I10 are chosen. Since the shield temperature oscillates around the setpoint, they seam not to be totally off. In order to lower the overshoot a smaller proportional parameter is set for the second run. To study the

effect of I, it is set to half of the previous value (P30 I5). The overshoot did not respond as rapidly as it was expected. For the next run, the priority was given to the new integral setting, I3, and P set to P40. The result of this combination of parameters seemed promising, as a smaller overshoot and damped oscillation of the shield temperature was observed. Obviously, in this case, the important parameter is I, so it was lowered again by one. The value of P was kept unchanged (P40 I2). The response of the shield temperature to these parameters is nearly perfect and the overshoot and the temperature drift are within the range of the stabilisation criteria¹¹. Thus, the values of P and I approached are considered to be appropriate. From the manual [5.5] it is suggested, that the value for the derivative should be of the order of $I/4$. This leads to P40 I2 D0.5. The effect on the setting of the shield temperature is to produce an overshoot, which is slightly higher than for $D=0$. Therefore, P40 I2 D0 is taken as the final PID parameter setting for temperatures around 150.2 K.

Optimisation procedures similar to the one described above are carried out for a series of temperatures, namely for 12.5K, 85 K and 150.2 K, shown in Figure 5.18, 5.17 and 5.16. For temperatures in-between, the PID parameters were estimated by interpolating. The fine-tuning was carried out for temperatures points separated by 5 to 10 degrees.

¹¹ see paragraph 5.5.2 Preparation Phase

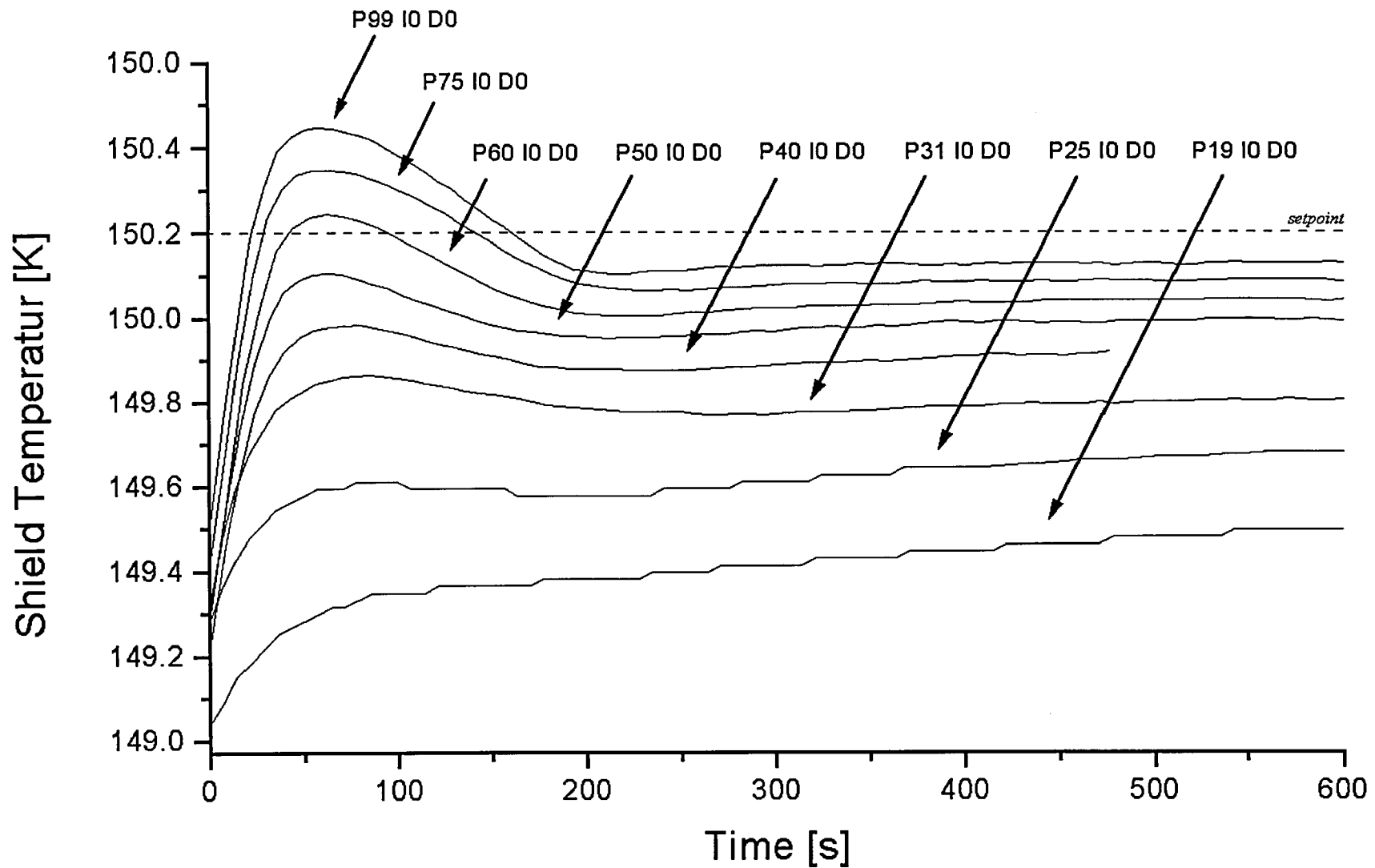


Figure 5.15: Shield Temperature Control at 150.2 K with different P parameters

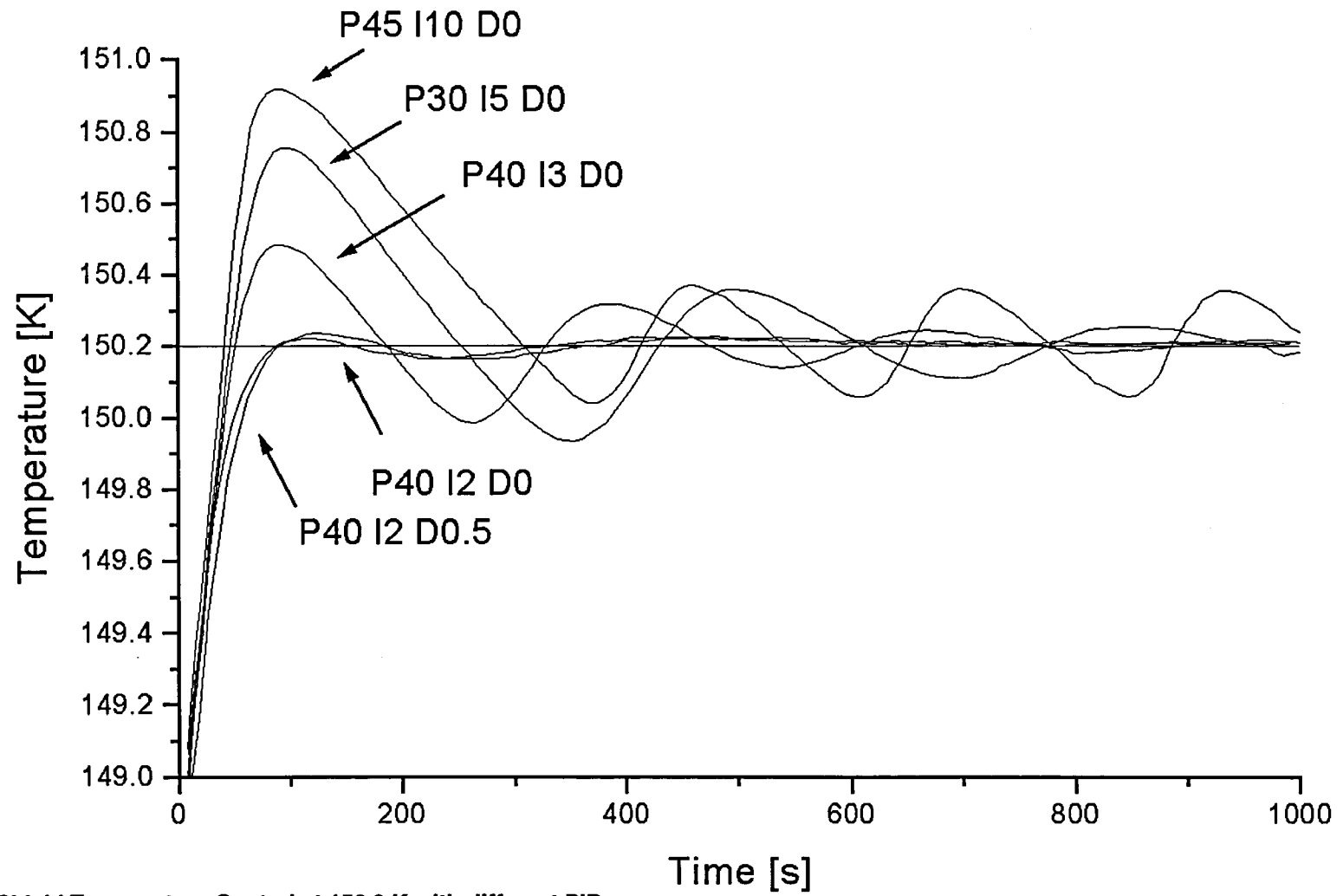


Figure 5.16: Shield Temperature Control at 150.2 K with different PID parameters

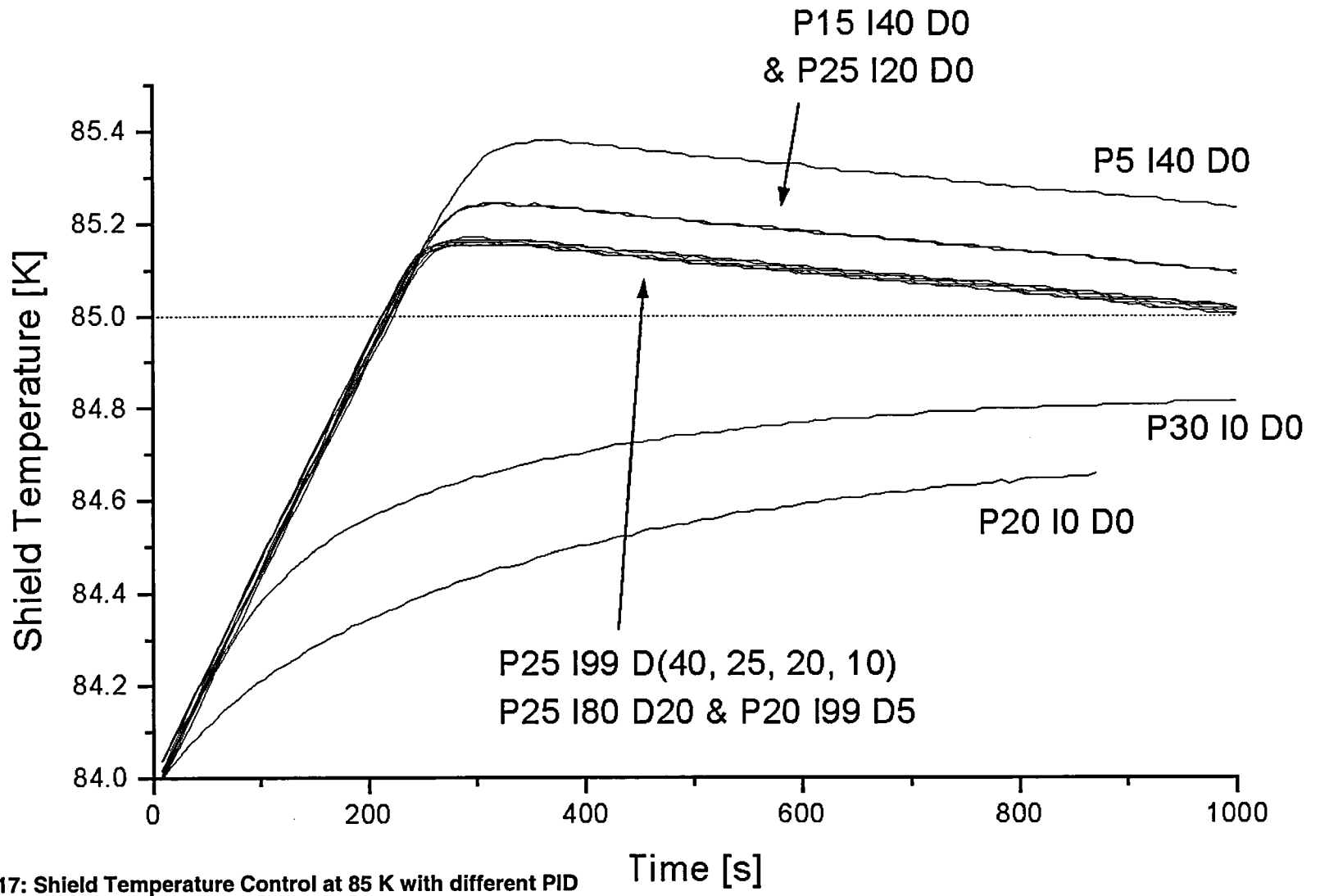


Figure 5.17: Shield Temperature Control at 85 K with different PID parameters

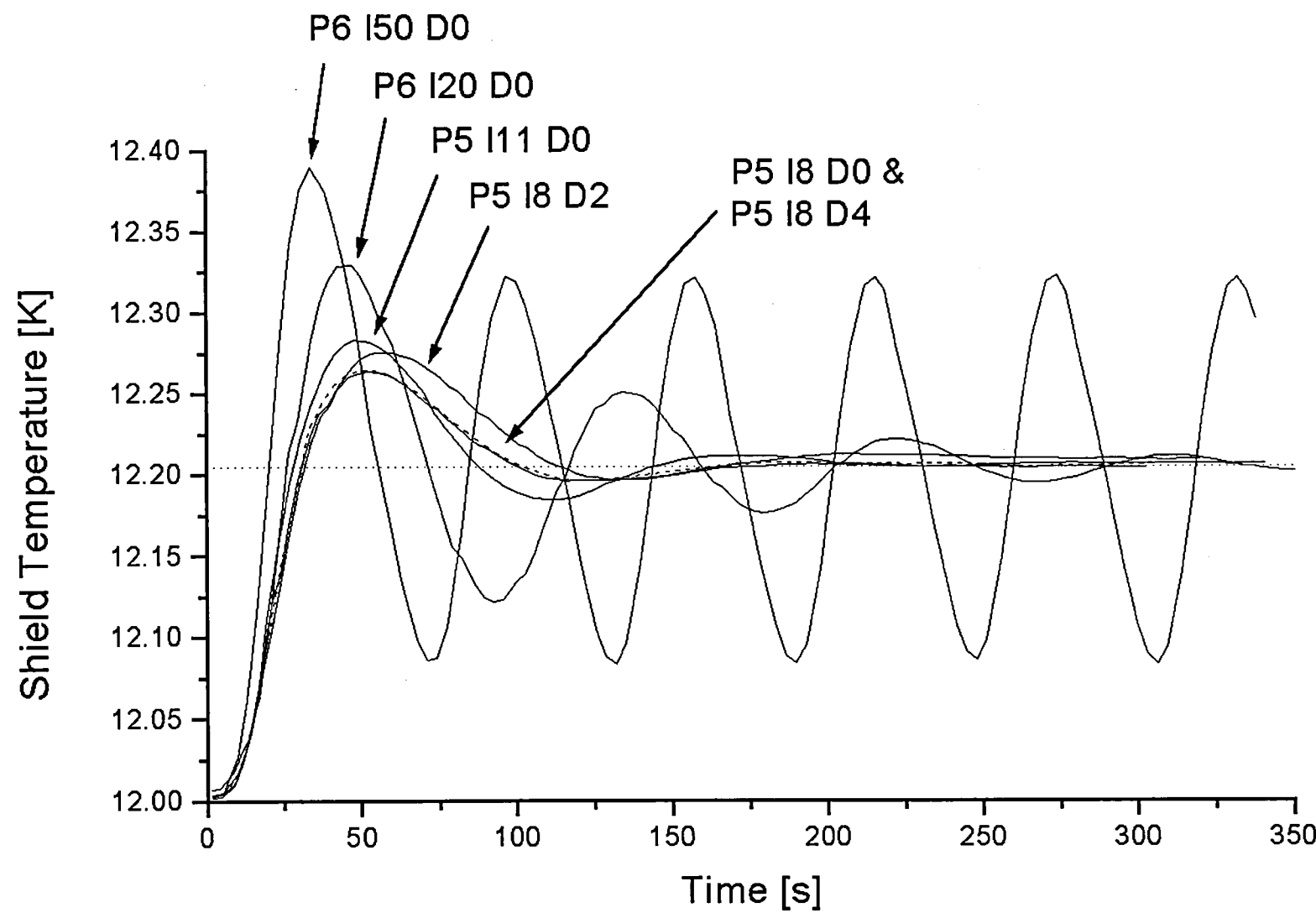


Figure 5.18: Shield Temperature Control at 12.205 K with different PID parameters

5.5 Software

In order to run continuous measurements and due to long duration of the measurement, it was essential to automate the data acquisition. The software was originally written by Parsons and Taylor [5.2]. It was further modified for the purpose of this investigation. The software for the control of the calorimeter was written in Microsoft QuickBasic 4.50.

For economical reasons, it is possible to use Nitrogen instead of Helium as cooling liquid for temperatures above $\sim 80\text{K}$. Since the cooling power is different for each of the two cooling liquids, the necessary temperature control parameters alter. Therefore, two nearly identical programs were written with temperature control parameters appropriate to the temperature range under consideration. The low temperature version covers the temperature range from 4 K to 100 K cooled with liquid Helium, while the high temperature version uses liquid Nitrogen and ranges from 77 K up to 210 K. The overlap of $\sim 20\text{K}$ is considered to be sufficient to prove smooth transition between both data sets obtained.

Due to the different tasks, the program is divided into four separate sections. These are described in the following. A flow diagram representing the data acquisition program is presented in Figure 5.19: The construction of the data acquisition program.

5.5.1 System Set-up Phase

This is the initial phase of the program. The communication to the measurement devices checked. This involves declaring input and output of the DVM, current source as well as the temperature controller. Sample characteristics such as name, weight, molar mass and grease mass are recorded. Also within this pre-run phase, the operator is asked for the initial experimental run parameters including, temperature range, initial heating current, heating time and drift time. Finally, the recording files are declared and their headers are written (which include the sample characteristics).

5.5.2 Preparation Phase

Prior to the measurement phase, communication to the peripherals is initialised. Run parameters like heating current and heating time are defined. The shield control phase begins with writing set-point and PID parameters to the temperature controller. The set-point is chosen between the starting temperature of the sample before the energy input and the expected finishing temperature. The shield is considered stable, if the shield temperature is within the range of set-temperature

± 0.1 K and the temperature drift is smaller than ± 50 mK/min. As the computer waits for the shield to become stable, it is checking the shield temperature every 20 seconds and determine the drift for that period. If the observed shield temperature and drift are within the predetermined limits, than the shield is considered stable passes. Five passes in a row are required for the continuation to the sample preparation phase.

The sample catch-up routine allows time for the sample temperature to stabilise. It is considered stable if the temperature drift is smaller than ± 25 mK/min. This criterion is checked every 20 seconds and has to be fulfilled for 60 seconds before the program starts the measurement phase.

5.5.3 Measurement Phase

In Figure 5.1 the variation of the sample temperature during one measuring cycle is presented. To determine pre- and post-heat temperature a drift time is given the system. During this time interval, the sample temperature is measured every two seconds.

At the start of this part of the program, the computer timer is reset, so all calls to the timer are made with respect to this starting time. After the pre-drift period the heat pulse is supplied. While heating, the heating current and voltage are measured frequently. As noted before, the temperature measured at the sample sensor position is still rising for a short time after the end of heat pulse. A delay time, which depends on sample properties and on the shield temperature, is implemented to allow temperature to equilibrate throughout the sample, sample holder and temperature sensor.

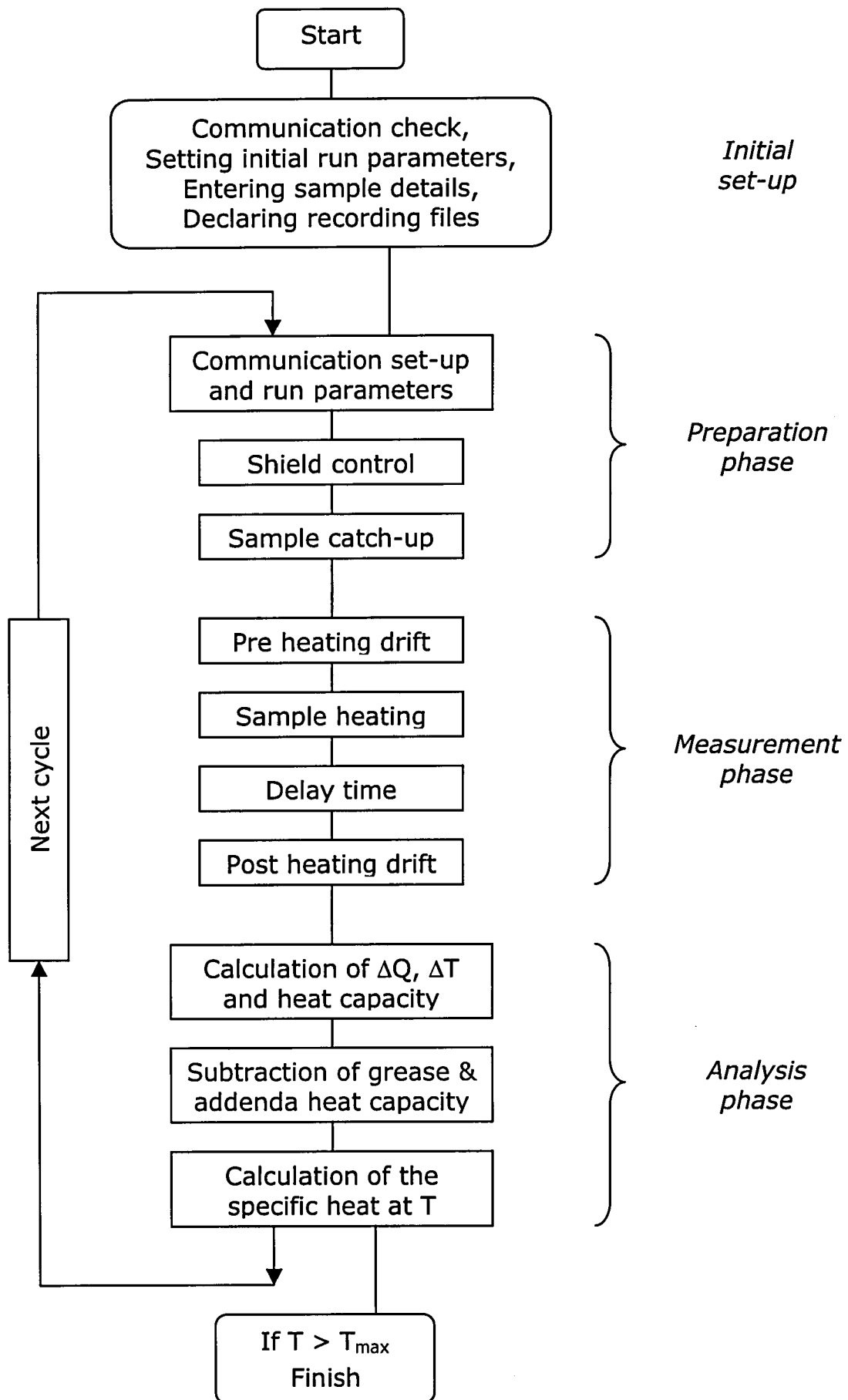


Figure 5.19: The construction of the data acquisition program

5.5.4 Analysis Phase

The analysis routine calculates the energy input ΔQ into the sample system, the temperature rise ΔT and the heat capacity $C(T)$ of the system.

The energy input into the sample system is evaluated by averaging the heater current I and heater voltage U and multiplying it by the heating time ΔT .

$$\Delta Q = IU * \Delta T \quad (5.7)$$

In order to compute the sample temperature rise, the drift curve data is subjected to a linear regression fit. Prior to this, the time t scale is normalised to have the reference point at the middle of the sample heating phase. Thus, the intercept of the pre- and post-drift extension of the fits at $t=0$ yields the pre- and post-heating sample temperatures. The change in temperature is determined as the difference between pre- and post-heating temperatures.

$$\Delta T = T_{pre} - T_{post} \quad (5.8)$$

This allows to estimate the temperature rise while correcting for any heat loss. The gradient of the linear regression is a measure of this heat loss and it is used as an indication for obtaining the appropriate delay time. The heat capacity of the sample system is calculated as the ratio $\Delta Q / \Delta T$ (equation (5.1)).

The heat capacity is then corrected by subtracting the heat capacity of addenda and grease (see also sections 5.6.1 and 5.6.2 respectively), to obtain the sample heat capacity. Finally, the specific heat of the sample material is put onto an absolute scale by normalising the sample heat capacity using the ratio of molar mass divided by sample mass. The temperature to which this value of the specific heat corresponds to is taken to be temperature midway between pre and post heating temperatures.

$$C_p(T) = C(T) \frac{M}{m} \quad (5.9)$$

5.6 Heat Capacity of the Calorimeter

The heat capacity of the sample system contains in addition to the sample heat capacity other contributions from all additional components to the calorimeter, such as the grease, used to mount the sample. The values of these contributions can be determined separately. There are then subtracted from the total heat capacity of the sample system to extract the heat capacity of the pure sample.

5.6.1 Addenda

The addenda consists of a sapphire plate, the sample heater, the sample thermometer (CERNOX™ temperature sensor model CX-1050-SD, SN X05304) and the Apiezon N high vacuum grease (see also Figure 5.2). Because the heat capacity of the grease depends on the amount of grease used for mounting the sample, it is discussed separately in the next paragraph (5.6.2).

The heat capacity of the remaining addenda is shown in Figure 5.20 for the temperature interval [4, 210] K. The absence of any saturation for temperatures up to 210 K is a result of the high Debye temperature of sapphire. This contributes to the minimisation of the addenda heat capacity at low temperatures.

The addenda heat capacity in the temperature range of the low temperatures version of the control software is fitted by a polynomial fit of the order of 9, represented by

$$C_{Addenda} = \sum_{i=0}^9 A_n T^n \quad (5.10)$$

The coefficients of this fit are given in Table 5.1. The deviation of the measured Addenda heat capacity from the fit is shown in Figure 5.21.

The data are nearly equally spread around both sides of the zero line, indicating that the fit is reasonable. The spread also indicates the resolution of the measurement.

In order to fit the curve using a polynomial regression for temperatures from 80 K to 210 K, the graph is to be divided into sections, which fitted individually. To avoid such fractionating, the data were interpolated using a cubic spline fit [5.4].

The addenda heat capacity at a given temperature can be calculated as described and the obtained value is subtracted to eliminate the addenda contribution to the heat capacity measured.

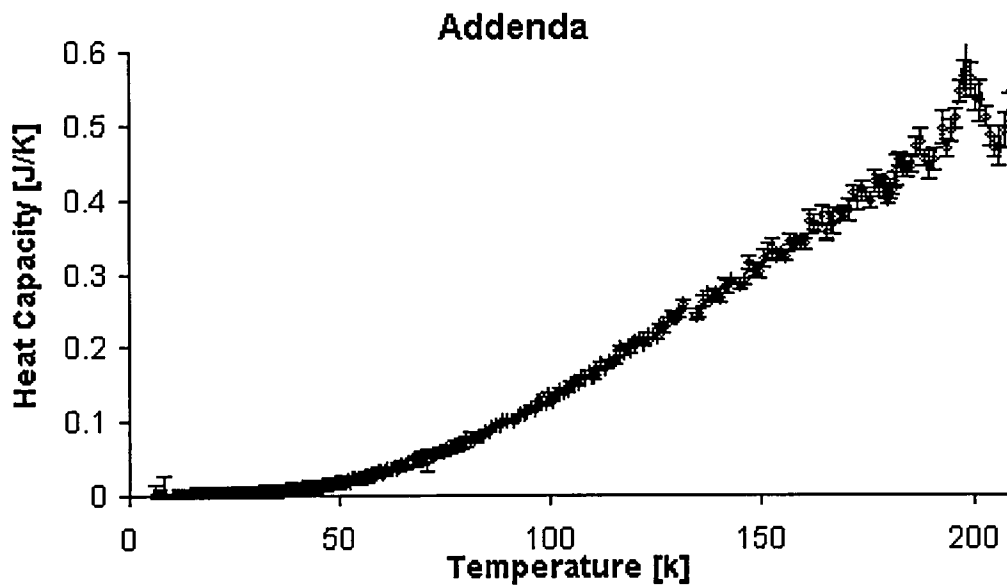


Figure 5.20: Addenda Heat Capacity without Grease

Table 5.1: Polynomial Coefficients, equation (5.10), representing the Heat Capacity of the Addenda for T [4,100]K, units [J/K]

Parameter	Value
A_0	$2.6895 \cdot 10^{-4}$
A_1	$-2.44017 \cdot 10^{-5}$
A_2	$2.13087 \cdot 10^{-5}$
A_3	$-1.98211 \cdot 10^{-6}$
A_4	$9.84904 \cdot 10^{-8}$
A_5	$-2.71518 \cdot 10^{-9}$
A_6	$4.72425 \cdot 10^{-11}$
A_7	$-5.02856 \cdot 10^{-13}$
A_8	$2.95372 \cdot 10^{-15}$
A_9	$-7.29039 \cdot 10^{-18}$
Standard Deviation:	$7.94481 \cdot 10^{-4}$

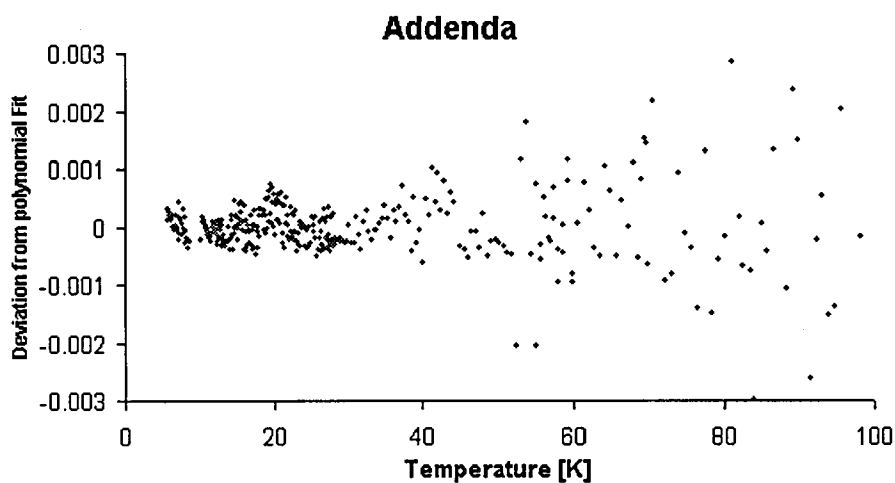


Figure 5.21: Deviation of the Addenda Heat Capacity from Polynomial Fit

5.6.2 Apiezon N High Vacuum Grease

Apiezon N high vacuum grease is used to provide good thermal contact between the sample and the sapphire disk. Its heat capacity is widely reported in the literature ([5.9] to [5.13]). Although the amount of grease used is small (< 10 mg) its contribution is significant, especially in the region above 200 K where specific heat anomalies are present.

For temperatures below 80 K, the polynomial equations and coefficients published by W. Schnelle et al. [5.13] is used. Above 80 K, especially in the temperature range where the specific heat anomaly is observed, because of the greater number of data points published by Bunting et al. [5.9], this data is used. The data obtained by Bunting where interpolated using a cubic spline interpolation.

Specific Heat of Apiezon N high vacuum grease

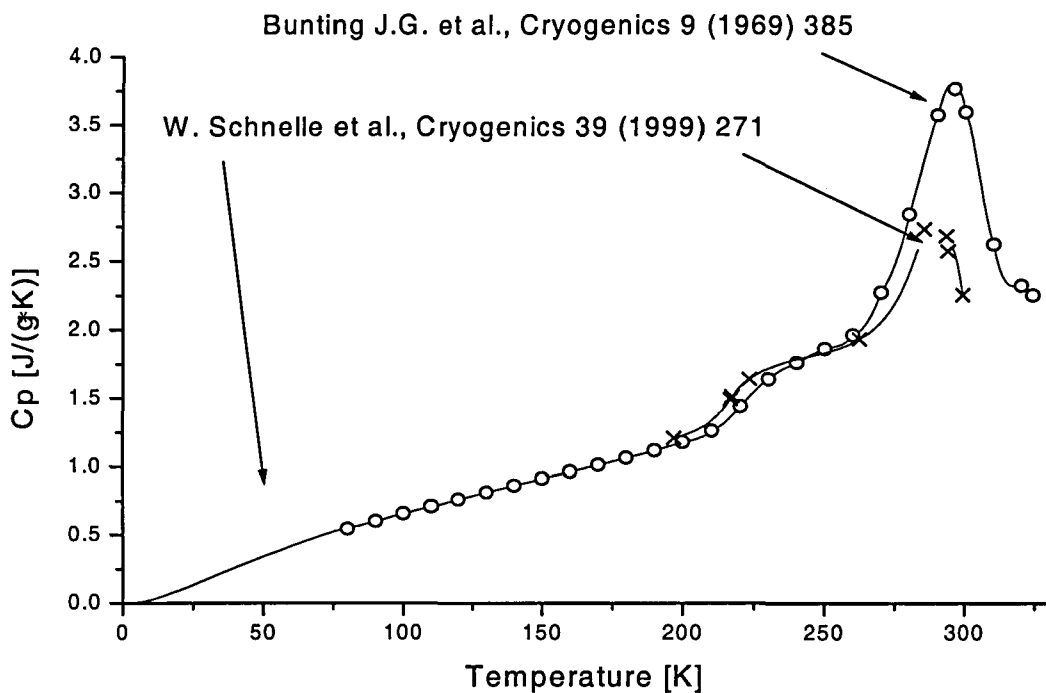


Figure 5.22: Specific Heat of Apiezon N high vacuum grease

5.7 Copper Standard

By using a sample whose thermal properties are well known, the accuracy of the calorimeter can be investigated. The heat capacity of pure copper (99.995%, Johnson and Mathey) is measured over the temperature range from 4 to 210 K. The result is shown in Figure 5.23. The data obtained are in good agreement with previous investigations, for example see work by Martin [5.14].

Copper is a nonmagnetic material. If the low temperature data are within the Debye model of the heat capacity (see section 4.2.2 *ff*), then the data should be well represented by equation (4.61)

$$C_p = \gamma T + \beta T^3 \quad (5.11)$$

where γT is the conduction electron contribution and βT^3 represents the phonon contribution to the specific heat. The low temperature data for $T < 14$ K are presented in the form C_p/T vs. T^2 in Figure 5.24.

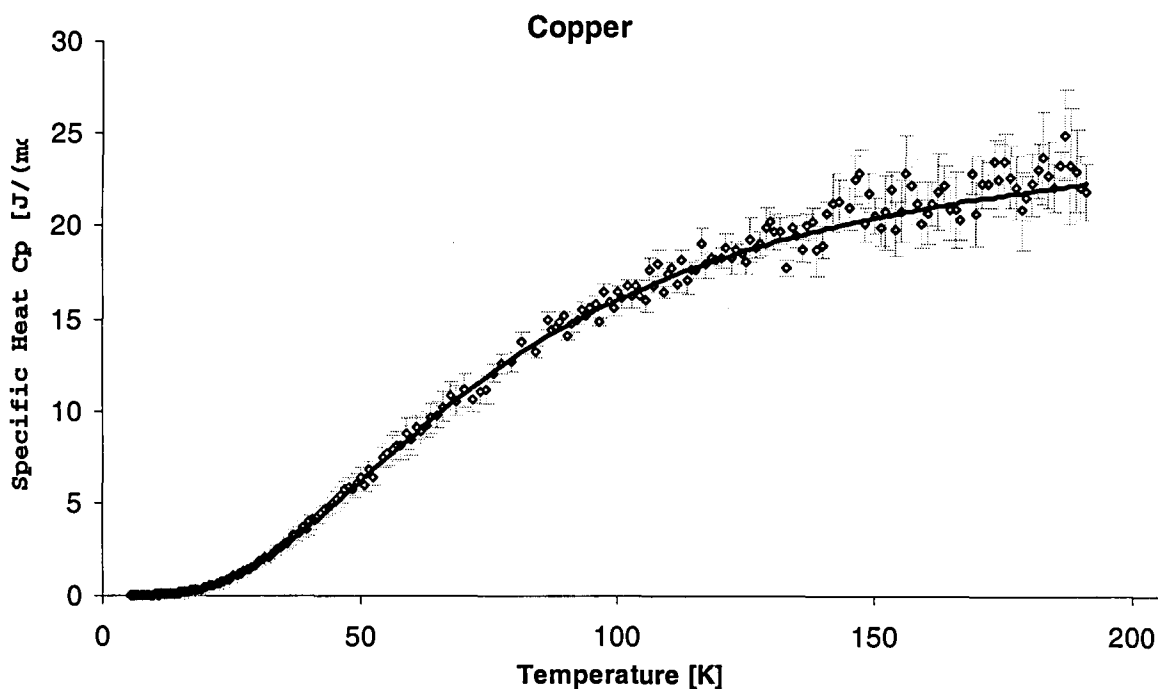


Figure 5.23: Specific Heat of Copper, Solid Line: D. L. Martin [5.14]

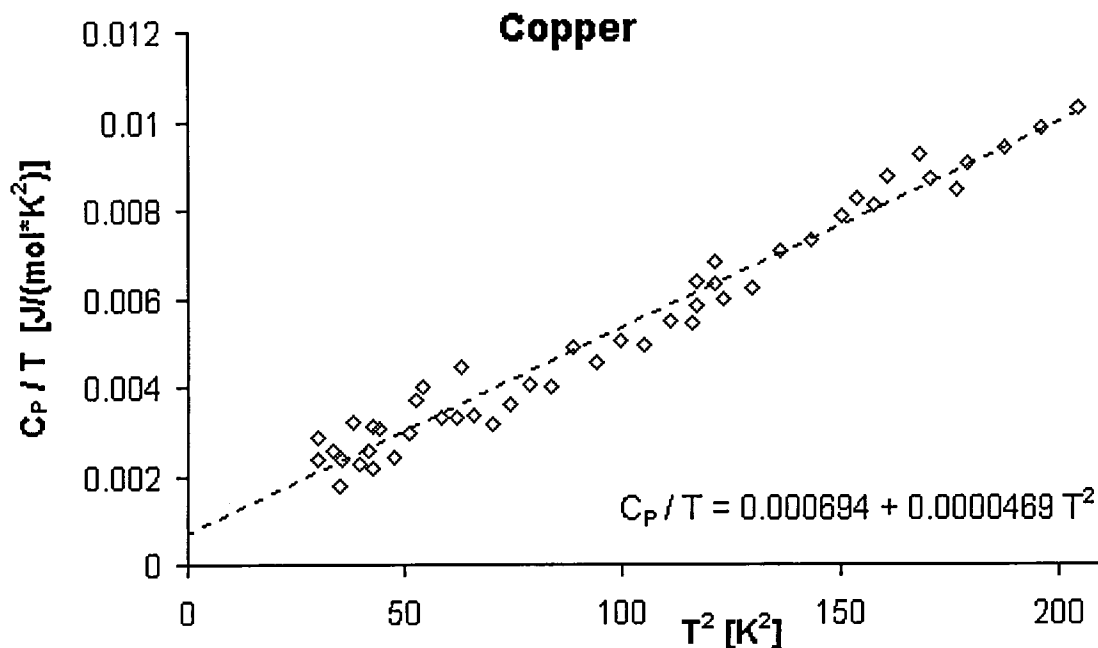


Figure 5.24: Low Temperature Specific Heat of Copper, Dashed Line: Least Square Linear Regression

A least square linear regression of the low temperature data plotted in the form C_p/T vs. T^2 reveals the coefficient of the conduction electron contribution to the specific heat $\gamma = (0.694 \pm 0.139) \text{ mJ}/(\text{mol K}^2)$ and the coefficient of phonon contribution $\beta = (0.0469 \pm 0.0013) \text{ mJ}/(\text{mol K}^4)$. From the slope β of the graph in Figure 5.24, the low temperature approximation to the Debye temperature can be calculated using (4.39).

$$\Theta_D(0) = \sqrt[3]{\frac{1}{\beta} \frac{12}{5} N k_B \pi^4} \cong \sqrt[3]{\frac{1}{\beta} 234R} \quad (5.12)$$

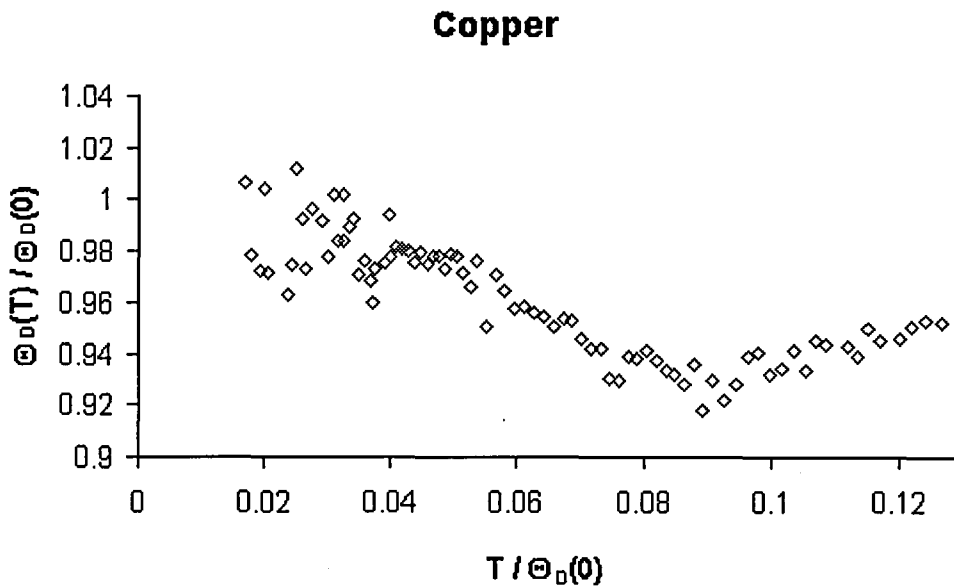
where R is the molar gas constant. This leads to a Debye temperature of Copper of $\Theta_D(0) = (346 \pm 3) \text{ K}$. Even though, Θ_D is slightly higher than expected, the values obtained are in reasonable agreement with those, given in the literature and presented in Table 5.2.

Table 5.2: Comparison of the experimental specific heat coefficients of Copper

γ [mJ/(mol K ²)]	$\Theta_D(0)$ [K]	Reference
0.694±0.139	346±3	this work
0.723±0.012	341±1	Parsons [5.2]
0.505	343	Kittel [5.15]
0.688±0.5	343.8±0.5	Corak et al [5.16]
	315	Ashcroft [5.17]

Because the Debye result (4.37) is viewed more general than a rough interpolation formula, the practice arose of fitting observed heat capacities with (4.37) by allowing Θ_D to depend on temperature. The thermal dependence of the Debye temperature of Copper is shown in Figure 5.25.

As expected, at lowest temperatures $\Theta_D(T)$ approaches the value of $\Theta_D(0)$. A minimum is observed at approximately $T/\Theta_D(0) \approx 0.9$ after which $\Theta_D(T)/\Theta_D(0)$ rises to a plateau. Such a temperature dependence of the Debye temperature is generally observed in several metallic and non-metallic elements [5.17].

**Figure 5.25: Debye Temperature as a Function of Temperature**

5.8 Summary

The design and automation of a calorimeter based on the Nernst heat pulse method was discussed. The working of the control software was described. The contributions to the measured heat capacity from the empty calorimeter and Apiezon N high vacuum grease were pointed out and their values estimated to isolate the heat capacity of the sample.

To test the functioning of the calorimeter, the specific heat of a well known element, in this case Copper, was measured. The specific heat of Copper obtained from the measurement is in reasonable agreement with theoretical models and the various coefficients from the models are comparable with those given in the literature.

The spread of data points around the polynomial fit of the Addenda heat capacity gives an indication of the accuracy of the calorimeter.

5.9 References

- [5.1] Hussen, W.Y., "Investigation of the Thermal and Magnetic Properties of some Ce based Heavy Electron Systems". Diss. Loughborough University, (1990)
- [5.2] Parsons James M., "An Investigation of the Thermal Properties of some Strongly Correlated Electron Systems", Diss. Loughborough University, (1998)
- [5.3] Swartz J.M., "Temperature Measurement and Control", LakeShore Catalogue, Lake Shore Cryotronics, Inc., (1999)
- [5.4] Press W.H., Flannery B.P., Teukolsky S.A., Vetterliin W.T., "Numerical Recipes, The Art of Scientific Computing", Cambridge University Press, (1986)
- [5.5] Instrument instruction manual for DRC-93 temperature controller, Lakeshore™ Cryotronics, (1988)
- [5.6] Franklin Gene F., Powell J. David, Emami-Naeini Abbas, "Feedback Control of Dynamic Systems" 3rd ed., Addison-Wesley Publishing Company, Inc., (1994)
- [5.7] Callender A., Hartree D.R., Porter A., "Time Lag in Control System", Philos. Trans. R. Soc. London, A. London: Cambridge University Press, (1936)
- [5.8] Ångström Karl J., Hägglund Tore, "PID Controllers", (Rev. ed. of: "Automatic tuning of PID controllers") Instrument Society of America, (1995)
- [5.9] Bunting J.G., Ashworth T., Steeple H., "The specific heat of Apiezon N grease", Cryogenics, 9, p 385-386, (1969)
- [5.10] Bevolo A.J., "Heat capacity of Apiezon N grease from 1 to 50 K", Cryogenics, 14, p 661-662, (1974)
- [5.11] Wun M., Phillips N.E., "The low temperature specific heat of Apiezon N grease", Cryogenics, 15, p 36-67, (1975)
- [5.12] Schink H.J., v.Lohnesyen H., "Specific heat of Apiezon N grease at very low temperature", Cryogenics, 21, p 591-592, (1981)
- [5.13] Schnelle W., Engelhardt J., Gmelin E., "Specific heat capacity of Apiezon N high vacuum grease and of Duran borosilicate glass", Cryogenics, 39, p 271-275, (1999)
- [5.14] Martin D.L., " "tray" type calorimeter for the 15-300 K temperature range: Copper as a specific heat standard in this range", Rev Sci Instrum. 58 (4), (1987)
- [5.15] Kittel Ch., "Einführung in die Festkörperphysik" 12. Auflage, R.Oldenburger Verlag Muenchen Wien (1999)
- [5.16] Corak S., Garfunkel M. P., Satterthwaite C. B., Wexler A., "Atomic Heats of Copper, Silver, and Gold from 1°K to 5°K", Phys. Rev. 98, 1699-1707 (1955)
- [5.17] Ashcroft N.W., Mermin N.D., "Solid State Physics", Saunders College Publishing, (1976)

6 SAMPLE PREPARATION AND CHARACTERISATION

6.1 Sample Preparation

Samples were prepared by the repeated melting of the appropriate quantities of starting elements in an argon arc furnace. The furnace was built in house and consists of a small chamber, a water-cooled copper table and a tungsten-electrode, which is also used to flip the samples before re-melting. All starting materials were of a purity of at least 99.95% and placed on the furnace table in reverse order to their melting temperature.

The system was flushed at least 5 times with argon and then left under an argon atmosphere with a pressure of ~ 0.2 bar. To remove any remaining oxygen Titanium is melted for ~ 1 min using the arc. If the Titanium is still shiny after melting, the atmosphere is considered clean. The cold copper table prevents the melting of the bottom of the sample thus avoiding copper contamination. All samples were melted at least 4 times and furnace cooled. From each compound, the weight loss after melting is listed in Table 6.1. While melting Pd_2YbIn , the sample exploded, which caused the huge weight loss.

From each sample, an approximately 1g piece was cut off by spark erosion for the specific heat measurement. The rest was crushed into powder with a grain size smaller than $100 \mu\text{m}$ using a steel pestle and mortar. Both, powder and specific heat samples were annealed for ~ 4 days at 800°C and quenched in ice water with the exception of the Pd_2NdIn sample which was slow cooled for 13 hours.

Table 6.1: Sample Preparation and Structure

	Weight	Weight loss after melting	Sample weight for specific heat measurement	Structure	Literature
Pd_2LaIn	Sample by Babateen [6.1]			$P6_3/mmc$	$P6_3/mmc$ [6.2]
Pd_2CeIn	5g	0.03%		$P6_3/mmc$	
Pd_2NdIn	10g	0.27%		$P6_3/mmc$	
Pd_2HoIn	5g	0.91%	1.10890g	$Fm\bar{3}m$	$Fm\bar{3}m$ [6.3]
Pd_2ErIn	10g	0.55%		$Fm\bar{3}m$	$Fm\bar{3}m$ [6.3]
Pd_2YbIn	5g	6.64%*	1.1309g	$Fm\bar{3}m$	$Fm\bar{3}m$ [6.3]
Pd_2LuIn	5g	1.04%	0.7649g	$Fm\bar{3}m$	$Fm\bar{3}m$ [6.3]

*The weight loss is caused by a sample explosion while melting.

6.2 X-Ray Diffraction

In order to resolve structural details of a crystal lattice, the wavelength of the observation radiation (X-ray, electrons, neutrons) must be of the order of the lattice parameter or smaller.

X-ray radiation is located at the high-energy end of the electromagnetic spectrum.

It can be classified according to its wavelength

- X-rays with a wavelength between 0.12 Å (Ångström) and 1.2 Å are called "hard X-rays"
- X-rays with a wavelength between 1.2 Å and 12 Å are called "intermediate X-rays"
- X-rays with a wavelength between 12 Å and 120 Å are called "soft X-rays"

Since the lattice parameters of the investigated materials are of the order of a few Ångström, as reported by Babateen [6.1] and Xue [6.2], intermediate X-rays were used.

6.2.1 Experimental Set-up for X-ray Diffraction

The X-ray diffraction measurements are made using a powder diffraction set-up employing a standard Philips X-ray source. A broad focus PW2 103/100 copper radiation tube is used in conjunction with a PW 1050/25 goniometer. A proportional detector PW 1965/20/30 is fixed on the diffractometer axis. The X-ray system is remotely controlled by a PC, using the software package Sietronics PW1050 diffraction automation SIE 122D. The X-ray tube is powered using a voltages of $U_x = 40$ kV and a current of $I_x = 20$ mA, it emits $\text{Cu } K_{\alpha}^{12}$ radiation. The $\text{Cu } K_{\beta}$ radiation component was suppressed by the use of a nickel filter. As a result of using the $\text{Cu } K_{\alpha 1}\text{-}K_{\alpha 2}$ doublet, reflection peaks split, especially for higher angles. The scans are performed such, that the beam hits the sample surface under an angle ϑ while the detector is placed at an angle 2ϑ with respect to the transmitting beam. Sample and detector are moving by a preselected angular step, keeping the ratio $\vartheta / 2\vartheta$ constant. The exposure time for each step is constant. Scans are performed in the range $20^\circ < 2\vartheta < 85^\circ$. In order to obtain the lattice parameter, the diffraction patterns are analysed using FullProf¹³, a computer program for structure profile refinement.

¹² wavelengths $\lambda_{\alpha 1} = 1.540562$ Å ($K_{\alpha 1}$) and $\lambda_{\alpha 2} = 1.544390$ Å ($K_{\alpha 2}$) respectively

¹³ Version 3.5d Oct98-LLB-JRC by Juan Rodriguez-Carvajal, it has been initiated by the program of Wiles & Young, J. Applied Cryst. 14, 149 (1981)

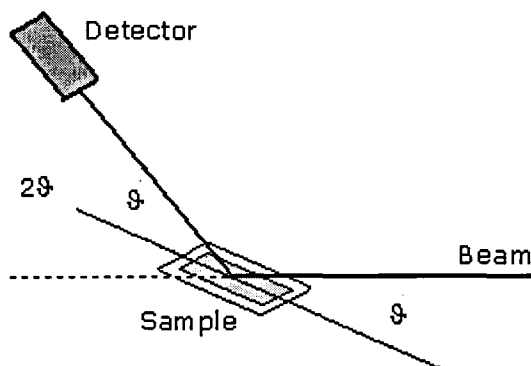


Figure 6.1: X-ray Set-up, schematic

Since the samples are mounted on an aluminium holder, for some patterns diffraction of aluminium are observed.

Aluminium (Al) has a face-centred cubic (fcc) unit cell, with space group symmetry $Fm\bar{3}m$. To identify reflections of the aluminium holder in the X-ray diffraction pattern of the investigated materials, a scan of the empty holder was performed. The diffraction pattern is shown in Figure 6.2. The lattice parameter obtained from the Aluminium holder reflection is given in Table 6.2.

Table 6.2: Lattice parameter of the Aluminium

	Lattice Parameter [\AA] (FullProf)	Literature [\AA] [6.3]
Aluminium Holder	4.0507 ± 0.0007	4.0488

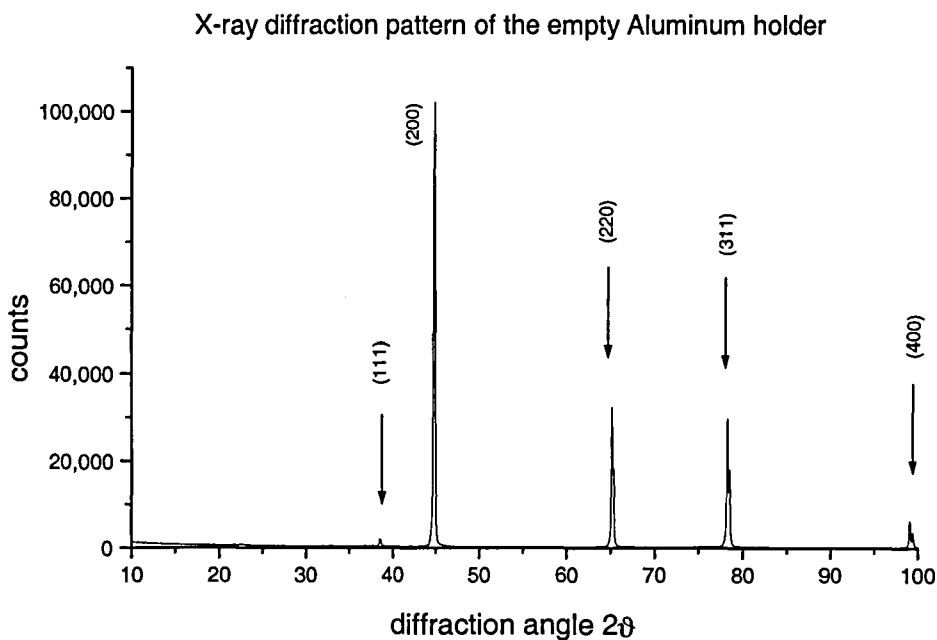


Figure 6.2: X-ray pattern of the empty holder (Aluminium)

6.2.2 Structure of Pd₂[Heavy Rare Earth]In Alloys

The basic formula for the structural determination of a material from diffraction peaks is the Bragg' law:

$$\lambda = 2 d_{hkl} \sin(\vartheta) \quad (6.1)$$

where λ is the wavelength of the radiation, 2ϑ the detector angle of the reflecting planes with Miller indices (hkl) and d_{hkl} is the separation of two parallel lattice planes with equal indices. For cubic lattices d_{hkl} can be calculated as

$$d_{hkl}^2 = \frac{a^2}{h^2 + k^2 + l^2} \quad (6.2)$$

where a is the lattice parameter. Therefore, for cubic samples, (6.1) can be written to

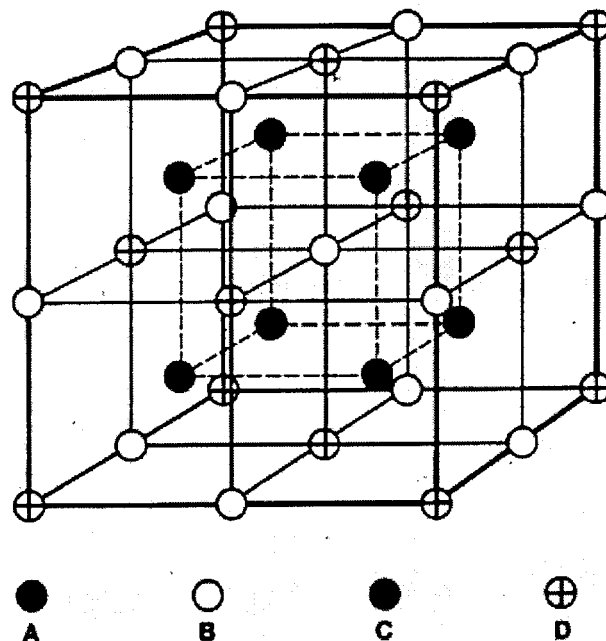
$$\lambda^2 = \frac{4a^2}{h^2 + k^2 + l^2} \sin^2(\vartheta) \quad (6.3)$$

The atomic scattering factor f is a property of the elements. The structure factor is the collection of all the waves scattered by the individual atoms of one unit cell. It is given by

$$F_{hkl} = \sum_{n=1}^N f_n \cdot e^{2\pi i(h \cdot u_n + k \cdot v_n + l \cdot w_n)} \quad (6.4)$$

where the summation is carried out over all atoms of the unit cell. (hkl) are again the Miller indices of the reflecting plane, u_n, v_n, w_n are the positions of the n^{th} atom in the unit cell and f_n its atomic scattering factor. The exponential term describes constructive and destructive interference of the scattered waves of the individual atoms. The total intensity of a peak, specified by (hkl) , is proportional to $|F_{hkl}|^2$.

As shown by M.O. Babateen [6.1], Pd₂[RE]In containing heavy Rare Earth metals are Heusler alloys at room temperature. Heusler alloys are ternary intermetallic compounds, at the stoichiometric composition X₂YZ [6.5]. The Heusler L2₁ structure can be considered to composite of four interpenetrating fcc sublattices with atoms A (X), B (Y), C (X) and D (Z) at locations (0, 0, 0), (1/4, 1/4, 1/4), (1/2, 1/2, 1/2) and (3/4, 3/4, 3/4) respectively (see Figure 6.3).

Figure 6.3: L₂₁ Heusler alloy structure

The Heusler L₂₁ structure is the ordered version of Heusler alloys. Heusler B2 is a disordered version with the elements Y and Z being randomly placed at the lattice sites B and D.

The structure factor is given as

$$F_{hkl} = 4 \cdot \left(f_A + f_B \cdot e^{\pi i(h/2+k/2+l/2)} + f_C \cdot e^{\pi i(h+k+l)} + f_D \cdot e^{\pi i(3h/2+3k/2+3l/2)} \right). \quad (6.5)$$

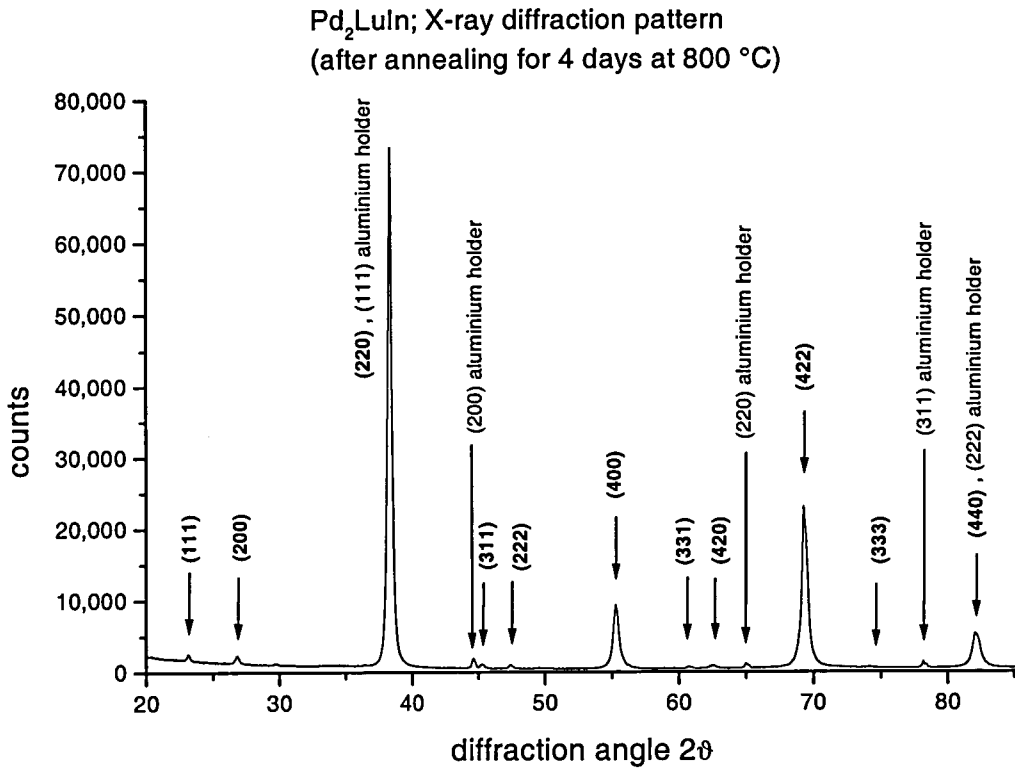
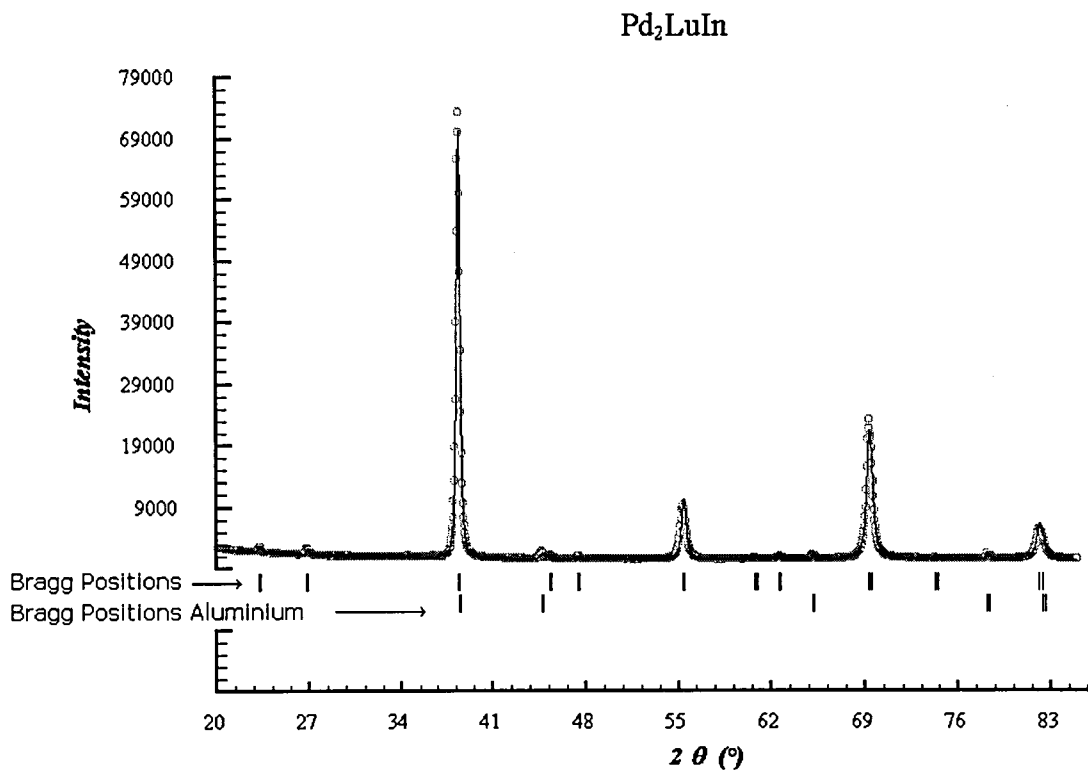
In Pd₂[RE]In Heusler L₂₁ alloys, the A and C sites are occupied by Pd atoms, the B sites by the Rare Earth atoms and the D sites by In atoms. Therefore, equation (6.5) can be investigated for different sets of lattice planes:

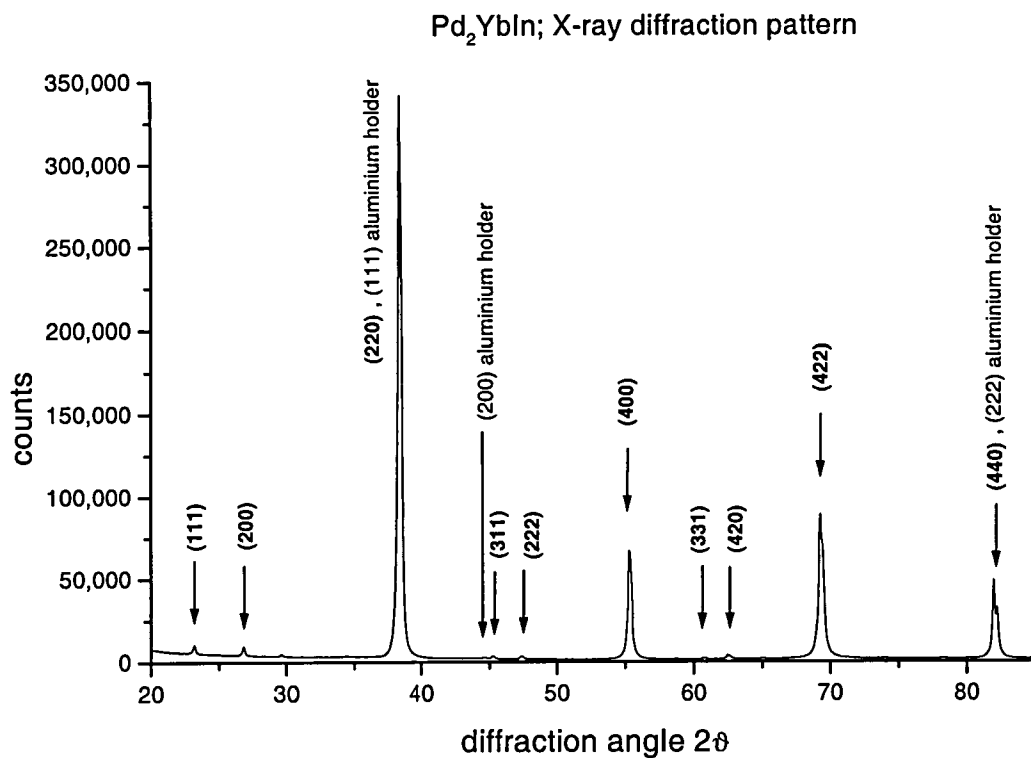
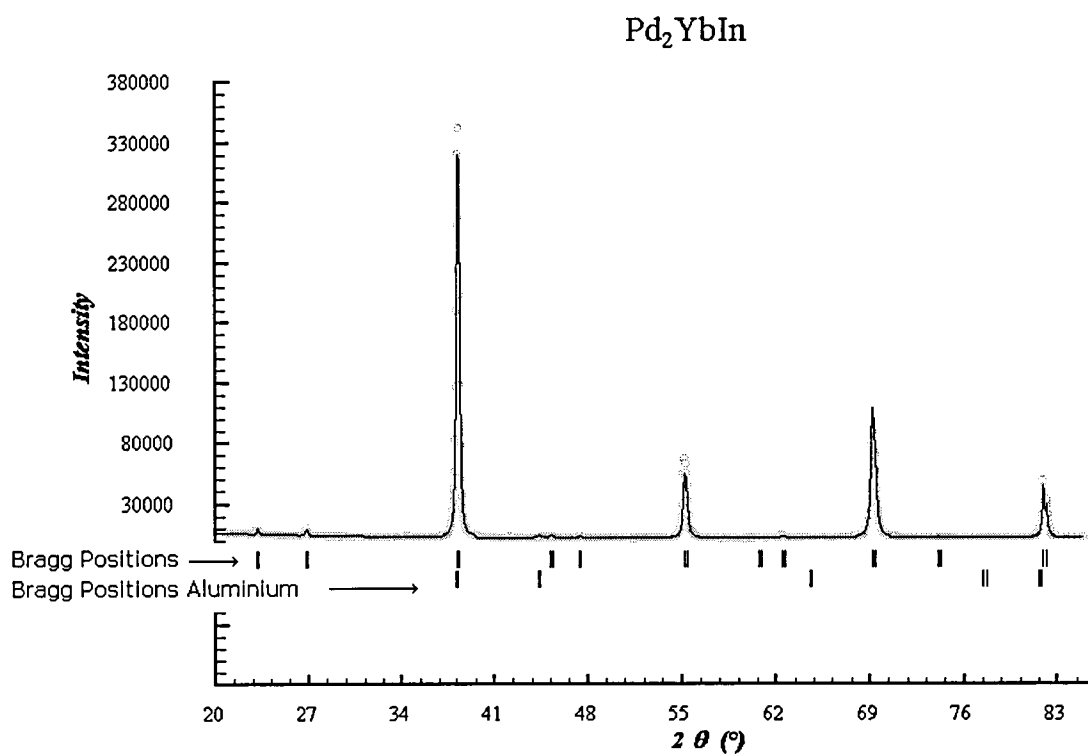
$$1. \ h, k, l \text{ are all odd:} \quad F_{hkl} = 4 |f_{RE} - f_{In}| \quad (6.6)$$

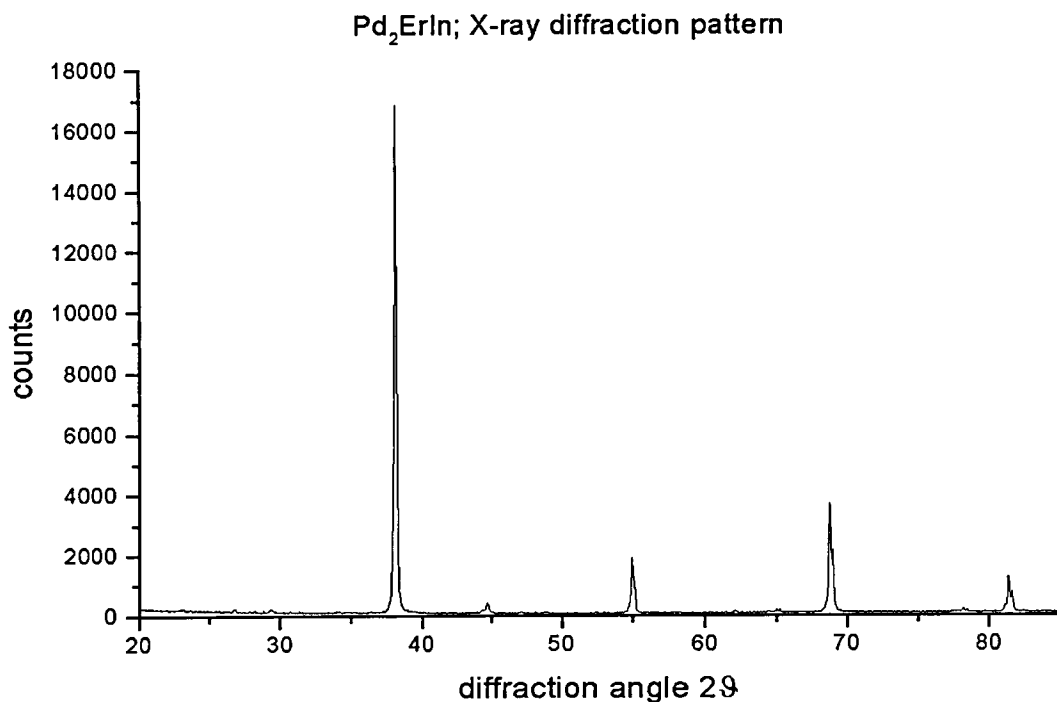
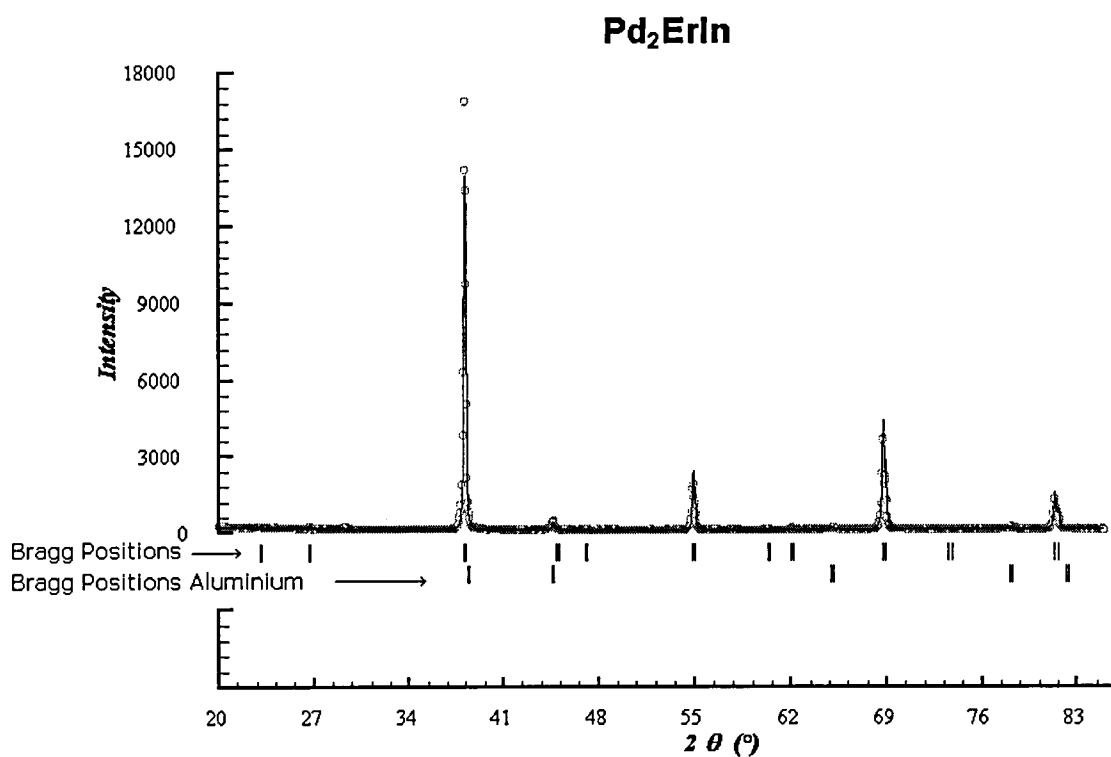
$$2. \ h, k, l \text{ are even and } (h+k+l)/2 = 2n+1: \quad F_{hkl} = 4 |2f_{Pd} - (f_{RE} + f_{In})| \quad (6.7)$$

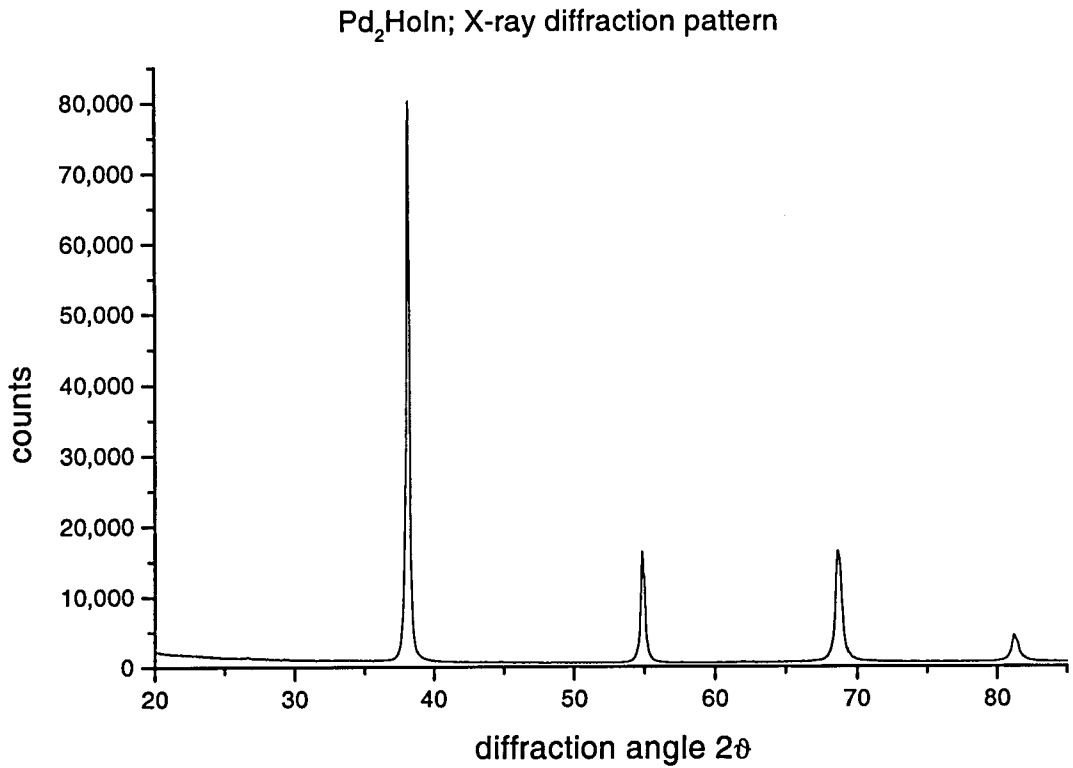
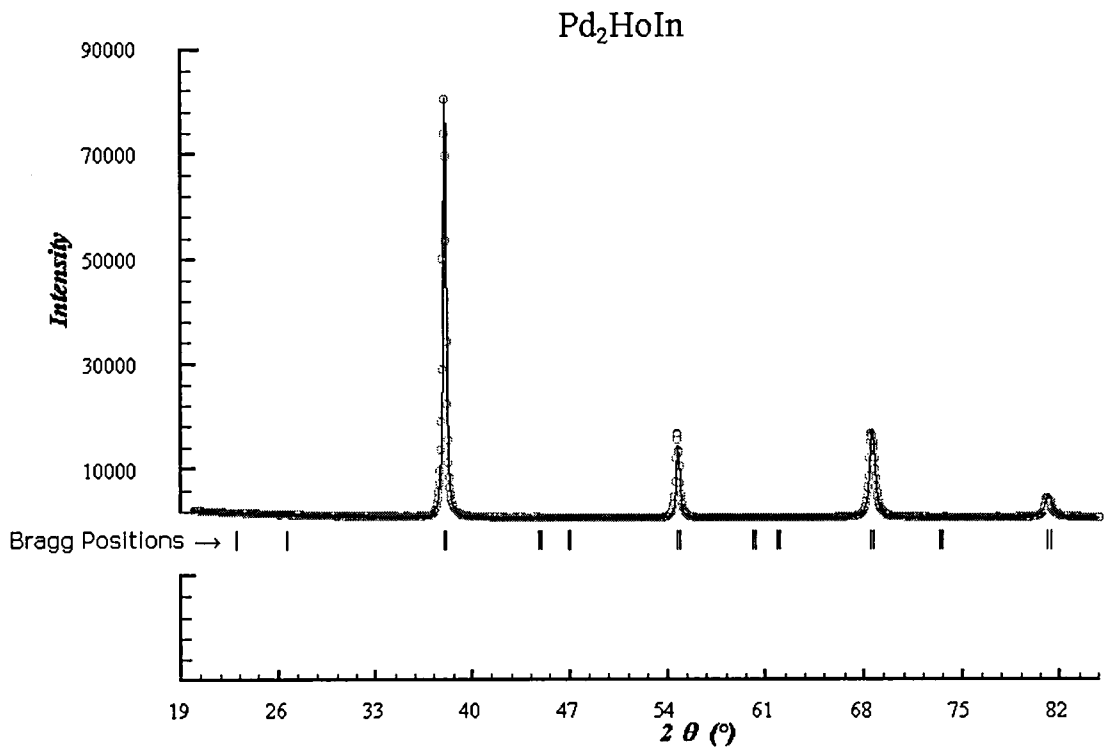
$$3. \ h, k, l \text{ are even and } (h+k+l)/2 = 2n: \quad F_{hkl} = 4 |2f_{Pd} + (f_{RE} + f_{In})| \quad (6.8)$$

The reflections described in case three are called "principal reflections". They are independent of chemical order and occur at the same positions and with the same intensities in the patterns of both, ordered (Heusler L₂₁) and disordered (Heusler B2) alloys. The principal reflections have generally the highest intensities. For Heusler B2 alloys these are the only reflections observed.

Figure 6.4: Pd₂LuIn X-ray diffraction patternFigure 6.5: Pd₂LuIn X-ray diffraction pattern refinement using FullProf

Figure 6.6: Pd_2YbIn X-ray diffraction patternFigure 6.7: Pd_2YbIn X-ray diffraction pattern refinement using FullProf

Figure 6.8: Pd₂ErIn X-ray diffraction patternFigure 6.9: Pd₂ErIn X-ray diffraction pattern refinement using FullProf

Figure 6.10: Pd_2HoIn X-ray diffraction patternFigure 6.11: Pd_2HoIn X-ray diffraction pattern refinement using FullProf

The lattice parameters for these alloys are obtained by solving the Bragg equation for cubic lattices (6.3) and by refining the diffraction pattern using FullProf.

Table 6.3: Lattice parameter for Pd₂[Heavy Rare Earth]In Alloys

	Lattice Parameter [Å]	Lattice Parameter [Å] (FullProf)	Literature [Å]
Pd ₂ HoIn	6.687±0.090	6.7014±0.0005	6.685±0.012 [Babateen]
Pd ₂ ErIn	6.682±0.076	6.6855±0.0003	6.668±0.005 [Babateen]
Pd ₂ YbIn	6.643±0.084	6.646±0.001	6.618±0.011 [Babateen]
Pd ₂ LuIn	6.635±0.067	6.6350±0.0004	6.692 [Parsons]

6.2.3 Structure of Pd₂[Light Rare Earth]In Alloys

Following B.Xue et al. [6.2] Pd₂LaIn crystallises in the hexagonal GdPt₂Sn structure with symmetry $P6_3/mmc$ (space group No. 194 [6.4]). This is an ordered version of the TiAs structure, with fractional atomic co-ordinates given in Table 6.4.

Table 6.4: Atomic Positions of Pd₂LaIn

	Wyckoff Notation	x	y	z
Palladium (Pd)	4(f)	1/3	2/3	0.57732
Palladium (Pd)	4(f)	2/3	1/3	-0.57732
Lanthanum (La)	2(c)	1/3	2/3	1/4
Indium (In)	2(a)	0	0	0

For hexagonal crystals the Bragg-equation (6.3) has to be rewritten to

$$\sin^2(\vartheta) = \frac{\lambda^2}{3 \cdot a^2} \cdot (h^2 + h \cdot k + k^2) + \frac{\lambda^2}{4 \cdot c^2} \cdot l^2. \quad (6.9)$$

According to "International Tables of Crystallography" [6.4], the reflection conditions for alloys with such symmetry are

1. $l = 2n$ or
 2. $h - k = 3n + 1$ or
 3. $h - k = 3n + 2$.
- (6.10)

The structure factor F_{hkl} can be written as

$$F_{hkl} = f_{Pd} e^{2\pi i(h/3+2k/3+lz)} + f_{Pd} e^{2\pi i(2h/3+k/3-lz)} + f_{La} e^{2\pi i(h/3+2k/3+l/4)} + f_{In} \quad (6.11)$$

Taking the symmetry of the crystalline structure ($P6_3/mmc$) and the atomic positions for Pd_2LaIn (Table 6.4) a picture of the unit cell is drawn, see Figure 6.12.

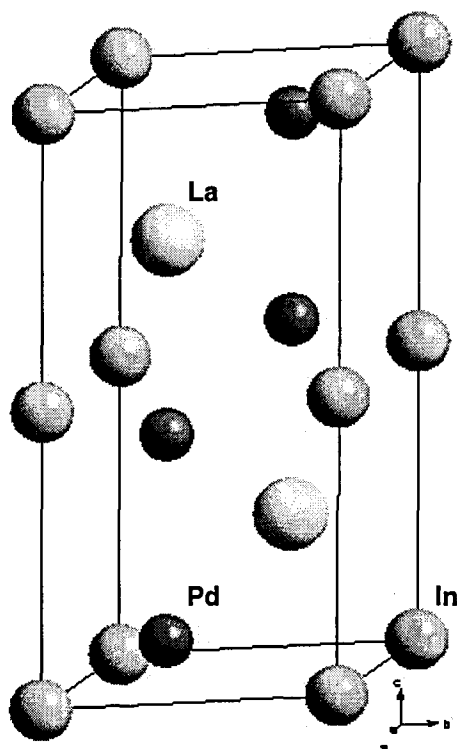
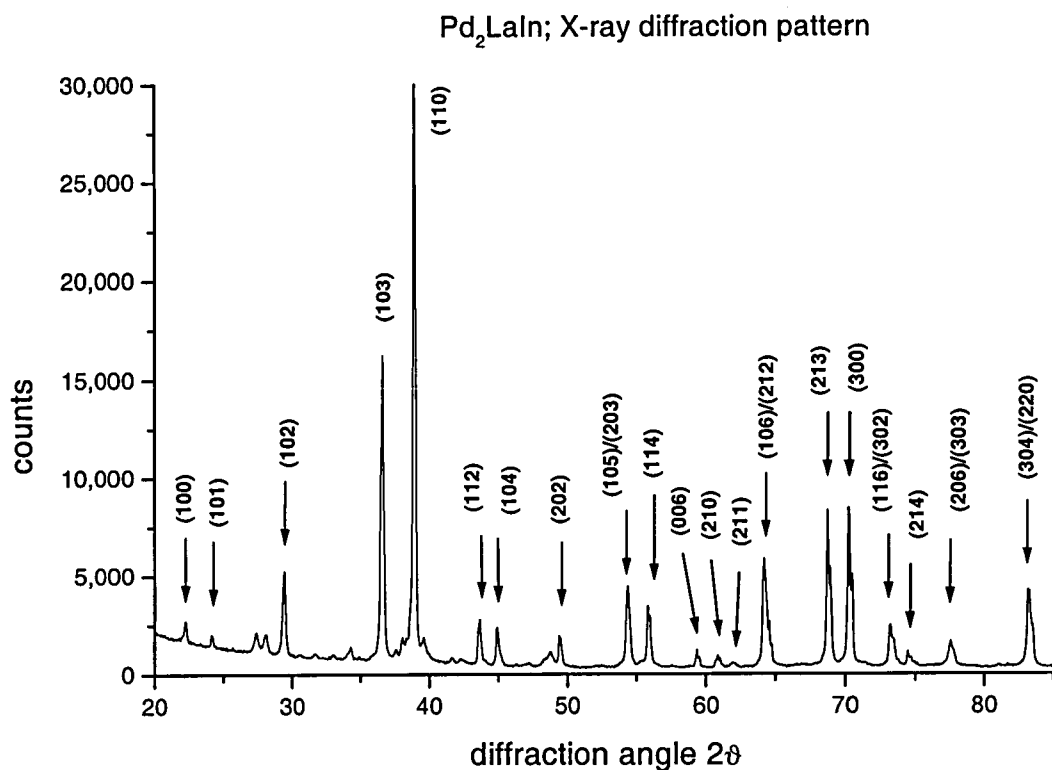
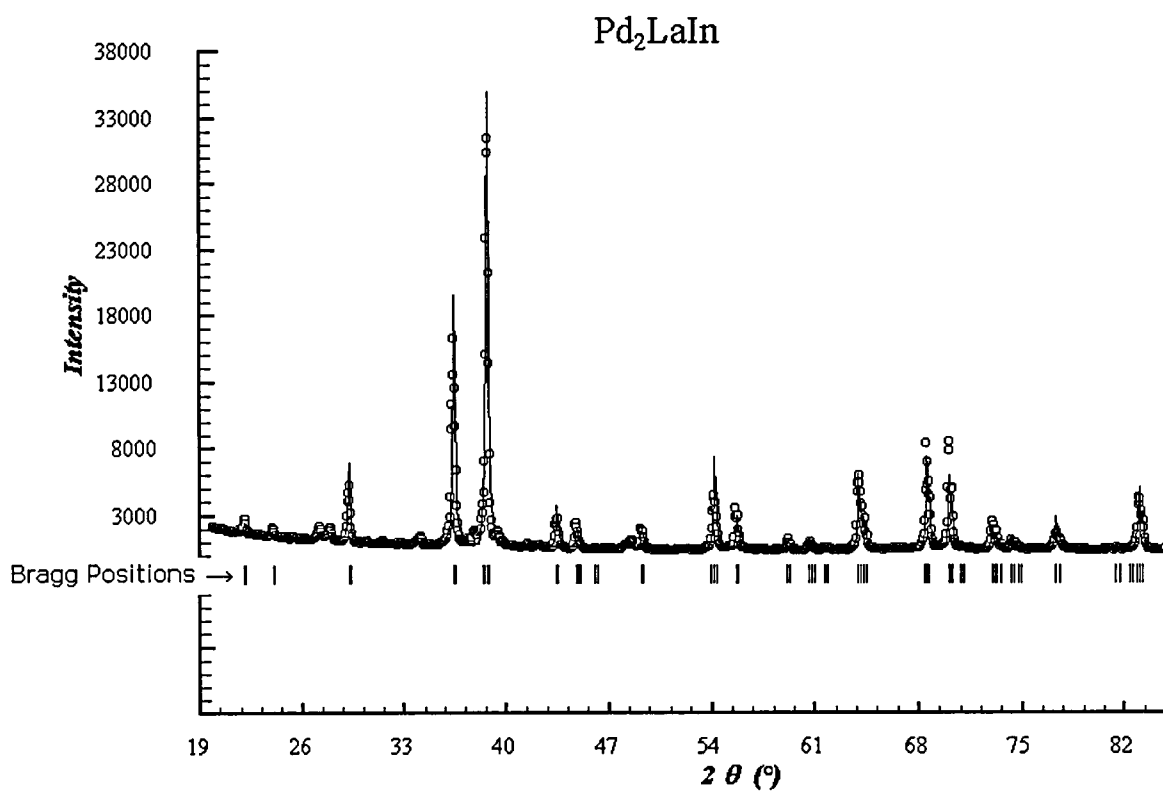


Figure 6.12: Unit cell of $\text{Pd}_4\text{La}_2\text{In}_2$

The crystalline structure of Pd_2LaIn (Xue [6.2]) was also applied to Pd_2CeIn and Pd_2NdIn . The lattice parameters were obtained by calculation and by refinement using FullProf.

Table 6.5: Lattice parameter for $\text{Pd}_2[\text{Light Rare Earth}]\text{In}$ Alloys

	a [Å]	c [Å]	A [Å] (FullProf)	c [Å] (FullProf)
Pd_2LaIn	4.6445(7)	9.3542	(B.Xue et al [6.2])	
Pd_2LaIn	4.641 ± 0.096	9.33 ± 0.36	4.6490 ± 0.0004	9.362 ± 0.001
Pd_2CeIn	4.631 ± 0.109	9.21 ± 0.29	4.6273 ± 0.0004	9.198 ± 0.001
Pd_2NdIn	4.605 ± 0.109	9.05 ± 0.30	4.609 ± 0.002	9.067 ± 0.004

Figure 6.13: Pd_2LaIn X-ray diffraction patternFigure 6.14: Pd_2LaIn X-ray diffraction pattern refinement using FullProf

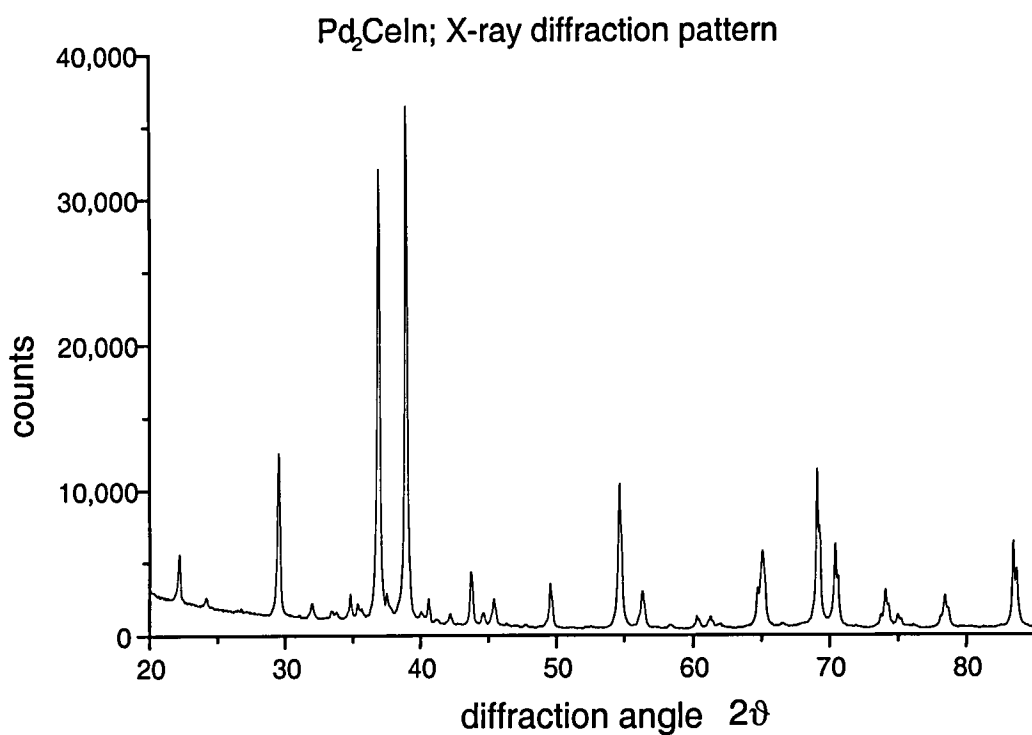


Figure 6.15: Pd₂CeIn X-ray diffraction pattern

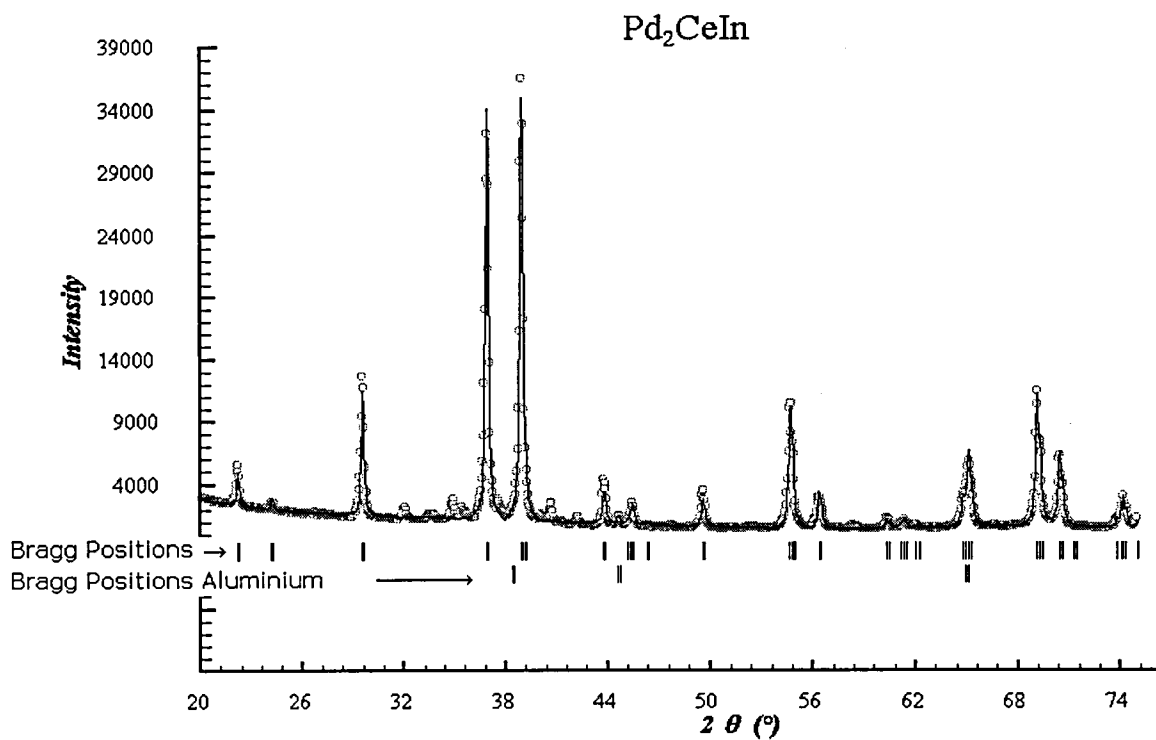
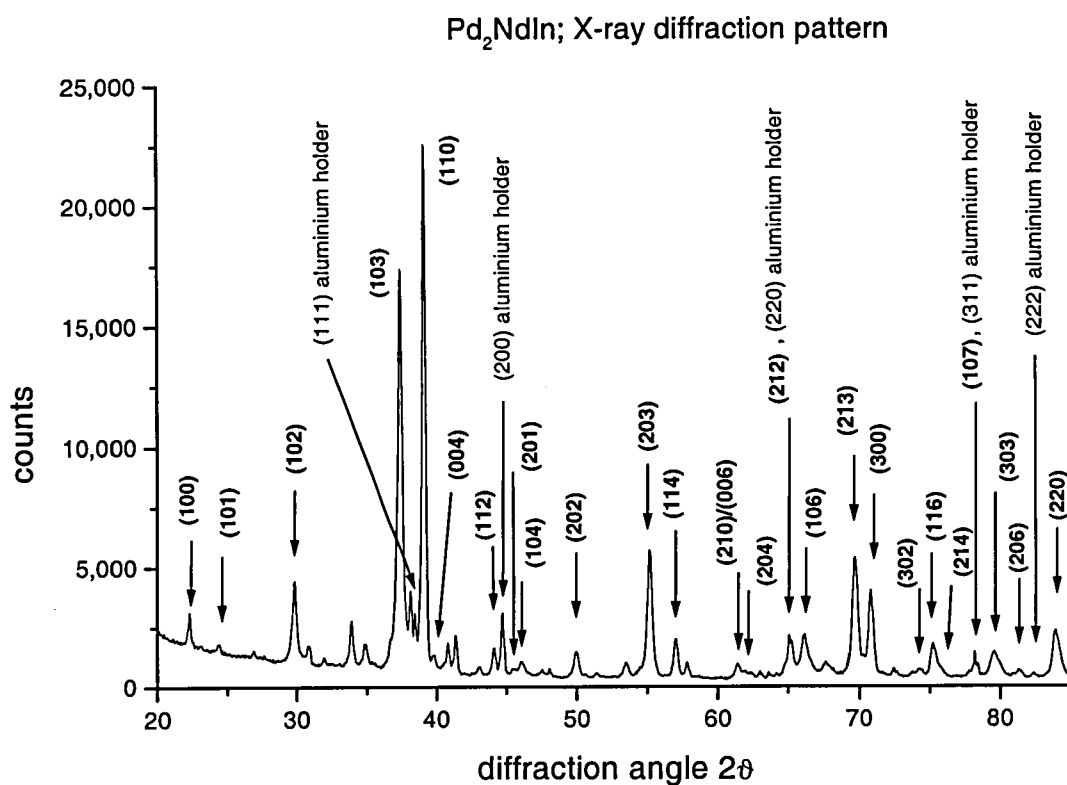
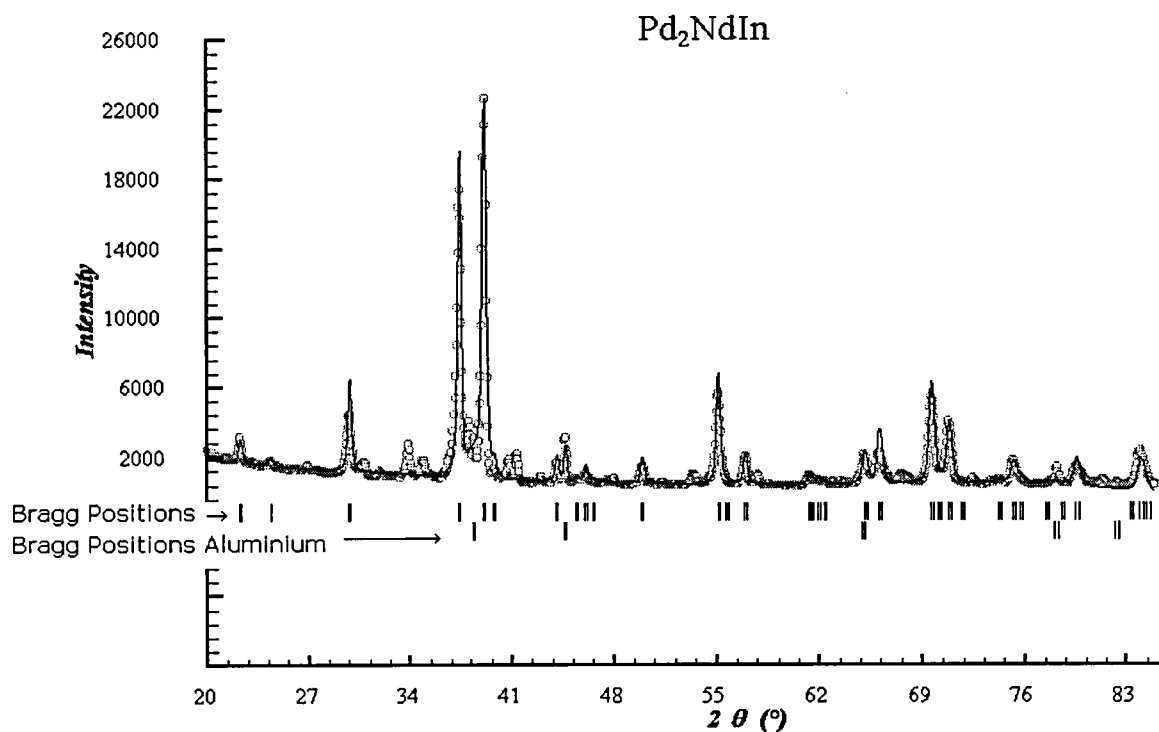


Figure 6.16: Pd₂CeIn X-ray diffraction pattern refinement using FullProf

Figure 6.17: Pd_2NdIn X-ray diffraction patternFigure 6.18: Pd_2NdIn X-ray diffraction pattern refinement using FullProf

6.3 Conclusion

Concluded it can be stated, that the structure of all Pd₂[RE]In alloys investigated is solved and the lattice parameter obtained are in good agreement with those values given in the literature. In the diffraction pattern of Pd₂HoIn only the principle reflections occur while the diffraction pattern of Pd₂ErIn, Pd₂YbIn and Pd₂LuIn show additional reflections of planes corresponding to reflection conditions described as case 1 and 2, section 6.2.2. Therefore, Pd₂ErIn, Pd₂YbIn and Pd₂LuIn are Heusler L2₁ alloys while Pd₂HoIn is a Heusler B2 alloy. Since no other peaks except those expected arise and the background is low, the alloys are considered single phase and of high purity.

The diffraction pattern of those alloys having hexagonal structure show, although most of the peaks are identified, a few peaks which are of small magnitude and are not recognised. These may be due to impurities or an additional phase.

6.4 References

- [6.1] Babateen M.O., "An Investigation of Magnetic Properties of Some Rare Earth Heusler Alloys", PhD Thesis, Loughborough University, (1994)
- [6.2] Xue B., Schwer H., Hulliger F. "Structure of LaPd₂In", Acta Cryst. (1992). C48, 2064-2065
- [6.3] Villars P., Calvert L.D., "Pearson's Handbook of Crystallographic Data for Intermetallic Phases", Volume 2, American Society for Metals, Metals Park/Ohio, (1991)
- [6.4] Hahn T., ed. "International Tables for Crystallography", Volume A, "Space Groups Symmetry, 2nd ed.", D. Reidel Publishing Company, Dordrecht, 1987
- [6.5] Webster P.J., Ziebeck K.R.A., "Landolt-Brönstein: Numerical Data and Functional Relationships in Science and Technology", subvolume III/19c: "Heusler Alloys", ed. by O Madelung, Springer-Verlag, Berlin (1988)

The preparation of the samples was accompanied by private communications with Peter Anders (Loughborough University, UK). The theory in this chapter on X-Ray Diffraction has been prepared by using the following textbooks

Guinier A., "X-Ray Diffraction", W.H. Freeman and Company, San Francisco, (1956)

Henry N.F.M., Lipson H., Wooster W.A., "The Interpretation of X-Ray Diffraction Photographs", MacMillan & Co Ltd., London, (1961)

7 MEASUREMENT OF SPECIFIC HEATS OF SOME Pd₂[RE]In ALLOYS

7.1 Specific Heat of Pd₂LuIn

The specific heat of Pd₂LuIn is measured from 4 K to 210 K, shown in Figure 7.1.

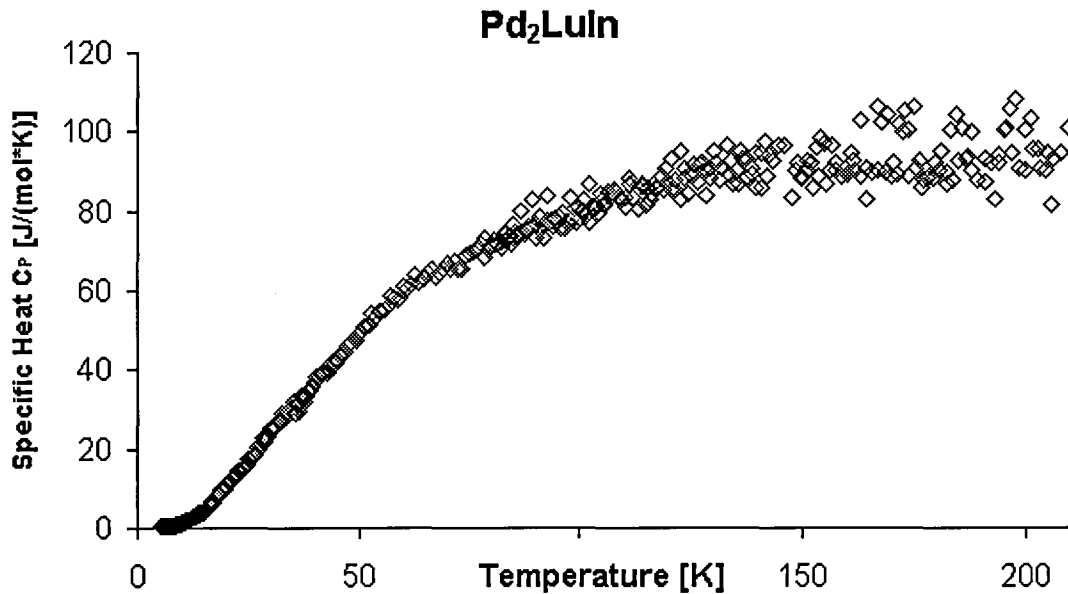


Figure 7.1: Specific Heat of Pd₂LuIn

Hence Pd₂LuIn is a non-magnetic material, the specific heat is given by

$$C_p = \gamma T + \beta T^3 \quad \text{for small } T \quad (7.1)$$

where $C_p \approx C_v$.

The contributions due to the conduction electrons and the crystal lattice vibration can be separated by plotting the experimental data in the form C_p/T versus T^2 (see section 4.6.1) which is presented in Figure 7.2. With the intercept γ and slope β of least square linear fit of the data, the Fermi T_F and the Debye Θ_D temperatures can be calculated using equations (4.49) and (4.39).

$$T_F = \frac{1}{\gamma} \frac{Nk_B\pi^2}{2} \quad (7.2)$$

$$\Theta_D = \sqrt[3]{\frac{1}{\beta} \frac{12}{5} Nk_B\pi^4} \quad (7.3)$$

The γ value is also directly related to the density of states at the Fermi surface (from equation (4.48)) by

$$D(e_F) = \frac{3}{\pi^2 k_B^2} \gamma . \quad (7.4)$$

The results are shown in Table 7.1.

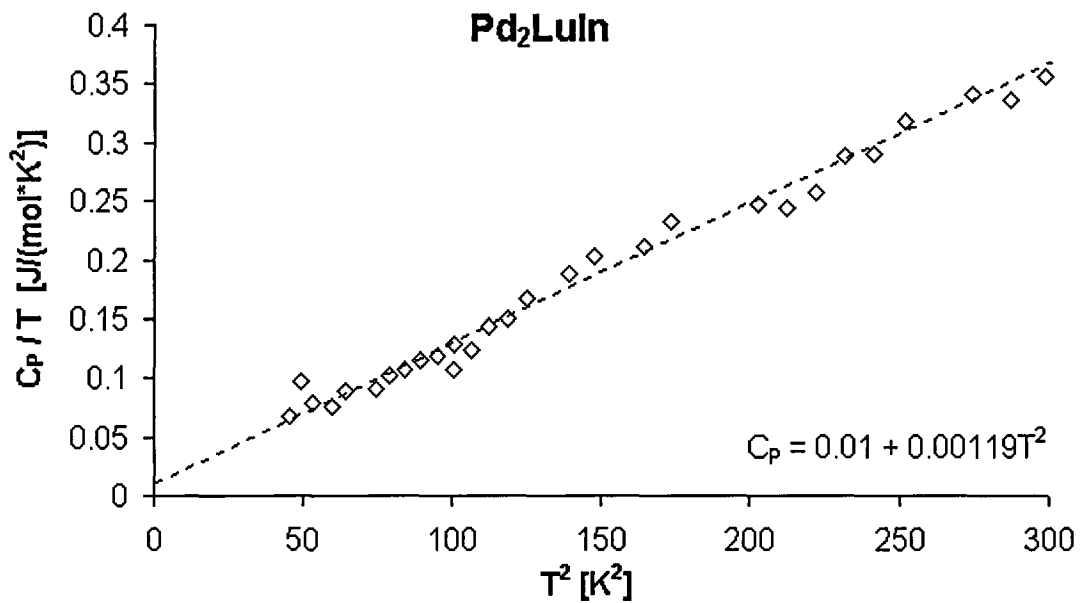


Figure 7.2: Low Temperature specific heat of Pd₂LuIn, in the form C_p/T vs. T^2

Table 7.1: Low Temperature Properties of Pd₂LuIn

	Pd ₂ LuIn	Literature
γ [mJ/(mol*K ²)]	10±5	10±1 [7.1]
T_F [K]	≈16'000	
$D(\epsilon_F)$ [states / f.u.* eV]	≈1.1	
β [mJ/(mol*K ⁴)]	1.19±0.03	
Θ_D [mol ^{-1/3} *K ⁻¹]	187±3	194±1 [7.1]

*formula unit

In the following specific heat of Pd₂LuIn is used as the phonon blank in the analysis of the specific heat measurement of other Pd₂[RE]In alloys. Therefore, the data in the temperature interval 4 K to 70 K are fitted by a polynomial fit of the order of 6. Figure 7.3 shows the quality of the fit. The data are nearly equally spread around both sides of the zero line, indicating that the fit is reasonable. The spread also indicates the resolution of the measurement.

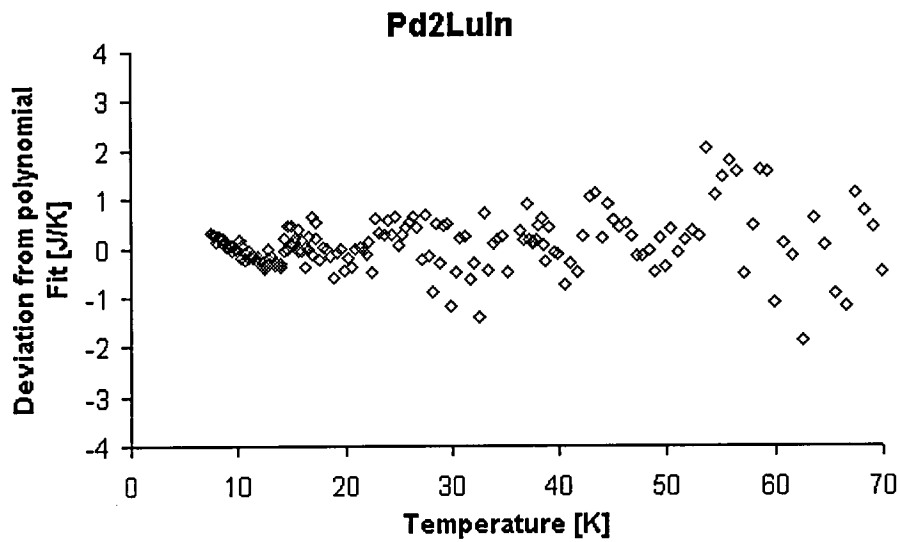


Figure 7.3: Deviation of the experimental data from the polynomial fit for Pd₂LuIn

7.2 Crystal Field Excitations in Pd₂YbIn

The specific heat of Pd₂YbIn was been measured within the temperature interval 4 K to 200 K, shown in Figure 7.4.

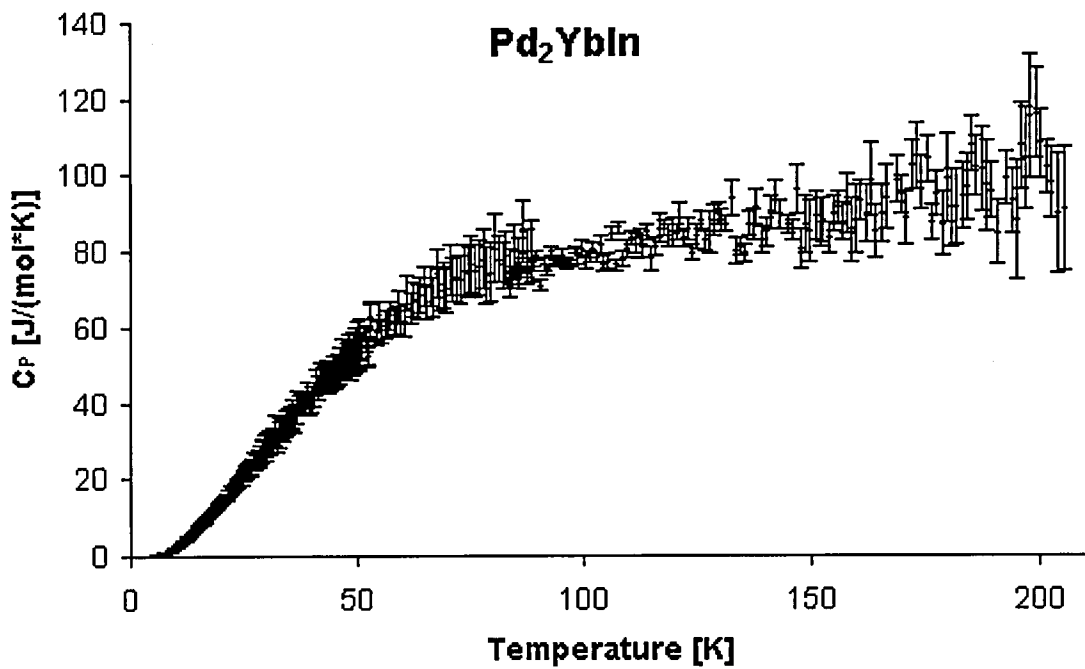


Figure 7.4: Specific Heat of Pd₂YbIn

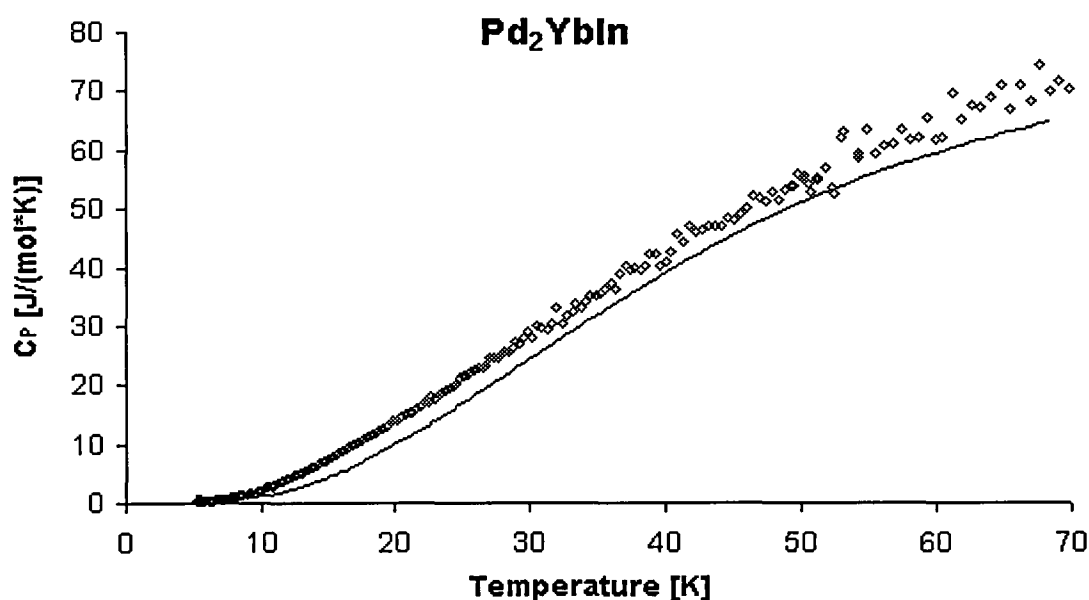


Figure 7.5: Specific Heat of Pd₂YbIn

The solid line indicates the fit for Pd₂LuIn multiplied with ρ_{scale} .

Clearly, the data for Pd₂YbIn remains in excess of that for Pd₂LuIn over the temperature range measured, indicating a magnetic contribution to the specific heat exists. The magnetic contribution is illustrated in Figure 7.7.

7.2.1 CEF Level Scheme

The ground state configuration of the 13 4f electrons of the Yb³⁺ ion is given by 4f¹³ ²F_{7/2} with a total angular momentum $J=7/2$ (3.7). According to LLW [7.2], when placed in a cubic crystal field, the 8-fold degenerated ground state is expected to split into a ground state quartet with two excited doublets as given by

$$J = 7/2 \rightarrow \Gamma_6 + \Gamma_7 + \Gamma_8 . \quad (7.5)$$

Therefore, two crystal field transitions are predicted. However, neutron scattering measurements reported by Babateen [7.3] indicate only a single transition due to the crystal field excitation¹⁴ at approximately 6.5 meV with no further transitions observed up to an energy transfer of 20 meV. The reason for this can be that either the two energy levels are too close to each other and therefore can not be separated by inelastic neutron scattering or that the most energetic CEF level is beyond the measured energy transfer range measured, in this case 20 meV. The two possible scenarios of CEF level schemes are presented in Figure 7.4.

¹⁴ further on called crystal field transition for simplicity

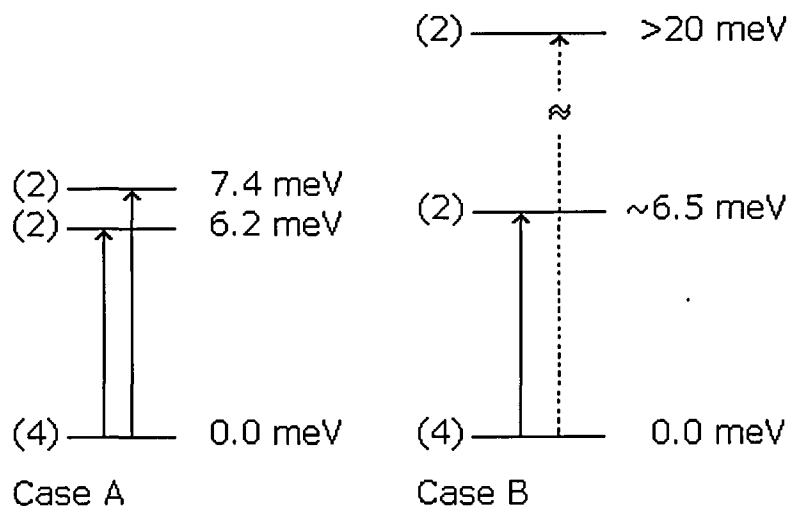
Pd₂YbIn

Figure 7.6: Possible CEF level schemes for Yb³⁺ in Pd₂YbIn, from neutron measurements [7.3].

7.2.2 C_{CEF} of Pd₂YbIn

To investigate the nature of this contribution, the magnetic specific heat is being calculated, in case A, for the thermal responses of the crystal field transitions of a ground state quartet with two excited doublets at 6.2 meV and 7.4 meV respectively shown in Figure 7.7 as a dashed line and in case B for a ground state quartet with only one excited doublet at ~6.5 meV and a second doublet above 20 meV, shown in Figure 7.7 as a dotted line. Since the energy gap between the ground state quartet and the second excited doublet in case B is large compared to the thermal energy of the investigated temperature range, possible electron transitions are unlikely for low temperatures and therefore these transitions are neglected in the calculation of the magnetic specific heat of Pd₂YbIn at low temperatures.

As illustrated in Figure 7.7, the exposed magnetic heat capacity of Pd₂YbIn corresponds more likely to a crystal field level scheme as described in case A, where two excited doublets are located at 6.2 meV and 7.4 meV above a ground state quartet than to case B. The Schottky peak occurs with a magnitude which is slightly too high but still comparable to that calculated but at a temperature approximately 24 K which is 7 K too low.

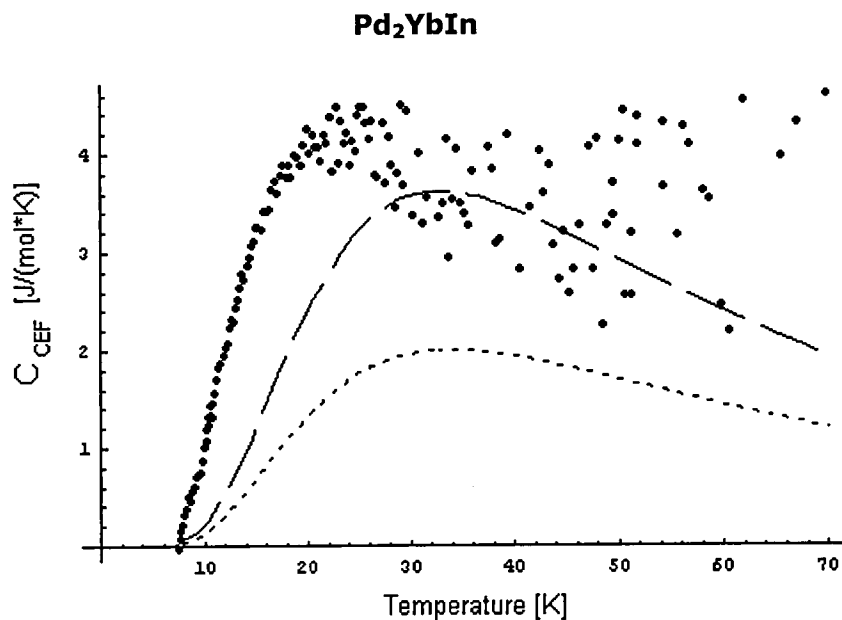


Figure 7.7: Magnetic specific heat of Pd₂YbIn. The theoretical contribution of the CEF level scheme in Case A (dashed line) and B (dotted line), as illustrated in Figure 7.6, are given.

7.3 Crystal Field Excitations in Pd₂HoIn

The specific heat of Pd₂HoIn is been measured within the temperature interval 5 K to 35 K shown in Figure 7.8.

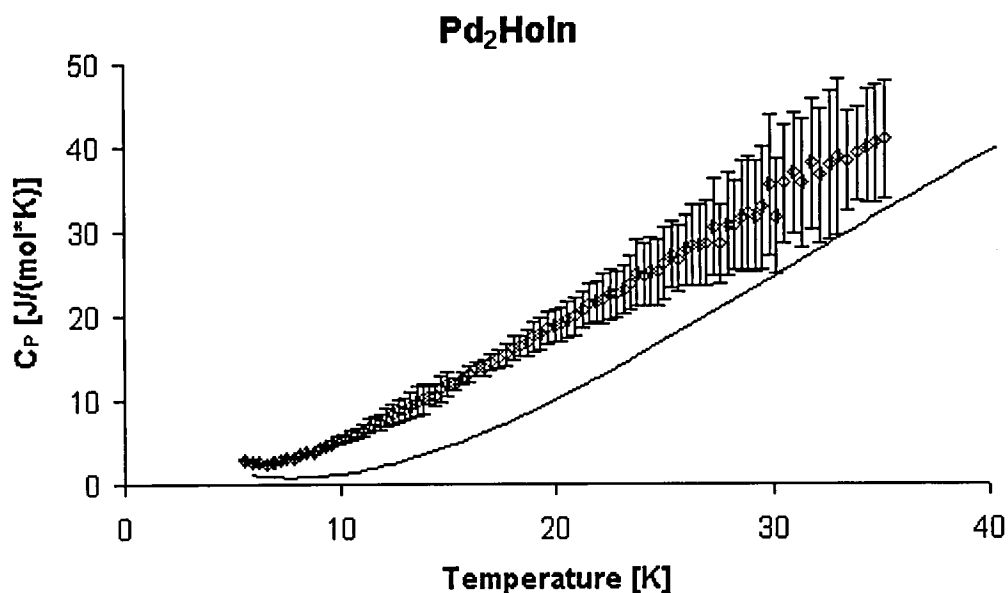


Figure 7.8: Specific Heat of Pd₂HoIn. The solid line is the corrected fit for Pd₂LuIn

7.3.1 CEF Level Scheme

Holmium has 10 4*f* electrons with total orbital angular momentum $L=6$, a total spin $S=2$ and total angular momentum $J=8$ (see (3.9)). The 17-fold degenerated ground state is expected to split up in the presence of a cubic field according to LLW [7.2] as followed

$$J=8 \rightarrow \Gamma_1 + \Gamma_3^{(1)} + \Gamma_3^{(2)} + \Gamma_4^{(1)} + \Gamma_4^{(2)} + \Gamma_5^{(1)} + \Gamma_5^{(2)}. \quad (7.6)$$

Figure 7.9 shows the CEF level scheme for Pd₂HoIn, obtained from inelastic neutron scattering measurements [7.3].

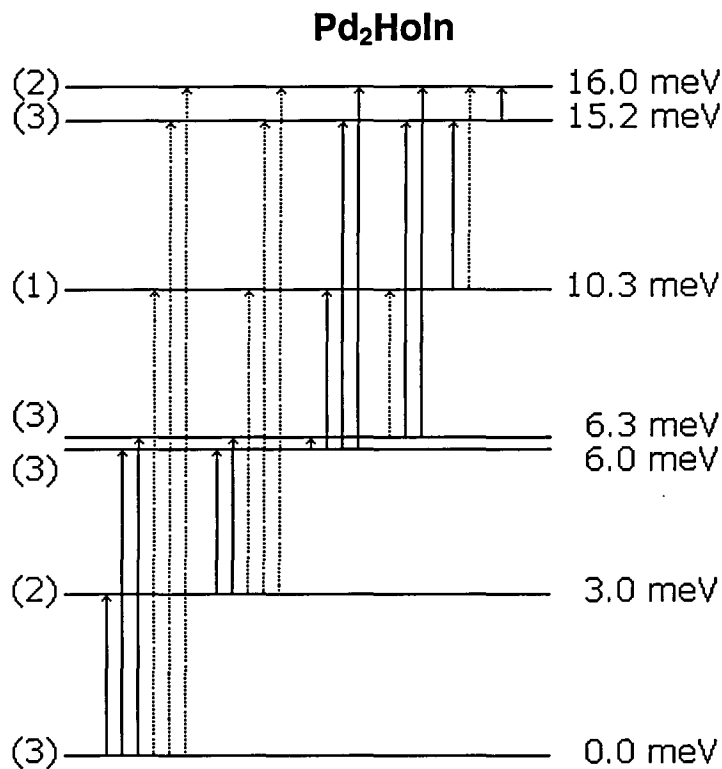


Figure 7.9: CEF level scheme for Ho³⁺ in cubic Pd₂HoIn, from [7.3]

7.3.2 C_{CEF} of Pd₂HoIn

The magnetic specific heat of Pd₂HoIn is isolated by subtracting the phonon specific heat, Pd₂LuIn corrected by ρ_{scale} , from the measured specific heat. The magnetic heat capacity of Pd₂HoIn is shown in Figure 7.10.

Again, the data for the magnetic capacity respond in shape and magnitude to the calculated curve but an offset is observed.

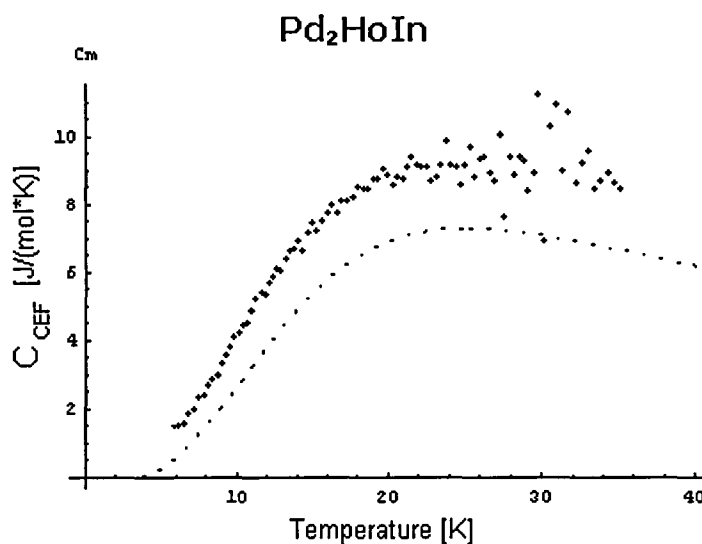


Figure 7.10: Magnetic specific heat of Pd₂HoIn. The theoretical contribution of the CEF level scheme as illustrated in Figure 7.4, is given.

7.4 Discussion

The curves of the magnetic specific heats of Pd₂HoIn and Pd₂YbIn are above the calculated values. Therefore, it was assumed that a general error in the measurement might influence the result. On the other hand, the specific heat of Copper obtained corresponds well with previous results. Thus, it appears that the only possible error, which both magnetic specific heats have in common, must arise from the phonon contribution namely the specific heat of Pd₂LuIn.

Therefore, from the measured heat capacities of Pd₂HoIn and Pd₂YbIn the heat capacities of the grease, the addenda and the calculated magnetic contributions are subtracted to obtain the theoretical phonon heat capacity. The results are normalised to obtain the specific heat of Pd₂LuIn. The outcome is plotted in Figure 7.11. The graphs reveal that the specific heat of Pd₂LuIn calculated from Pd₂HoIn and Pd₂YbIn are almost identical while the value of measured specific heat of Pd₂LuIn is significantly lower.

Since the two independent measurements of the specific heats of Pd₂HoIn and Pd₂YbIn come to the same result for the specific heat of Pd₂LuIn using the two different crystal field level scheme of Pd₂HoIn and Pd₂YbIn it is assumed that the offset in the magnetic specific heats of Pd₂HoIn and Pd₂YbIn is caused by an incorrect specific heat of Pd₂LuIn measured.

Therefore, the crystal field level scheme of Pd₂HoIn and Pd₂YbIn obtained from inelastic neutron scattering measurements by Babateen [7.3] can be confirmed.

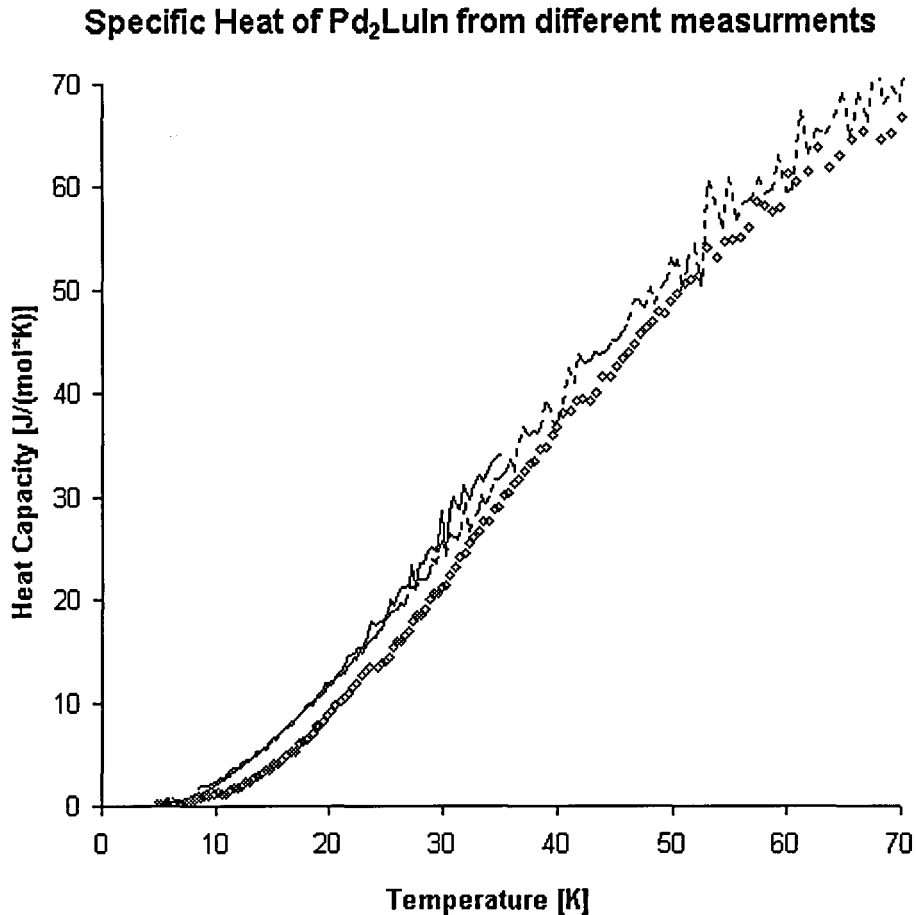


Figure 7.11:The Specific Heat of Pd₂LuIn measured (diamonds), calculated from the Specific Heat of Pd₂YbIn (solid line) and calculated from the Specific Heat of Pd₂HoIn (dashed line)

For very low temperatures, $T < 10\text{K}$, the measured and calculated specific heat of Pd₂LuIn seem to be equal. Therefore, the obtained values for γ and Θ_D are assumed to be correct.

The reason for the measured specific heat of Pd₂LuIn being too low is assumed to be found in the sample size.

While the post-heat temperature is measured during the post-heat-drift time, the sample system loses energy to the calorimeter, since its temperature is higher. For samples of approximately 1 gram and a difference in sample- and shield-temperature of less than 1K, the cooling rate is of the order of 10^{-3} K/sec. For smaller samples, here Pd₂LuIn with 0.7649g, this gradient is of the order of 10^{-2} K/sec, schematically demonstrated in Figure 7.12. This leads to a higher post-drift temperature. The effect does not occur when measuring the pre-heat-pulse temperature since the sample is given time to stabilise before measuring the heat capacity at a certain temperature (see section 5.5.2 Preparation Phase). Consequently a higher temperature rise is assumed, equation (5.8).

Therefore, if the sample is too small, the temperature taken as the post-drift temperature is too high and thus ΔT is too large. Since the heat capacity is inverse proportional to the temperature rise (equation (5.1)), the heat capacity obtained is smaller than the actual value.

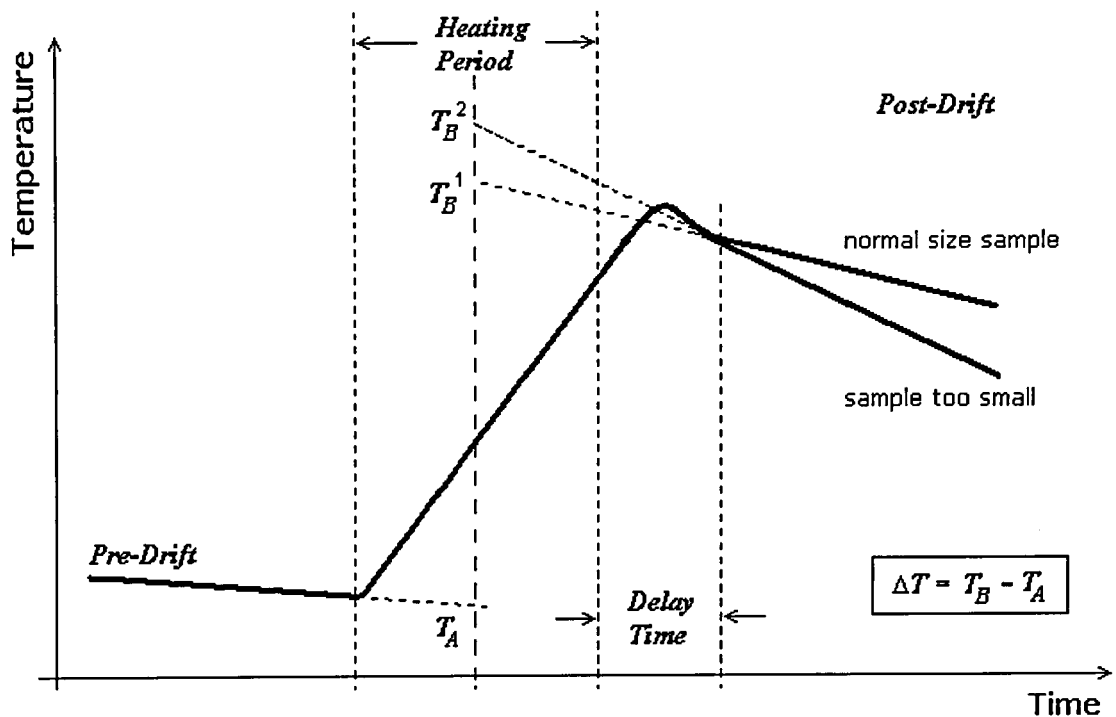


Figure 7.12: The effect of the sample weight on the post-heat temperature.

7.5 References

- [7.1] Parsons M.J., "An Investigation of the thermal properties of some Strongly Correlated Electron Systems", PhD Theses, Loughborough University, (1998)
- [7.2] Lea K.R., Leask M.J.M. Wolf W.P., " The Raising of angular momentum degeneracy of f-electron terms by cubic crystal fields", J. Phys. Chem. Solids, Pergamon Press, V23, pp1381-1405, (1962)
- [7.3] Babateen M.O., "An Investigation of Magnetic Properties of Some Rare Earth Heusler Alloys", PhD Thesis, Loughborough University, (1994)

8 SUMMARY AND OUTLOOK

This thesis is a summary of the work done by the author during the period 2000-2001 in the Department of Physics, Loughborough University and under the guidance of Dr. K.-U. Neumann. It was aimed to improve the performance of the instrument used to measure the specific heat of solids and to make statements on the crystal field level scheme of the $4f$ electrons of some Rare Earth metals in $\text{Pd}_2[\text{RE}]\text{In}$ alloys.

Placed in a crystal lattice, the degeneracy of the degenerated ground state of the Rare Earth $4f$ electron levels is lifted partially. The crystal field level scheme of the $\text{Pd}_2[\text{RE}]\text{In}$ alloys under consideration was obtained from inelastic neutron scattering by previous works. The excited CEF levels become populated if temperature is increase from 0K. This contribution to the specific heat was isolated for Pd_2YbIn and Pd_2HoIn .

To improve the shield temperature responds a new heater was installed. Therefore, the shield control parameter had to be refined. To improve the accuracy of the measurement, the sample temperature sensor was recalibrated, new Apiezon N grease heat capacity data and new Addenda heat capacity data were obtained. Furthermore, to acknowledge the possibility to use different cooling liquids the control software was rewritten.

X-ray diffraction measurements were performed to characterise the samples prepared such as $\text{Pd}_2[\text{RE}]\text{In}$ ($\text{RE} = \text{Ce}, \text{Nd}, \text{Ho}, \text{Er}, \text{Yb}, \text{In}, \text{Lu}$). It revealed the so far unknown structure of Pd_2CeIn and Pd_2NdIn .

To complete the studies of the thermal properties of $\text{Pd}_2[\text{RE}]\text{In}$ alloys in future work, the specific heat of those materials which were not investigated in this work needs to be measured. In order to obtain the magnetic specific heat, it is recommended to prepare a larger Pd_2LuIn sample.

It is suggested to replace the LakeShore Cryotronics, Inc. TEMPERATURE CONTROLLER MODEL DRC-93C by a later model since most of the uncertainties, shown for example in Figure 5.21 and Figure 5.23, especially for high temperatures, arise from the circumstances, that the 9318C RESISTANCE INPUT CARD alters the supply current in steps to maintain the supply voltage across the sensors. Newer models do not work in that way. For further detail see section 5.3.2 Temperature Measurement and the Lakeshore manual [5.5]

